CHARACTERISATION OF ZINC AND BERYLLIUM DOPED INDIUM PHOSPHIDE GROWN BY MOLECULAR BEAM EPITAXY

A Thesis

Submitted to the Faculty of Engineering

of the University of Glasgow

for the degree of

Doctor of Philosophy

by

Robert McIlwraith Park, B.Sc.

October 1981.

ACKNOWLEDGEMENTS

I wish to express my gratitude to Professor J. Lamb for the provision of research facilities and the Science Research Council for financial support over the period of this investigation. Sincere thanks is also due to my supervisor Dr. C.R. Stanley for his guidance throughout the project and also for his valuable assistance in the preparation of this thesis.

Grateful acknowledgement is made to Dr. I. Gale of P.R.L. (Redhill, Surrey) for the atomic absorption spectrometry analysis and to Drs. G. Jones and C. Pickering of R.S.R.E. (Malvern) for the texture camera and double crystal diffractometry analyses, and the plasma reflectivity measurements, respectively. I would also like to thank Messrs Boyle, Young, and Clark of the technical staff for their excellent assistance. I am particularly indebted to my fellow research student Mr T. Kerr who performed the photoluminescence measurements and also to Dr. P. Sullivan with whom I had many stimulating and helpful discussions.

Finally I wish to thank my sister Mrs. J. Kerr for her excellent typing of the manuscript and also my parents for their financial and emotional support throughout my education.

TABLE OF CONTENTS

SUMMARY

The purpose of the work reported in this thesis was two-fold. The first objective was to investigate the incorporation behaviour of both zinc (Zn) and beryllium (Be) in molecular beam epitaxy (MBE) grown indium phosphide (InP) with a view to growing device quality p-type InP material. Secondly, a deep level transient spectroscopy (DLTS) system was designed and constructed in order to detect and possibly identify deep level majority carrier trapping centres in MBE grown InP, the aim behind this investigation being to provide feedback information in order to improve the quality of InP grown by MBE.

Prior to commencing the doping study an investigation was carried out into the growth of unintentionally doped InP by MBE onto Fe-doped semi-insulating InP substrates which were atomically cleaned in-vacuo by the process of argon ion sputtering followed by annealing. Hall-effect and plasma reflectivity measurements made on unintentionally doped InP films grown onto sputtered and annealed substrates yielded substantially different results; Hall-effect measurements typically yielded nett donor concentrations N_D-N_A of $\sim 3\times10^{16}cm^{-3}$ and electron mobilities $< 1000\ cm^2V^{-1}s^{-1}$ at R.T. while higher electron mobilities, typical $\approx 3{,}000\ cm^2V^{-1}s^{-1}$, were obtained by the plasma reflectance technique with N_D-N_A being $\approx 10^{17}cm^{-3}$. This result lead to speculation that the substrate/film interface region was seriously influencing electrical

measurements on the films and an investigation into the effects of the sputtering and annealing cleaning process on substrate surfaces was initiated to verify this hypothesis. Hall-effect and C-V profiling techniques revealed that the surface of semi-insulating substrates is converted to n-type with N_D-N_A in the range $10^{16}-10^{17}cm^{-3}$ to a depth of $\sim$ 1,000Å as a result of the sputtering and annealing process. Hence films grown onto sputtered and annealed substrates are interfaced by a conducting layer.

Zn was found to have a near unity sticking coefficient on (100) InP grown by MBE at substrate temperatures around 360°C and Zn concentrations up to $\sim 4x10^{20}cm^{-3}$ were achieved in films as measured by atomic absorption spectrometry analysis with no apparent degradation of either the surface morphology or crystal structure. Plasma reflectivity measurements on Zn doped films yielded nett donor concentrations of $\simeq 10^{17}cm^{-3}$ and electron mobilities in the range 2,500-3,000 $cm^2V^{-1}s^{-1}$, ie the electrical properties of Zn doped films were almost identical to those of unintentionally doped films, indicating the Zn content in MBE grown InP to be electrically in-active. Be was also shown to have a unity sticking coefficient on (100) InP grown by MBE at substrate temperatures around 360°C and Be concentrations in films ranging from $5x10^{17}cm^{-3}$ to $2x10^{19}cm^{-3}$ were achieved as measured by atomic absorption spectrometry analysis. The Be content in MBE grown InP films was shown to be partially activated, indicating a degree of substitutional

incorporation; Be doped films were found to be highly compensated n-type.

Unintentionally doped InP grown by MBE was shown to contain a dominant deep level electron trap by deep level transient spectroscopy analysis having a thermal activation energy to the conduction band of 0.59eV and a capture cross-section of $1.8 \times 10^{-12} cm^2$. The concentration of the deep level trap was found to be dependent on the substrate temperature during growth; the trap concentration increased from $8 \times 10^{14} cm^{-3}$ to $3 \times 10^{15} cm^{-3}$ as the substrate temperature was lowered from $360^{\circ}C$ to $300^{\circ}C$.

CHAPTER 1.

CHAPTER 1

INTRODUCTION

1.1 Introduction

Molecular beam epitaxy (MBE) is a high vacuum technique for the growth of epitaxial layers, usually semiconductors, that utilises thermal beams of source atoms or molecules impinging on a single - crystal substrate [1.1]. MBE has been developed over the past decade or so and is now not only an important technology for the fabrication of microwave and electro-optic devices, but also a vehicle for the investigation of fundamental properties of semiconductors, metals and insulators (see, for example, Cho [1.2]). The MBE technique is superior to other epitaxial growth techniques such as liquid phase epitaxy (LPE) and vapour phase epitaxy (VPE) in that ultra thin layers of extreme smoothness can be reproducibly grown with tailored doping profiles and/or composition on an atomic scale normal to the growth surface. The high degree of growth control afforded by MBE was first demonstrated by Chang et al [1.3] for MBE growth of GaAs/ $Al_x Ga_{1-x}As$ superlattices consisting of several alternate layers of GaAs and $Al_xGa_{1-x}As$ with layer thickness as low as 50Å. More recently, Ploog et al [1.4] have reported the growth by MBE of a novel superlattice structure, known as the "nipi" structure, consisting of a periodic sequence of ultrathin (200Å → 1500Å) p- and n-type GaAs layers separated by

intrinsic (i-) layers. Such a structure, which prior to the development of MBE was only considered on a theoretical basis, may have an effective energy-gap of any value between the energy-gap of bulk GaAs (1.45eV) and zero, depending on the choice of layer thickness and carrier concentration. Furthermore, the carrier concentration and consequently the effective band gap of nipi crystals can be modulated within wide limits by the application of an external bias, thus suggesting a voltage-tunable semiconductor laser (see, for example, Döhler and Ploog [1.5]).

MBE lends itself to the fabrication of complex structures since the constituent elements of a particular semiconductor and the required dopant elements are evaporated as separate atomic or molecular beams having precisely controlled effusion rates and which can be instantaneously shuttered from the substrate onto which epitaxial growth is taking place. An illustration of a typical MBE growth arrangement is shown in Fig. 1.1. Furthermore, substrate temperatures during MBE are low (eg, 550°C for GaAs) compared to those required for LPE (850°C) and VPE (750°C); consequently dopant interdiffusion between adjacent layers is minimal in MBE and therefore hyperabrupt p-n junctions are possible.

1.1.1 Molecular Beam Epitaxy of Compound Semiconductors

MBE of III-V compounds has its origins in the so-called "three-temperature" technique developed by Günther [1.1].

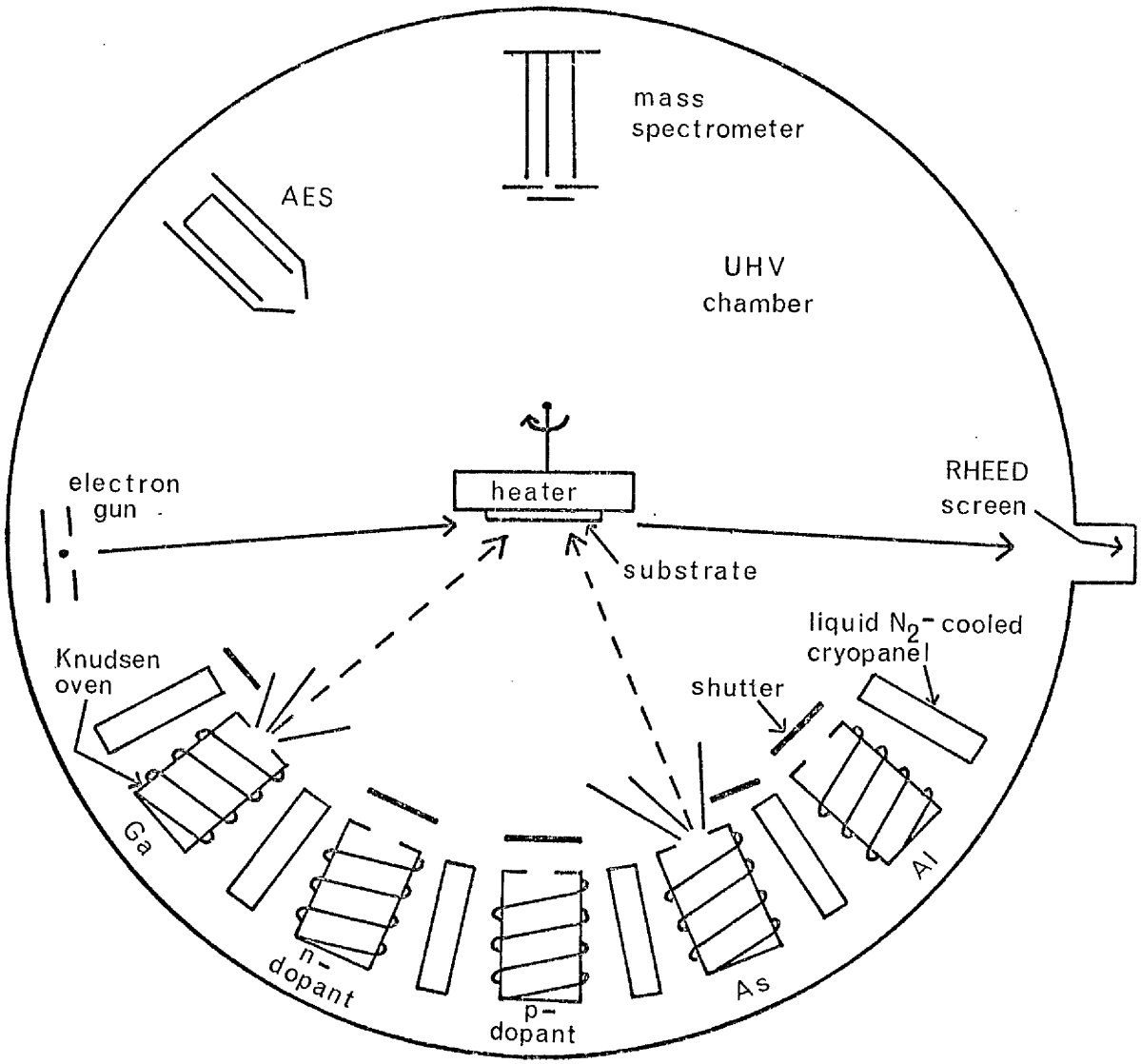

FIG. 1.1 : Typical MBE multi-layered device growth system (plan view).

The three-temperature technique for the vacuum deposition of III-V compounds relied on the much lower vapour pressure of the group V element over the III-V compound than over the pure group V solid. A group V element source oven was held at a temperature T_1 to maintain a steady pressure in the vacuum chamber, while a separate group III element source oven was held at a higher temperature T_3 to provide a flux of atoms incident on the substrate, the substrate being maintained at an intermediate temperature T_2 which was high enough to eliminate the condensation of excess group V element on the surface. This technique resulted in the growth of stoichiometric films of a number of binary and ternary III-V compounds; however, since the substrates were usually glass the deposited films were invariably polycrystalline. Epitaxial growth of GaAs by the three-temperature method was first demonstrated by Davey and Pankey [1.6] on both GaAs and Ge substrates which were atomically cleaned in-vacuo by an ion bombardment technique. The ion bombardment substrate cleaning process used by these authors was later shown by Auger electron spectroscopy (AES) studies [1.7] to result in the removal of contaminants such as C and O from GaAs surfaces prior to epitaxial film deposition. Around the same time an investigation was reported by Arthur [1.8] into the kinetics of the interaction of collimated molecular beams of Ga and As_2 with a GaAs surface using modulated beam mass spectrometry techniques. This study revealed that above a substrate temperature of 500K the adsorption of

As_2 on GaAs was directly dependent on the surface population of Ga adatoms. It was established that if an arsenic molecule encountered a free Ga atom during its surface lifetime, the molecule remained on the surface, while if no free gallium was available the arsenic molecule re-evaporated following surface migration. These observations suggest that the growth rate of GaAs is controlled by the arrival rate of Ga atoms while stoichiometric growth is ensured provided an excess of arsenic is supplied at the substrate. Although this interpretation has since been found to be somewhat oversimplified (see, for example, Foxon and Joyce [2.14]) considerable success was achieved in growing stoichiometric GaP and $GaAs_xP_{1-x}$ films as well as GaAs films on GaAs substrates by MBE using similar molecular beam flux conditions [1.9]. MBE of III-V compounds and alloys became highly controllable and sophisticated following the incorporation into MBE systems of AES systems to monitor substrate surface cleanliness prior to film deposition, and reflection high-energy electron diffraction (RHEED) systems, to monitor film crystallinity and surface structures during growth (see, for example, Cho [1.1]).

Much of the early motivation for MBE research was to develop a technology capable of reproducibly growing multiple-layer GaAs - $Al_xGa_{1-x}As$ structures for injection lasers. In 1976, Cho et al [1.10] demonstrated the first continuous room temperature operation of an MBE grown

GaAs - $Al_xGa_{1-x}As$ double heterostructure laser (DH laser), although at that time the threshold current density for lasing was twice that for a similar structure grown by LPE. By early 1979, further improvements in vacuum apparatus and growth techniques yielded lasers with threshold current densities even lower than those of comparable lasers grown by LPE and today GaAs - $Al_xGa_{1-x}As$ DH lasers with R.T. threshold current densities of 1 to 1.5 kA cm^{-2} or lower can now be prepared almost routinely by MBE. In addition to the fabrication of DH injection lasers MBE of GaAs and $Al_xGa_{1-x}As$ has been successfully applied in other device areas. For example, GaAs and $Al_xGa_{1-x}As$ optical waveguides have been grown by a selective area growth technique using Si shadow masks. Single and multilayer stripe-mesa waveguides with widths as narrow as 1μm have been reported using this technique[1.11]. Also, the operation of high performance MBE grown GaAs microwave devices, such as varactors [1.12], IMPATT diodes[1.13] and MESFETS [1.14], has been demonstrated. Because the doping profile is critical in such applications MBE is especially well suited to the fabrication of these devices. Over the last few years the range of semiconductor materials grown by MBE has been extended dramatically and now includes III-V, III-III-V, III-III-V-V, III-III-III-V, II-VI, and II-II-VI compounds. Fig. 1.2 details the semiconductors that have been prepared by MBE in relation to their energy-gaps.

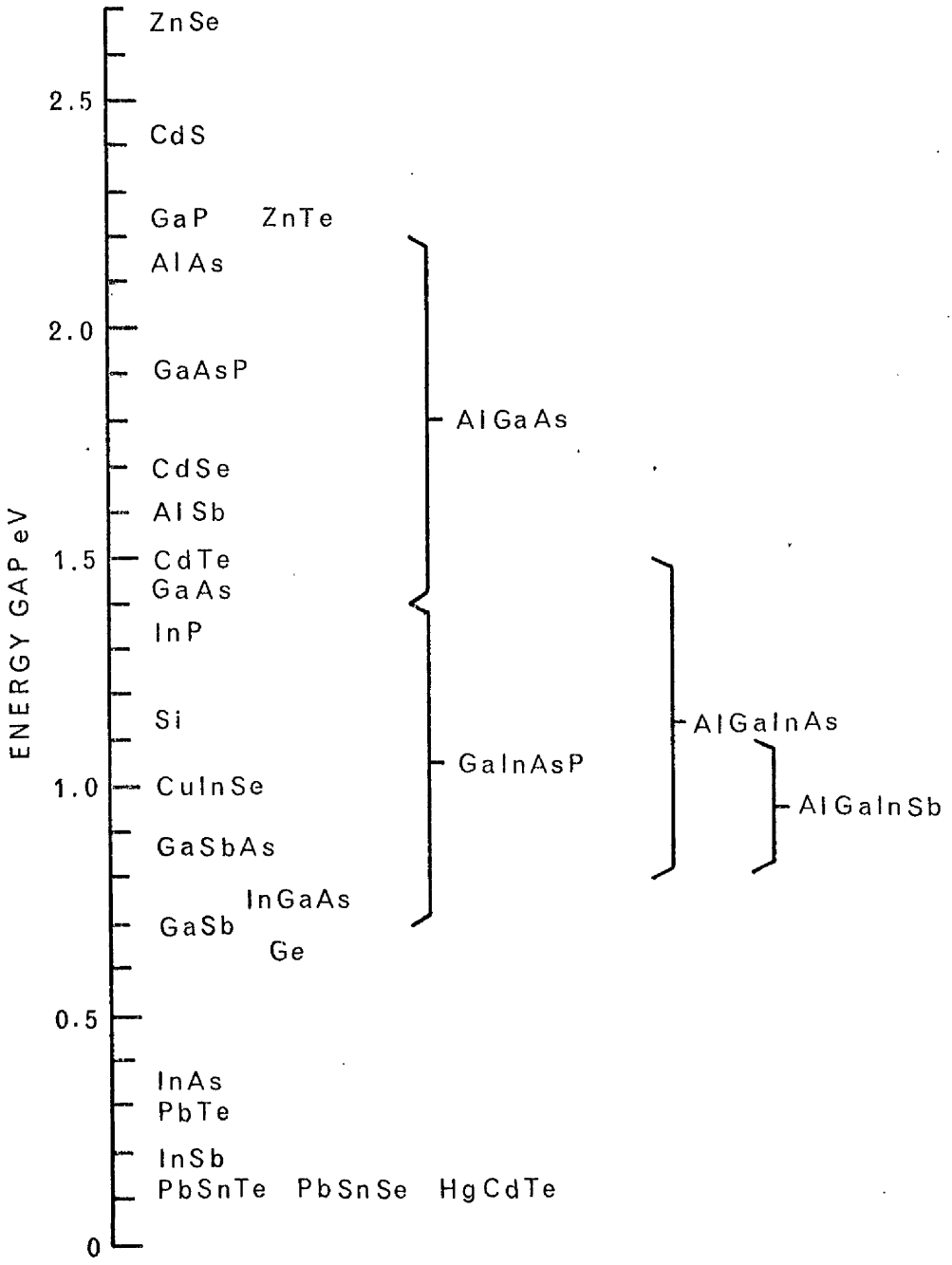

FIG. 1.2 : Semiconductor compounds grown by MBE versus energy gap.

The energy gaps of the ternary compounds listed in column 1 correspond to ternary compositions which lattice-match to single crystal substrates.

1.1.2 Device Applications of InP

The quaternary compound $Ga_xIn_{1-x}As_yP_{1-y}$ (see Fig. 1.2) is currently receiving much attention due to the potential application of sources and detectors based on this material in optical-fibre communication systems. $Ga_xIn_{1-x}As_yP_{1-y}$ is a particularly attractive semiconductor compound since the energy-gap of the alloy can have any value between 1.35eV and 0.75eV (0.9μm → 1.65μm) depending on the choice of x and y while maintaining an exact lattice match with InP. Since present-day ultra-low-OH content optical fibres exhibit minimum attenuation over a band of wavelengths ranging from 1 to 1.6μm [1.15], the transmission loss in this 'window' being $<1dBkm^{-1}$ (see Fig. 1.3), semiconductor lasers with $Ga_xIn_{1-x}As_yP_{1-y}$ active regions are ideal as potential sources in optical-fibre communication systems. Continuous R.T. operation of LPE grown [1.16 - 1.18] and VPE grown [1.19] InP/GaInAsP/InP DH lasers emitting in the 1.1 → 1.3 μm range has been demonstrated; a typical InP/GaInAsP/InP DH laser structure is illustrated in Fig. 1.4. MBE growth of such laser structures, however, is in a much earlier stage due principally to difficulties found in growing the quaternary layer on account of the greatly differing physiochemical properties of As and P [1.20]. MBE growth of the ternary compound $Ga_xIn_{1-x}As$ which lattice matches to InP for x = 0.47 is a simpler proposition and has been

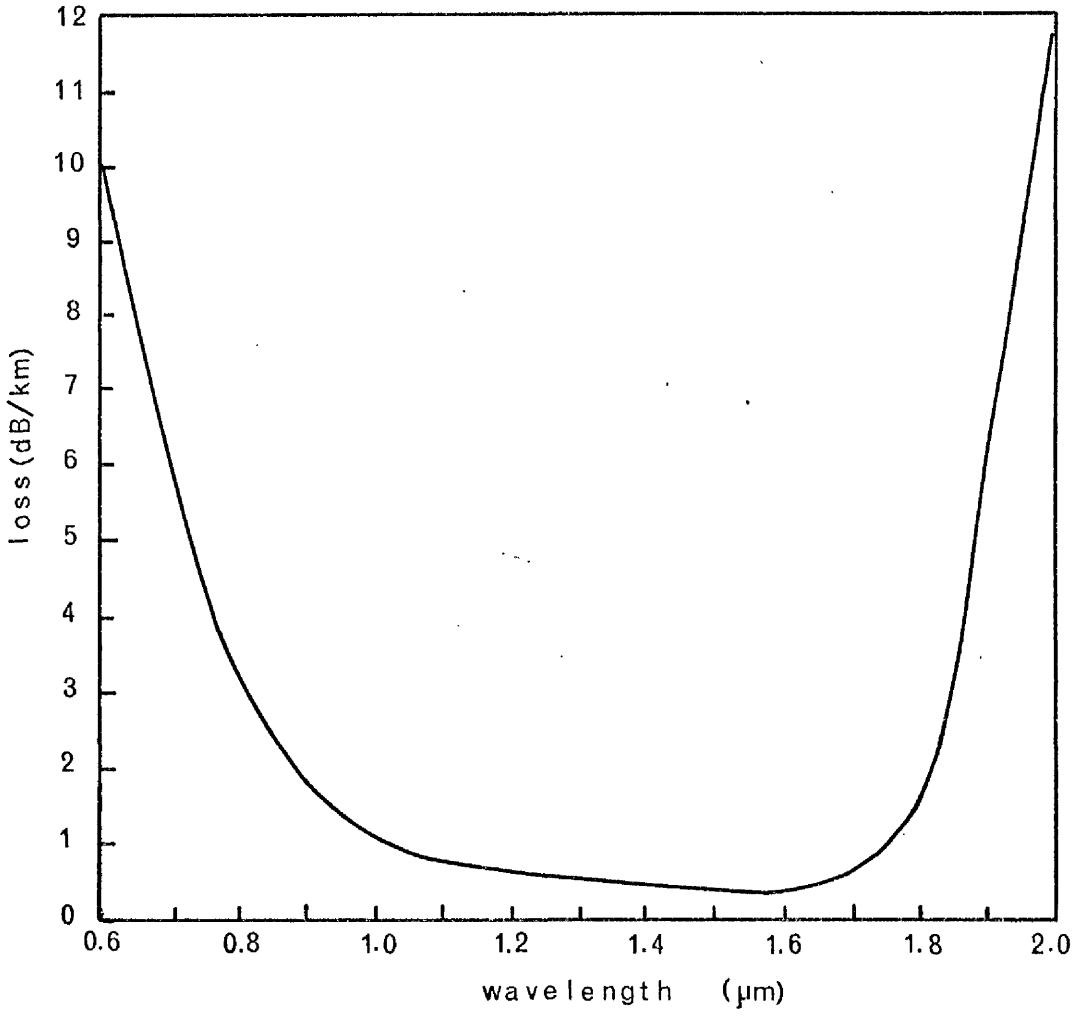

FIG. 1.3 : OPTICAL FIBRE TRANSMISSION LOSS VERSUS WAVELENGTH.

(REF. 1.15)

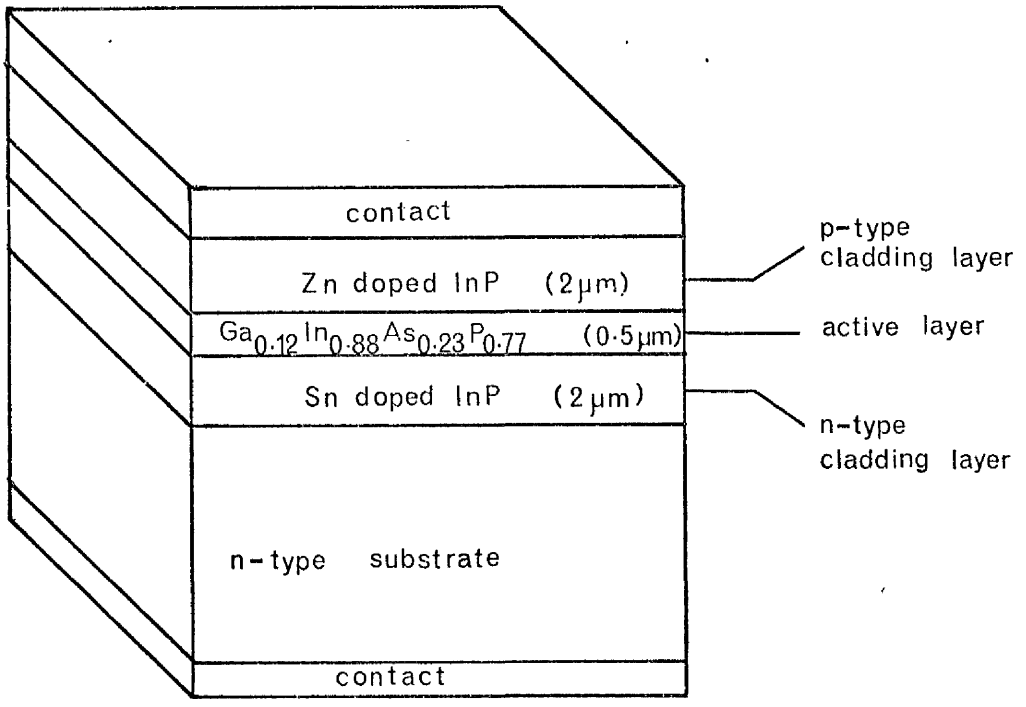

FIG. 1.4 : InP/GaInAsP/InP DH Laser grown by LPE (Ref. 1.16).

reported by several authors [1.21 - 1.25]. Furthermore, R.T. operation of lattice-matched InP/$Ga_{0.47}In_{0.53}As$/InP DH lasers grown by MBE with pulsed emission at 1.65μm has been reported by Miller et al [1.26]. In the laser structure reported by these authors Ge was used as the n-type dopant for the n-type InP cladding layer while the p-type cladding layer was produced by post-growth diffusion of Cd, ie the p-type InP layer was not grown directly by MBE.

It is obvious from the foregoing discussion that InP has become an important material with regard to the fabrication of modern opto-electronic devices. The material also has potential use in microwave devices such as transferred electron oscillators and amplifiers [1.27, 1.28] where InP appears to yield lower noise devices than GaAs. These two principal applications have spurred on research efforts in MBE of InP in recent years with a view to growing device quality material.

1.1.3 MBE of InP - A Review

The growth of (100) InP by MBE from In and P_2 beams was first reported by Farrow [1.29]. Farrow's early experiments, however, were not reproducible since his in-vacuo substrate heat cleaning technique did not satisfactorily remove surface contaminants such as C and O prior to film deposition [2.4]. McFee et al [1.30] later presented a detailed study of the growth conditions

and the electrical and optical properties of InP films grown from In and P_4 molecular beams on (111) and ($\bar{1}\bar{1}\bar{1}$) orientated substrates which were cleaned in-vacuo by an argon ion bombardment process. These authors found that the optimum substrate growth temperature was $\sim 450^{o}C$ and also mentioned that preliminary studies had indicated that the surface morphology of (100) orientated InP films was superior to that of (111) and ($\bar{1}\bar{1}\bar{1}$) orientated films. Norris and Stanley (1.31) subsequently reported a study of the substrate temperature limits for epitaxy of (100) InP from In and P_2 molecular beams; substrate surfaces were atomically cleaned by three 500eV argon ion bombardment/anneal cycles. The upper substrate temperature limit was found to be $410^{o}C$, with whisker growth from In droplets occuring above this temperature, while polycrystalline growth was observed at substrate temperatures $< 100^{o}C$. . These authors reported an optimum growth temperature of $\sim 360^{o}C$ for unintentionally doped InP films; films grown at this temperature were n-type with a nett donor concentration of $\sim 2 \times 10^{16}$ cm^{-3} and an electron mobility $\sim 3{,}000$ $cm^{2}V^{-1}s^{-1}$ at R.T. Around the same time, Kawamura et al (1.32) reported the growth by MBE of high quality unintentionally doped (100) InP films from In and P_4 molecular beams. A recent development has been the growth of molecular beam epitaxial InP onto substrates thermally cleaned at $\sim 500^{o}C$ in a P_2 flux in contrast to the generally adopted technique of argon ion sputtering followed by annealing (1.33).

To-date very little has appeared in the literature on n- and p-type doping of InP grown by MBE. Matsushima et al [1.34] reported Sn doped n-type InP layers grown on GaAs substrates, however, no information was given on the electrical and optical properties of the films. Homo-epitaxial Sn doped InP films were reported by Miller et al [1.35, 1.36] with n-type doping levels ranging from 2×10^{16} cm^{-3} to 2×10^{19} cm^{-3}. P-type doping of InP grown by MBE has been briefly reported by Backmann et al [3.15] for Mg, Be and Mn but no details of doping range attained, orientation of substrates or growth conditions were given. Since very little attention has been given to doping studies of MBE grown InP it is obvious that a greater research effort is required in this field if InP devices grown by MBE are to be realised.

1.2 Aims of Research

The two main objectives of the work described in this thesis were as follows:

1. To investigate the use of both Zn and Be as possible p-type dopants in MBE grown InP with a view to producing device quality p-type material.
2. To design and construct a deep level transient spectroscopy (DLTS) system in order to facilitate the detection and possible identification of deep level carrier traps in MBE grown InP. The principal aim behind this work being to provide feedback information in order to improve the quality of InP grown by MBE.

1.3 Review of Contents of Thesis

In chapter 2 the basic principles governing the growth of III-V compounds by MBE are discussed. Particular emphasis is placed on GaAs since extensive studies have been reported on the kinetics of GaAs growth by MBE whereas very little has been published on the growth kinetics of other III-V compounds. Molecular effusion theory is developed in the chapter culminating in the presentation of an equation describing the molecular effusion rate from a Knudsen oven; Knudsen ovens are the principle molecular beam sources in MBE. Finally dopant incorporation mechanisms in the MBE growth of III-V semiconductors are discussed in the latter part of the chapter.

In addition to describing the MBE vacuum system and diagnostic equipment, chapter 3 discusses the growth and characterisation of unintentionally doped InP grown by MBE.

Chapter 4 is concerned with Zn doping of MBE grown InP. The design, performance and operation of a specially constructed low energy (200eV → 2keV) Zn ion source which was incorporated in the MBE system as a source of Zn ions are described. The growth and characterisation of Zn ion and Zn (neutral) doped InP films are discussed.

Be doping in MBE of InP is considered in chapter 5. The growth and characterisation of Be doped InP films are reported.

Chapter 6 describes the design and operation of a deep level transient spectroscopy (DLTS) system which was constructed in order to detect the presence of deep level carrier traps in MBE grown InP material. The results obtained from DLTS measurements on molecular beam epitaxial InP are discussed.

Finally, chapter 7 contains a concluding discussion on the results obtained in this project together with suggestions for further work in the field.

CHAPTER 2.

CHAPTER 2

BASIC PRINCIPLES GOVERNING THE GROWTH OF III - V COMPOUNDS BY MOLECULAR BEAM EPITAXY

Although most of the studies of growth kinetics due to the interaction of molecular beams with crystalline surfaces have been limited to GaAs the fact that MBE growth of GaP [2.1], $Al_xGa_{1-x}As$ [1.1], $In_xGa_{1-x}As$ [2.2] and other III - V compounds including InP has been achieved using similar molecular flux conditions suggests that the basic growth mechanisms are similar for most III - V compounds. The following chapter describes the kinetics of epitaxial growth of III - V compounds from molecular beam sources with particular emphasis on dopant incorporation mechanisms (section 2.5).

2.1 Species Evolved in the Evaporation of III - V Compounds

In order to understand the kinetics of epitaxial growth of III - V films from molecular beam sources a knowledge of both the Knudsen (equilibrium) evaporation and Langmuir (free) evaporation behaviour of the particular III - V material involved is necessary. III - V compounds for which the Langmuir and Knudsen evaporation behaviour have been established include GaAs and InP. Farrow [2.3] has studied the free evaporation behaviour of the (100) surface of InP using modulated beam mass spectrometry (MBMS) techniques. This method involves

interupting the evaporated flux with a mechanical chopper before it enters the mass spectrometer and the use of signal averaging techniques to discriminate the direct beam flux from the crystal from background molecules. Farrow [2.3] found that only In and P_2 are evolved from a (100) InP surface when the crystal is heated in an U.H.V. environment and that the free evaporation is congruent, ie P_2 flux = 1/2 In flux, up to $365 \pm 10^{o}C$. At temperatures above $\sim 365^{o}C$ there is a disproportionate loss of P_2, the ratio P_2/In evolved being strongly temperature dependent as shown in Fig. 2.1. Farrow [2.3] has also found the maximum congruent evaporation rate from the (100) InP surface under free evaporation conditions to be $\sim 10^{-5}$ monolayer/sec. In a similar study Foxon et al [2.4] found a maximum congruent evaporation temperature for GaAs of $657^{o}C$ (below which As_2 flux = 1/2 Ga flux) together with a maximum congruent evaporation rate from the (100) GaAs surface of $\sim 10^{-1}$ monolayer/sec. The maximum congruent evaporation temperature of a crystal is an important parameter in relation to in-vacuo heat cleaning of substrates prior to film deposition. Cho and Panish [2.5] have shown from Auger electron spectroscopy (AES) studies that heating (100) GaAs substrates in-vacuo to $525 - 535^{o}C$ results in the complete removal of oxygen from the surface while carbon contamination is reduced to a few percent of a monolayer. Thus (100) GaAs substrates can be successfully heat-cleaned at temperatures well within the (100) GaAs congruent evaporation temperature

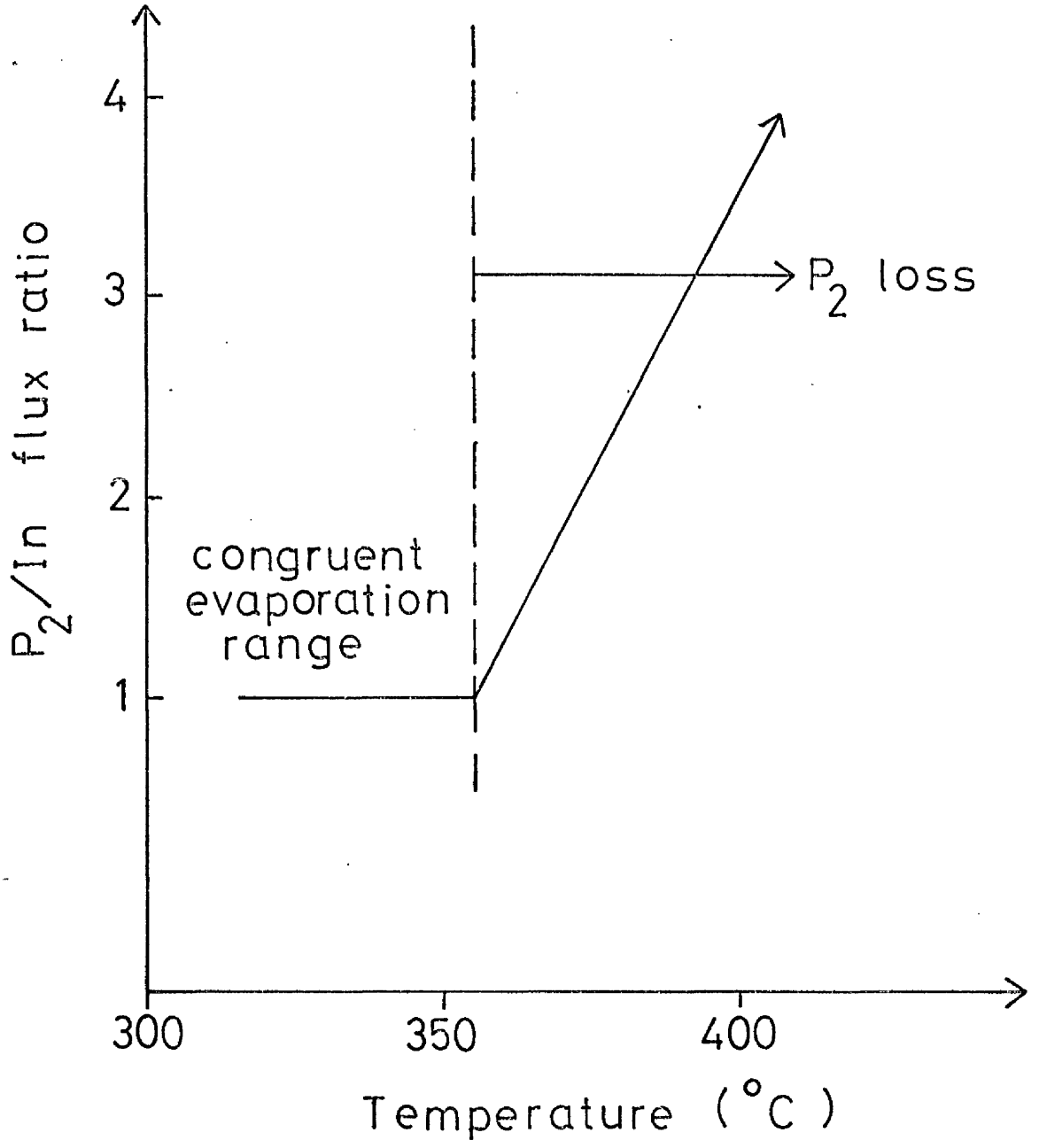

FIG. 2.1 : Langmuir evaporation of (100) InP. (Ref. 2.1)

range. In the case of InP, however, simple in-vacuo substrate heat-cleaning is not possible since at temperatures > 365°C there is a preferential loss of phosphorus from an InP surface. Farrow, [2.6] however, has shown that InP surfaces can be stabilised at temperatures > 450°C by impinging a compensating flux of either P_2 molecules, generated from a Knudsen oven containing InP, or P_4 molecules evaporated from an oven containing red phosphorus. Preliminary AES studies indicated that this technique results in the removal of oxygen contamination from InP surfaces at temperatures > 400°C although epitaxial InP deposition was not demonstrated onto substrates cleaned in this manner. More recently Davies et al [2.7] and Cheng et al [2.8] have shown using AES analysis that InP substrate surfaces which are passivated with an oxide following the ex-situ preparation can be successfully heat cleaned at temperatures > 500°C under exposure to an As_4 molecular beam. These authors subsequently deposited epitaxial $In_{0.53}$ $Ga_{0.47}$ As onto InP substrates prepared in this manner.

The evaporation of InP under Knudsen conditions, ie with the vapour and condensed phases in equilibrium, has been studied by Farrow [2.3] using MBMS techniques. P_2 was found to be the dominant species evaporated from a Knudsen oven containing InP in the temperature range 545 - 657°C although significant evaporation fluxes of In and P_4 were

also detected. At an oven temperature of $\sim 650^{o}C$ the ratio of dimer (P_2) to tetramer (P_4) molecules emanating from an InP Knudsen oven was found to be $\sim 9 : 1$. InP is the only III - V compound so far examined where such a tetramer pressure has been identified under Knudsen effusion conditions (Foxon et al [2.9]). In view of the absence of P_4 in the Langmuir evaporation flux from InP and the absence of tetramers in both the Knudsen and Langmuir evaporation fluxes from other III - V compounds such as GaAs and GaP the P_4 pressure in the InP oven is attributed to $P_2 + P_2$ association reactions on the walls of the oven (Farrow [2.3]). Significant dimer evaporation fluxes from GaAs and GaP are only detectable at temperatures around $950^{o}C$ (Foxon et al [2.9]), ie $300^{o}C$ higher than the normal InP oven temperature, and consequently the $X_4 \rightleftarrows 2X_2$ equilibrium lies further to the right in GaAs and GaP ovens than in an InP oven.

In the work reported in this thesis a Knudsen oven containing InP was used throughout as the source of phosphorus and hence a predominately P_2 molecular beam was evaporated. Also, typical InP substrate growth temperatures were $\leqslant 360^{o}C$, ie just below the congruent evaporation temperature limit of the material.

2.2 Knudsen Effusion Theory

The sources of molecular beams in MBE experiments, with the exception of specially designed electron-gun sources which are used to evaporate very low vapour pressure

elements such as Si, consist of small cylindrical graphite or boron nitride ovens which contain species having vapour pressures typically around 10^{-3} Torr. Molecular effusion, as opposed to turbulent effusion, takes place from such ovens if their aperature radius r is adjusted so that $r < \lambda$, where λ is the mean free collision path of the molecules within an oven. Under such conditions the number of molecules dQ which will emerge per second from an oven travelling in solid angle dw at angle θ relative to a normal to the aperture plane is given by

$$dQ = (dw/4\pi)\, n\bar{v}\, A_s \cos\theta \qquad (2.1)$$

where n is the number of molecules per unit volume, $\bar{v}$ is the mean molecular velocity inside the oven, and A_s is the aperture area. By integrating equation 2.1 over a 2π solid angle in the forward direction, the total number of molecules Q emerging per second is given by

$$Q = \frac{1}{4}\, n\, \bar{v}\, A_s \cos\theta \qquad (2.2)$$

The cosine law of molecular effusion implied by equation 2.2 was first established by Knudsen (2.10).

From kinetic gas theory

$$\bar{v} = 2\,(2kT/\pi M)^{1/2} \qquad (2.3)$$

$$\text{and } n = p/kT \qquad (2.4)$$

where M is the mass number of the evaporant, and p and T are the vapour pressure and temperature inside the oven,

respectively.

By substituting equations 2.3 and 2.4 into equation 2.2, Q can be written as

$$Q = \frac{1}{(2k\pi)^{1/2}} \frac{p A_s}{(MT)^{1/2}} \cos\theta \qquad (2.5)$$

If a detector, which in the case of MBE experiments is a substrate, intercepts a beam of molecules at a distance d from the source aperture, the number of molecules I which strike the detector per second is given by

$$I = \frac{1}{(2k\pi)^{1/2}} \frac{p A_s}{(MT)^{1/2}} \frac{A_d}{(\pi d^2)} \cos\theta \qquad (2.6)$$

Assigning the units of p(Torr), M(amu), T(K), A_s and A_d (cm^2) and d(cm) to the terms in equation 2.6, I can be written as

$$I = 1.118 \times 10^{22} \frac{pA_sA_d}{d^2(MT)^{1/2}} \cos\theta \quad \text{molecules } s^{-1} \qquad (2.7)$$

Equation 2.7 is normally written in the form of a flux equation, the flux of molecules J arriving at a substrate of area A_d being given by

$$J = 1.118 \times 10^{22} \frac{pA_s}{d^2(MT)^{1/2}} \cos\theta \quad \text{mol.cm}^{-2}\ s^{-1} \qquad (2.8)$$

In the above analysis a thin-walled aperture was assumed, however, if the aperture is a canal of appreciable length, the molecules which start to emerge at a considerable angle will strike the canal wall and have a smaller chance of escaping, and even if they do so it will probably be at a different angle. Thus the angular distribution of the emergent beam is changed considerably from the cosine distribution implied by equation 2.8. Clausing [2.10] has calculated the angular distribution for a canal-like aperture whose length equals twice the radius. This distribution is illustrated in Fig. 2.2 which also shows the angular distribution to be expected from the cosine law (equation 2.8). As can be seen from the figure a canal-like aperture has a focussing effect on the emerging beam although the beam intensity in the direction of the canal is undiminished. Angular distributions have been calculated for a number of canal length to radius (L/r) ratios [2.11], the focussing effect, ie beam narrowing, being found to increase with increasing L/r ratios.

In this work open ended cylindrical boron nitride crucibles were used which had a L/r ratio of 16 (L = 40mm, r = 2.5mm). The theoretical spatial distribution of the flux eminating from such ovens is shown in Fig. 2.3 together with the spatial distribution expected from the cosine law, illustrating that both

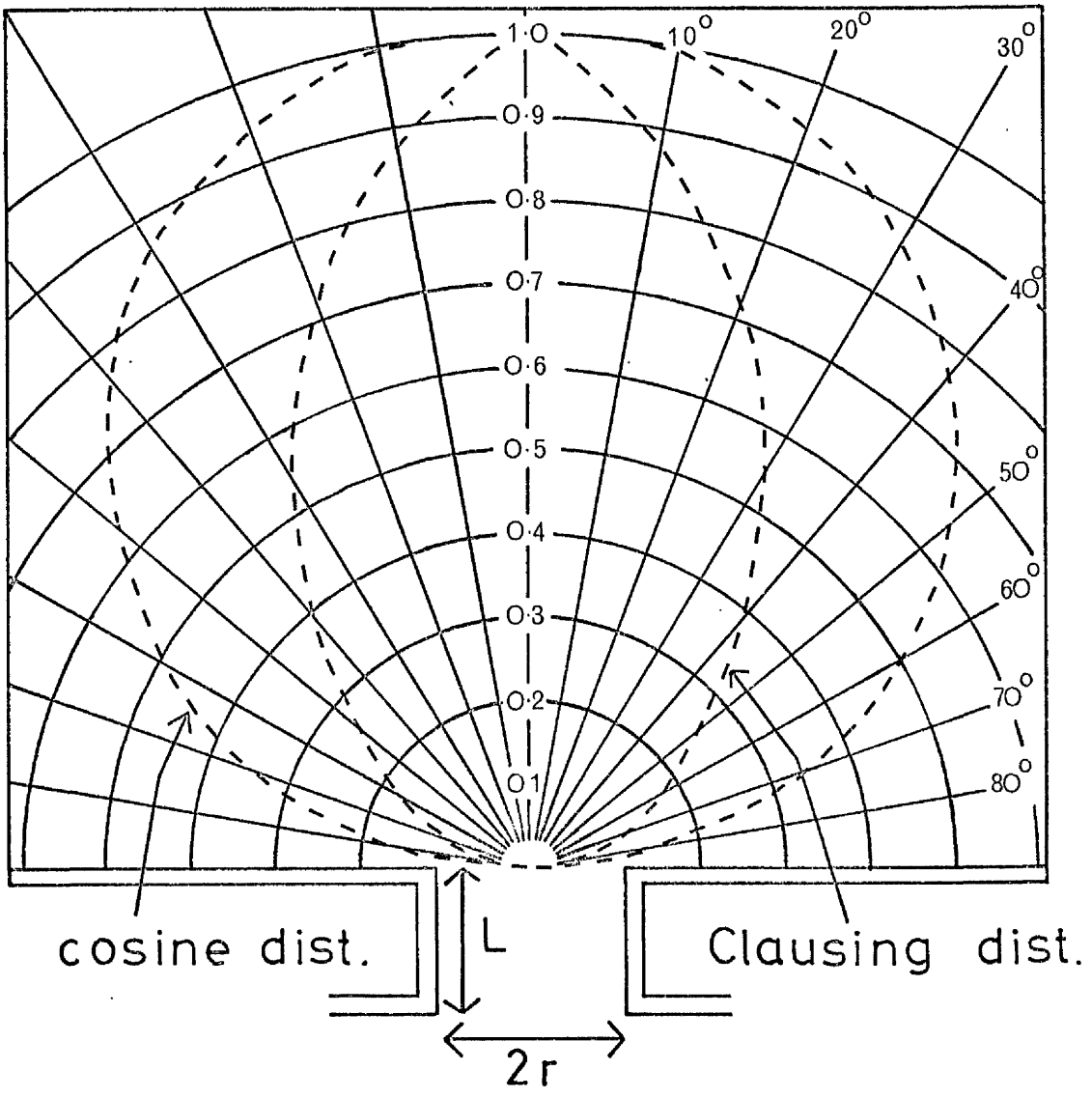

FIG. 2.2 : Angular distributions of a molecular beam effusing through a small canal.

$L \simeq 0 \rightarrow$ cosine dist.^{n}

$L/r = 2 \rightarrow$ Clausing dist.^{n}

(Ref. 2.10)

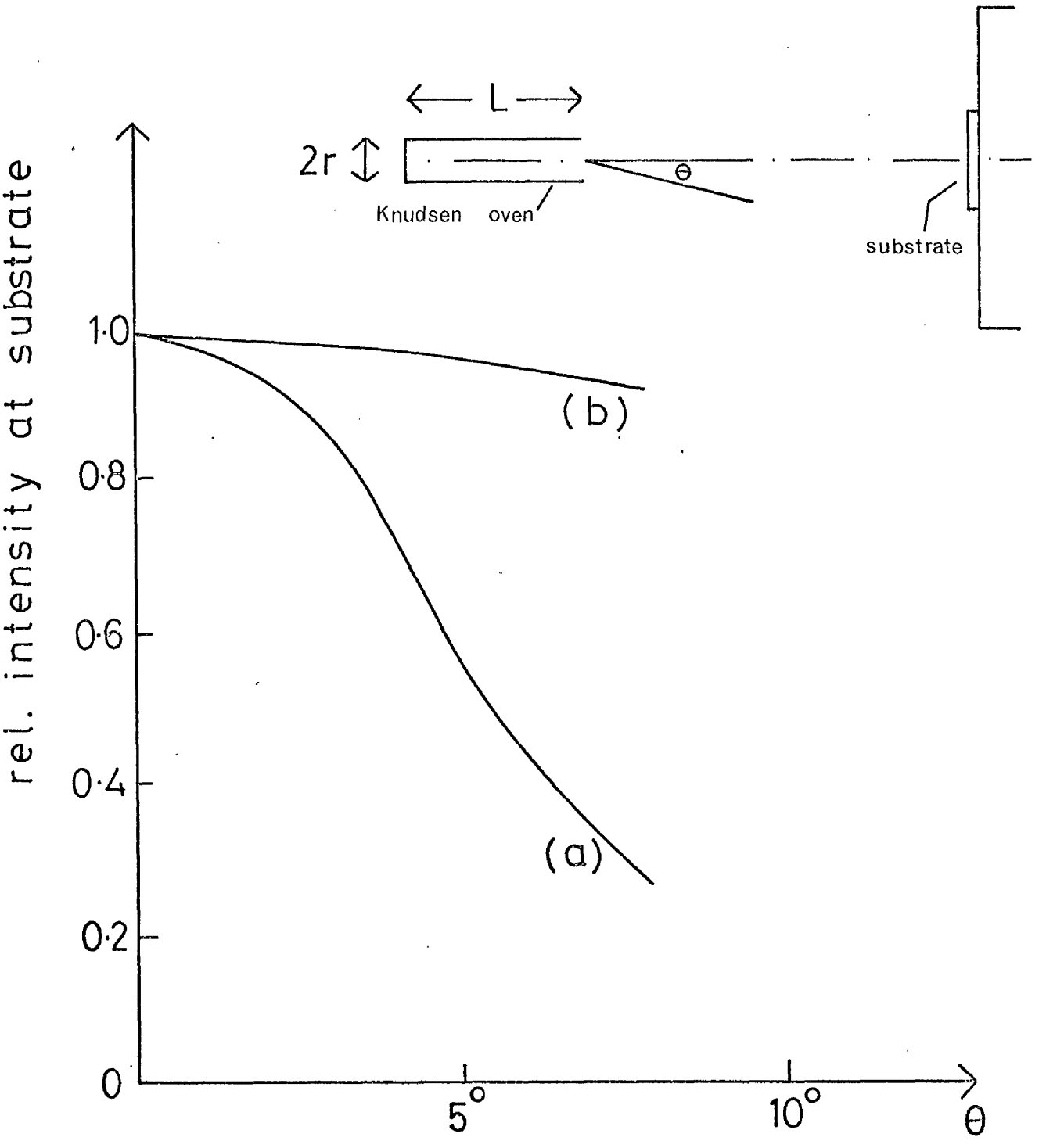

FIG. 2.3 : Spatial distribution of the flux from a Knudsen oven.

(a) $L/r = 16$

(b) Cosine dist^{n}

distributions are similar for $\theta < 3^{o}$. Also, 10mm x 5mm substrates were situated 10cm from the oven orifices in this work and therefore the maximum subtended angle θ over the substrate surface area was 2.8^{o}. Hence the flux arriving at the substrate can be approximated to that given by equation 2.8. Furthermore, for small values of θ, $\cos\theta \approx 1$ and therefore flux levels are approximately given by

$$J = 1.118 \times 10^{22} \frac{pA_s}{d^2(MT)^{1/2}} \quad mol.cm^{-2}\ s^{-1} \qquad (2.9)$$

Equation 2.9 is referred to as the Knudsen equation throughout the remainder of this thesis.

2.3 Kinetics of Epitaxial Growth by the Interaction of Group III and Group V Element Molecular Beams

The two most commonly used procedures for the preparation of III - V Compounds by MBE are described in the following, using GaAs as an example. The first such procedure employs beams of As_4 derived from an elemental arsenic source and Ga, while the second uses As_2 usually obtained from a GaAs source but more recently with an $As_4 \rightarrow As_2$ cracking cell [2.12] and Ga, which in each system impinge on a heated GaAs substrate where interaction occurs. The interaction kinetics of As_4 and Ga on (100) GaAs and As_2 and Ga on (100) GaAs have been studied using MBMS techniques by Foxon and Joyce [2.13, 2.14]. In addition, Farrow [1.29] has investigated the

interaction kinetics of P_2 and In on (100) InP using MBMS techniques but to date the kinetics of the In - P_4 system have not been reported although Kawamura et al [2.15] have grown (100) InP epitaxial films using In and P_4 beams. The crucial results from the interaction kinetics experiments which have been reported are summarised in sections 2.3.1 - 2.3.3.

2.3.1 (100) GaAs/Ga-As_4 System

In the absence of a Ga flux As_4 has a zero sticking coefficient but a measurable surface lifetime in the temperature range 300 - 450K, the sticking coefficient being defined as the ratio of chemisorbed to incident molecules. If a Ga surface population is produced by a coincident Ga beam, S_{As_4} becomes finite and temperature dependent, tending to unity as the substrate is increased above 300K. With a coincident Ga flux, As_4 has a temperature independent sticking coefficient between 450K and 600K, but it is a function of the Ga beam intensity, J_{Ga}. The crucial results are that the sticking coefficient of As_4, S_{As_4}, is always < 0.5, even when $J_{Ga} >> JAs_4$, (the As_4 flux); secondly, when $J_{Ga} << J_{As_4}$, one As atom sticks on the GaAs surface for every Ga atom supplied; and finally, when $J_{Ga} >> J_{As_4}$, the desorption rate of As_4 is second order with respect to its adsorption rate, but for $J_{Ga} << J_{As_4}$ a first order dependence is involved. These results can be explained by a process of dissociative chemisorption, with a pairwise interaction

of As_4 molecules absorbed on adjacent Ga lattice sites. When the As_4 surface population is small compared to the number of Ga sites the rate limiting step is the encounter/reaction probability between As_4 molecules leading to second order kinetics. As the As_4 surface population is increased, there is an increasing probability that an arriving molecule will find adjacent sites occupied and the desorption rate becomes proportional to the number of molecules being supplied, ie a first order process. To summarise, at temperatures > 450K Ga adatoms (adsorbed Ga atoms) only control the condensation, dissociation and reaction of As_4 molecules but below ∿ 400K As_4 molecules are not adsorbed dissociatively and consequently growth of GaAs from Ga and As_4 beams is not possible below ∿ 400K. This minimum temperature for epitaxy has been verified experimentally by Neave and Joyce [2.16].

2.3.2 (100) GaAs/Ga - As_2 System

At substrate temperatures > 600K the sticking coefficient of As_2, S_{As_2}, is a function of the arrival rate of Ga atoms, and when $J_{Ga} < J_{As_2}$ one As atom sticks on the GaAs surface for each Ga atom supplied, while for $2 J_{Ga} > J_{As_2}$, S_{As_2} is unity (c.f. $S_{As_4} = 0.5$ for the equivalent situation). Below 600K, the behaviour of As_2 molecules becomes more complex in that they undergo a surface association reaction, leading to the desorption

of As_4 molecules by a first order process with respect to J_{As_2}. Thus, below 600K growth of GaAs from Ga and As_2 beams is not possible.

2.3.1 (100) InP/In - P_2 System

The sticking coefficient of In, S_{In}, in the absence of a P_2 surface population is ≈ 1 over the InP substrate temperature range 300 - 638K whereas the sticking coefficient of P_2, S_{P_2}, in the absence of an In surface population is < 0.01. However, with In and P_2 beams coincident on a (100) InP surface, S_{P_2} ≈ 1. Thus the P_2 condensation is due to P_2 adsorption, dissociation and subsequent reaction with In adatoms to form InP. The temperature at which $P_2 + P_2$ association takes place, leading to the desorption of P_4 molecules, and hence an implied minimum epitaxial growth temperature has not been found by MBMS techniques for (100) InP growth from In and P_2 beams. Norris [1.31], however, has reported a minimum substrate temperature for InP epitaxy from In and P_2 beams of ∿ 100°C by RHEED observations, deposited films appearing polycrystalline for growth temperatures < 100°C.

From the results discussed above in sections 2.3.1 - 2.3.3. it is apparent that above a minimum substrate temperature, which is particular to each material and also the group V species involved, epitaxial growth by the interaction of coincident group III and group V element

molecular beams is controlled by the arrival rate or flux level of the group III element (J_{III}) with stoichiometric growth taking place provided $J_V > J_{III}$, where J_V is the group V element flux level. The film growth rate, G_r, therefore is limited entirely by J_{III} and is given by

$$G_r = J_{III}/\alpha \qquad (2.10)$$

where α is the surface density of group III atoms in a monolayer of the III-V crystal. J_V is usually set so that $J_V : J_{III} = 5$ to 20 for the case of group V dimer species [1.1] in order that stoichiometric growth is ensured, with excess group V molecules re-evaporating from the surface. As discussed in the following section a large group V element overpressure ensures growth under the so-called, 'group V element - stabilised' condition. Higher group V element flux levels still are required when the growth temperature is greater than the maximum congruent evaporation temperature of the particular III-V compound involved since a certain overpressure of the group V element is necessary in order to prevent the decomposition of the substrate crystal.

2.4 Surface Reconstruction in III-V Compounds during MBE Growth

Surface reconstruction is a re-ordering of the arrangement of the outermost layer of atoms at the surface of a crystal, often leading to a translational symmetry lower than that of the bulk crystal. The effect is particularly pronounced in covalently bonded crystals,

such as the III-V compounds, where the bonds are highly directional. Consider the case, for example, of (100) GaAs which is the most extensively characterised III-V compound in terms of surface structures. Since GaAs is composed of alternate layers of Ga and As atoms in the (100) direction, the surface may be terminated in either Ga or As atoms. As shown by Cho [2.17] surface structures stabilised with either atoms may be produced during MBE growth by controlling the relative arrival rates of Ga and As atoms or the substrate temperature. The most commonly observed reconstructed surface structures on (100) GaAs are (2 x 4) and C (2 x 8) for As - stabilised surfaces, and a rotation of 90^{o} from the As - stabilised structures forming (4 x 2) and C (8 x 2) structures for Ga - stabilised surfaces. Schematic diagrams of (2 x 4) and C (2 x 8) surface structures are shown in Fig. 2.4. As can be seen from the figure surface atoms in the case of the (2 x 4) surface structure have twice the periodicity of bulk atoms in the $[1\bar{1}0]$ direction and 4 times the bulk periodicity in the orthogonal $[\bar{1}\bar{1}0]$ direction, hence such a structure is labelled (2 x 4); the C (2 x 8) structure labelling is self-evident from Fig. 2.3. Such surface structures are observed during MBE growth using the reflection high energy electron diffraction (RHEED) technique in which an electron beam (3keV → 50keV) is incident at a glancing angle of incidence ($< 3^{o}$) to the surface of the crystal (see, for example, Cho and Arthur [1.1]). If the surface is

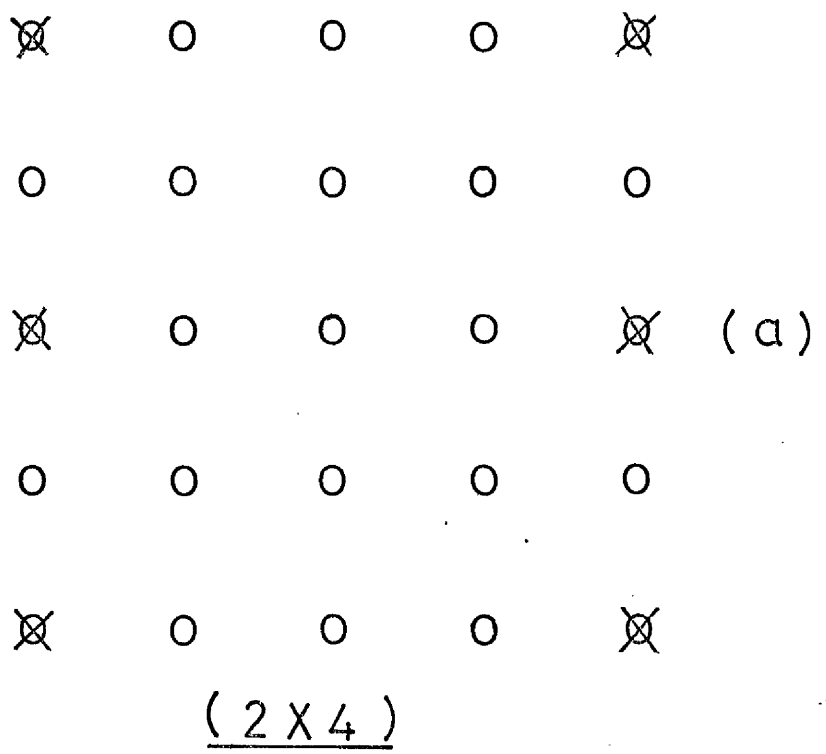

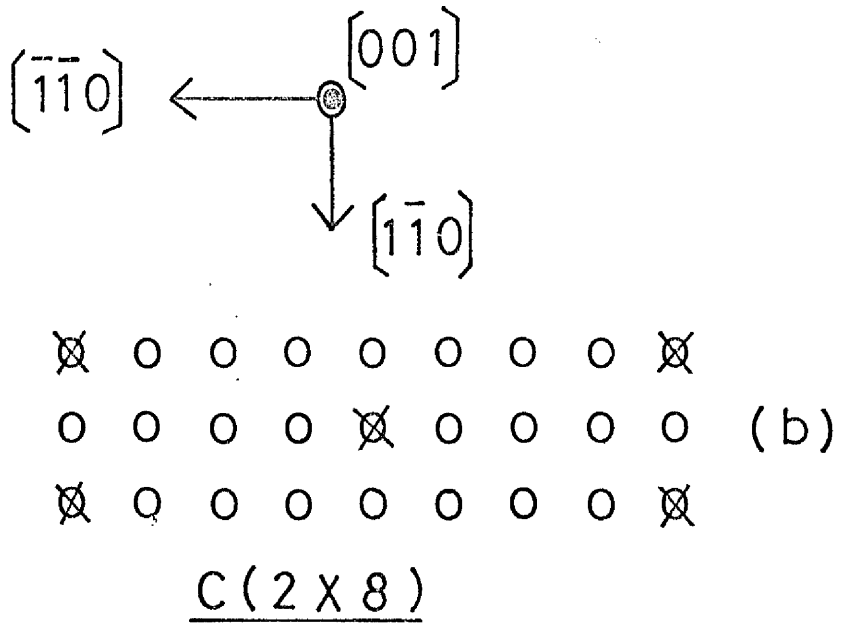

FIG. 2.4 : Surface structures.

o Bulk atoms

X Surface atoms

single crystal and atomically flat diffraction lines are observed on a phosphor screen positioned directly opposite the electron gun. Surfaces which reconstruct to a lower symmetry than the (1 x 1) bulk crystal give rise to extra diffraction lines in the RHEED pattern and consequently the symmetry of the surface unit mesh can be determined by recording the RHEED pattern with the electron beam incident in two orthogonal azimuths. Although the effect of surface reconstruction on epitaxial film properties is not fully understood, the observation of reconstructed surfaces such as the (2 x 4) and (4 x 2) structures is a useful means of obtaining well characterised growth conditions.

2.5 Dopant Incorporation Mechanisms in III-V Compounds Grown by MBE

Doping of MBE films is achieved by impinging suitable elements at the substrate in the form of molecular beams coincident with the main constituent - element beams. There is considerable difficulty, however, in trying to predict which elements will be suitable for MBE in that the doping process necessarily involves both the adsorption of the impurity on the surface and its subsequent incorporation into the bulk on a suitable lattice site as the film grows. Since kinetic processes in MBE are dependent on both temperature and surface stoichiometry each potential dopant must be tested empirically under particular growth conditions. The III-V compound most extensively studied to date in terms of dopant incorporation

has been GaAs (see, for example, Joyce and Foxon [2.18]). The GaAs work has highlighted the unpredictable nature of dopant incorporation in MBE films and also the fact that there are two processes which must be understood in order to evaluate the mechanisms involved in producing doped MBE films. The first of these processes is the interaction behaviour of the dopant with a substrate surface, especially in the presence of larger constituent - element fluxes while the second process is the incorporation and extent of electrical activity of the dopant in the growing film. Several elements have been tested as potential dopants in MBE grown GaAs and the results from these studies are now summarised.

Tin. [2.19] Sn, a group IV element, has a unity sticking coefficient on GaAs and is incorporated as a donor under normal MBE growth conditions. Hall - effect mobility measurements indicate that there is very little compensation in Sn-doped GaAs films at doping levels between 10^{17} and 10^{18}cm $^{-3}$, however, Sn has a tendency to segregate at the growth surface at MBE growth temperatures > 550^{o}C.

Silicon. [2.20] Although normally an amphoteric dopant in GaAs, in MBE grown material Si is incorporated predominately as a donor, with a degree of compensation only marginally higher than that produced by Sn. Si has a unity sticking coefficient on GaAs at typical MBE growth temperature ($\sim$ 600^{o}C) and produces n - type films with free-carrier concentrations in the range 10^{16} - 5 x

10^{18} cm^{-3} depending on the Si flux level with no apparent tendency to segregate. The major disadvantage associated with the use of Si as an n - type dopant in MBE is the reactive nature of the element at the high temperatures (∿ 1500K) required to produce an adequate vapour pressure in a Knudsen oven containing Si.

Germanium. [2.21] Ge is an amphoteric dopant in MBE grown GaAs, the site occupied by the impurity in the lattice being critically dependent on growth conditions. If the growth conditions are such that the Ga-stabilised surface structure is obtained (see section 2.4), Ge is incorporated predominately as an accepter, ie on As sites, while under As-stabilised growth conditions Ge is incorporated predominately as a donor, presumably on Ga sites. Ge-doped films are highly compensated, however, particularly for the case of n - type films and therefore Ge is not particularly useful as a practical dopant.

Magnesium. [4.14] Mg, a group II element, is chemically incorporated into GaAs with a near unity sticking coefficient but only one Mg atom in 10^5 is electrically active. It is interesting to note that the level of electrical activity of incorporated Mg (producing p-type material) increases rapidly with Al content in the ternary compound $Al_x Ga_{1-x} As$ [4.15]. Beyond speculation that Mg might diffuse interstitially and occupy interstitial sites, no experimental information is available on its incorporation behaviour in MBE grown GaAs.

Manganese. [2.22] Manganese, a group II element, is readily incorporated in an electrically active form provided As-stabilised growth conditions are maintained but it forms a deep acceptor level (113 meV above the valence band edge) and hence is not fully ionised at room temperature. Film perfection is found to deteriorate at doping levels > 10^{18} acceptors cm^{-3} due to a strong interaction of Mn with Ga during growth.

Beryllium. [4.2] Be, a group II element, is an ideal p - type dopant in MBE grown GaAs having a near unity sticking coefficient and an atom/free-carrier ratio in GaAs films of ∿ 1. P-type doping levels as high as 5×10^{19} cm^{-3} have been achieved using Be.

Tellurium. [2.23] Te, a group VI element, has a unity sticking coefficient on GaAs at typical MBE growth temperatures. S_{Te} is unexpectedly high since Te is a very high vapour pressure element. Te, however, displaces arsenic from an As - stabilised structure by forming the stable compound GaTe and thus is unsuitable as a dopant.

Of other potential dopants, the group II elements, Zn and Cd, have zero sticking coefficients on GaAs at temperatures > $100^{o}C$ (see chapter 4 for a fuller discussion of Zn doping) while the group VI elements, S and Se, have proved useful n - type dopants when evaporated as lead compounds (PbS, PbSe) from so-called captive sources [2.24].

CHAPTER 3.

CHAPTER 3

GROWTH OF UNINTENTIONALLY DOPED InP BY MOLECULAR BEAM EPITAXY

3.1 Introduction

The MBE system to be described here was previously used by Norris [3.1] to grow unintentionally doped InP and by Sullivan [3.2] to grow both unintentionally doped and Sn-doped InP. As mentioned in chapter 1, the in-vacuo substrate cleaning technique used by these authors which permitted the subsequent growth of epitaxial InP consisted of argon-ion sputtering followed by annealing, the precise conditions being a 30 minute exposure to 500eV argon ions with an ion-current density at the substrate $\sim 1\mu A cm^{-2}$ followed by a 30 minute anneal at 250-300°C, the process being repeated three times. Norris [3.1] has shown that this cleaning technique results in a smooth crystalline surface as evidenced by the observation of a streaky unreconstructed or bulk-like RHEED pattern following the cleaning process. In addition, (2 x 4) surface reconstruction has been observed by Norris [3.1] during InP film deposition in the substrate temperature range 300 - 380°C using typical flux levels during film growth of

$$J_{In} = 3 \times 10^{14} \text{ cm}^{-2} \text{ s}^{-1}$$

and $$J_{P_2} > 10^{15} \text{ cm}^{-2} \text{ s}^{-1}$$

As discussed in chapter 2, section 2.4, the (2 x 4) reconstructed surface is widely reported for GaAs as being indicative of As-stabilised growth conditions. Thus, by

direct analogy the flux levels given above are assumed to result in the growth of epitaxial InP under P-stabilised growth conditions. All the InP films grown by the author, the characteristics of which are reported in later sections were deposited under these P-stabilised growth conditions using In and P_2 fluxes similar to those given above. Also, the argon-ion sputtering and annealing substrate cleaning technique detailed above was employed throughout.

In addition to describing the MBE system and diagnostic equipment chapter 3 discusses the growth and characterisation of unintentionally doped molecular beam epitaxial InP. Plasma reflectivity measurements and electron channelling analysis have been used for the first time in the assessment of InP grown by MBE, the results obtained being reported in section 3.7.3. In section 3.8 detrimental effects associated with the argon-ion sputtering and annealing substrate cleaning process are discussed.

3.2 MBE System and Diagnostic Equipment

The stainless-steel ultra-high vacuum system used in this work is shown in Fig. 3.1 while the MBE growth chamber is illustrated schematically in Fig. 3.2. The pumping system consisted of a 600 Ls^{-1} diffusion pump topped with a Vacuum Generators CCT150 chevron-baffled cold trap and backed by a 200 L min^{-1} rotary pump. A base pressure of $\sim 2 \times 10^{-9}$ Torr was obtained following a 6 hour bakeout of the system at $\sim 150^{o}C$, the pressure

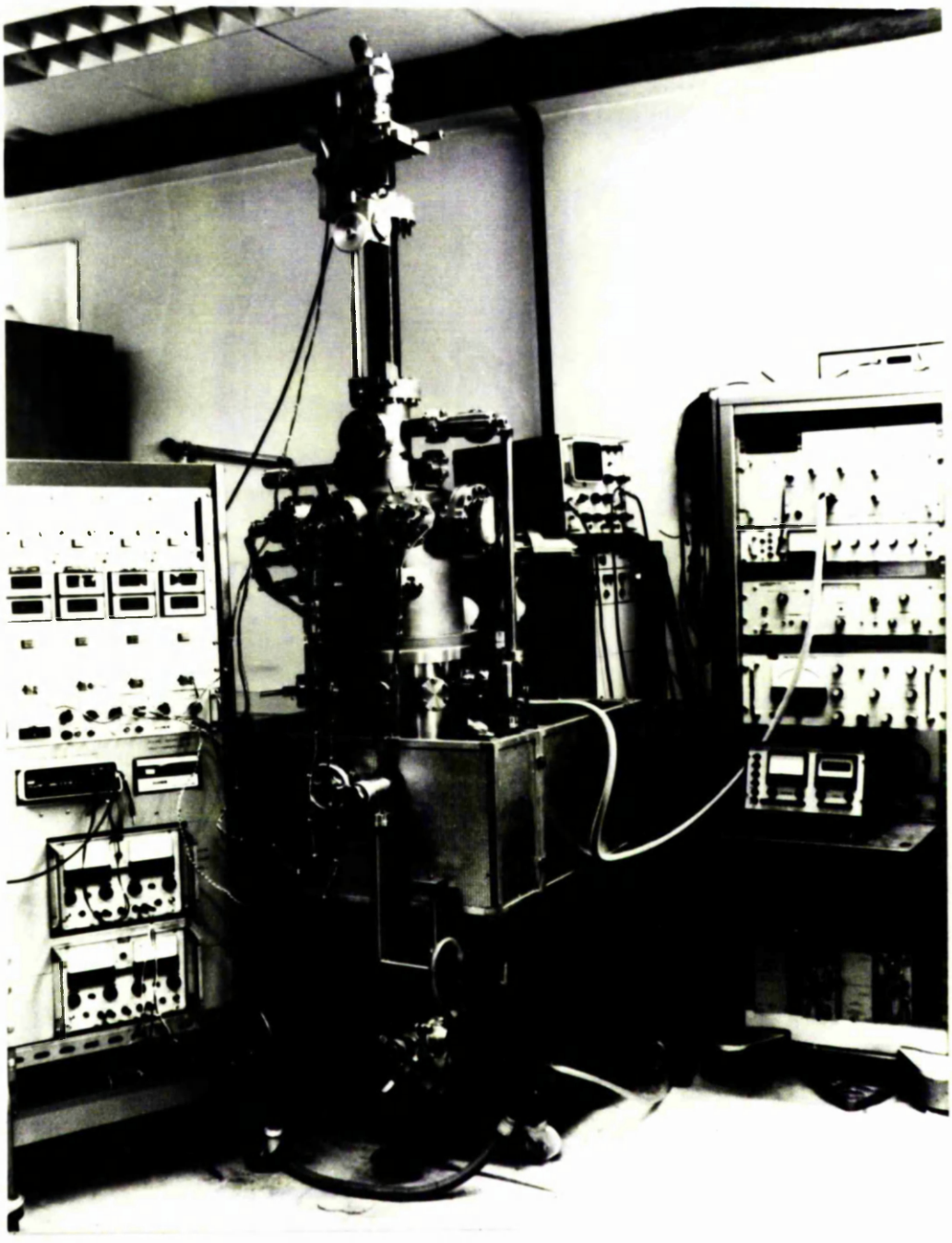

FIG. 3.1 : PHOTOGRAPH OF MBE VACUUM SYSTEM

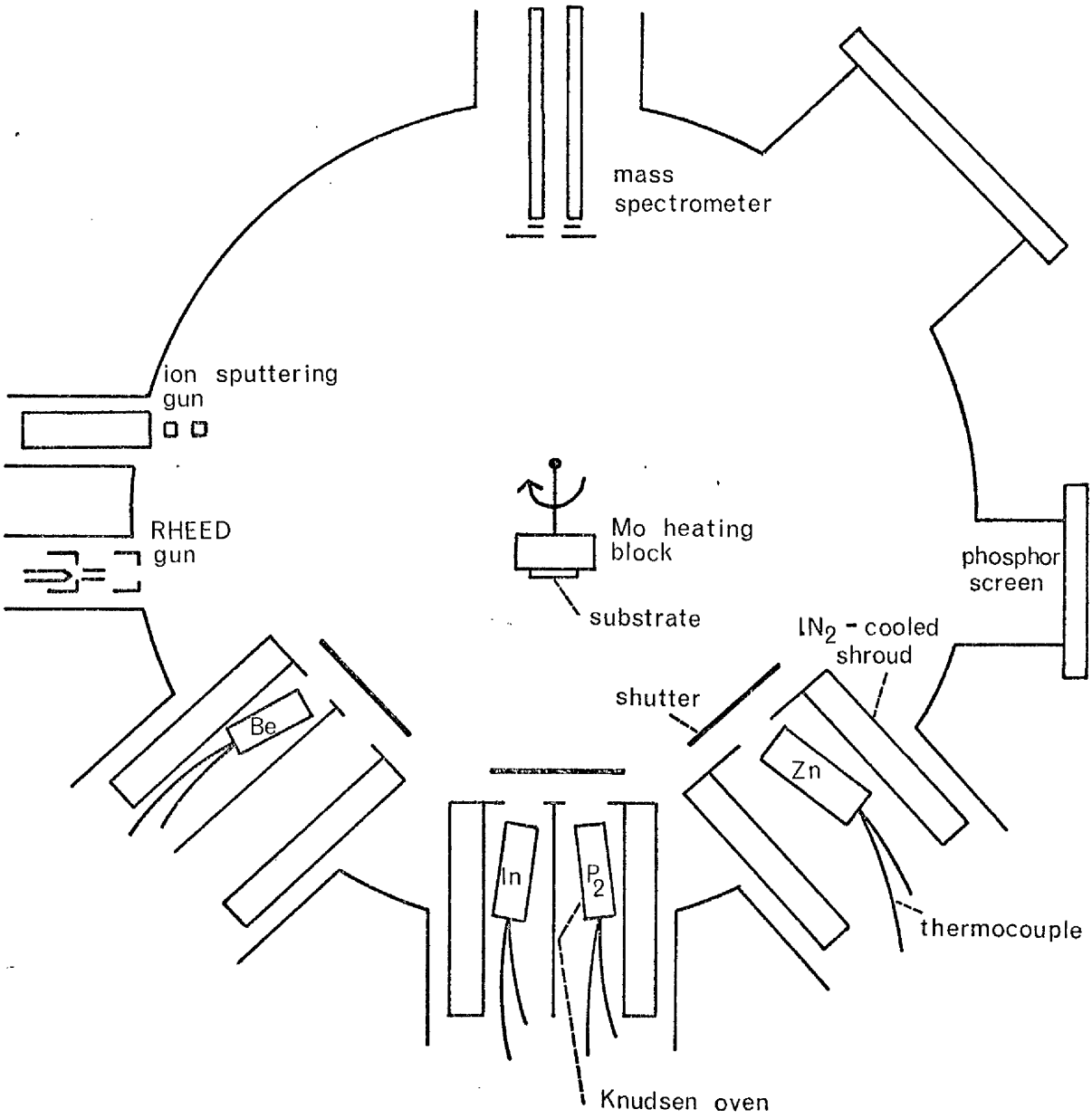

FIG. 3.2 : Schematic of MBE growth chamber.

prior to the bakeout being $\sim 5 \times 10^{-8}$ Torr due principally to the presence of water vapour. The ultimate base pressure was $\sim 5 \times 10^{-10}$ Torr achieved using liquid nitrogen-cooled cryopanels located in the service well of the vacuum system. A mass spectrum of the residual gases recorded using a Vacuum Generators Q8 quadrupole mass spectrometer is shown in Fig. 3.3, indicating carbon monoxide (28 amu) to be the main constituent of the background gases. Also present in the residual gas spectrum are argon (from the argon ion sputtering process) and phosphorus which was never completely removed.

Freshly prepared substrates (see section 3.5) were attached to a molybdenum heating block through the loading port shown in Fig. 3.4. The loading port was contained in a small chamber at the top of the vacuum system and could be isolated from the main growth chamber by means of an interlock valve. The linear motion drive shown in Fig. 3.4 controlled the position of a flap valve which when in the horizontal position pressing onto a Viton O-ring seal allowed the pressure in the system to be maintained at $\sim 5 \times 10^{-7}$ Torr while the small loading chamber was at atmospheric pressure. The vacuum interlock facility minimised both the turn-around time and the risk of atmospheric contamination. Following an initial bakeout of the system 4 to 5 growth runs could be performed using the flap valve to re-load new substrates, thus obviating the need to bake the system after each re-loading process. The 4 to 5 run limit which

Main Peaks :- $2 : H_2^+$, $14 : N_2^{++}/CH_2^+$

$18 : H_2O^+$, $28 : CO^+/N_2^+$

$31 : P^+$, $40 : Ar^+$

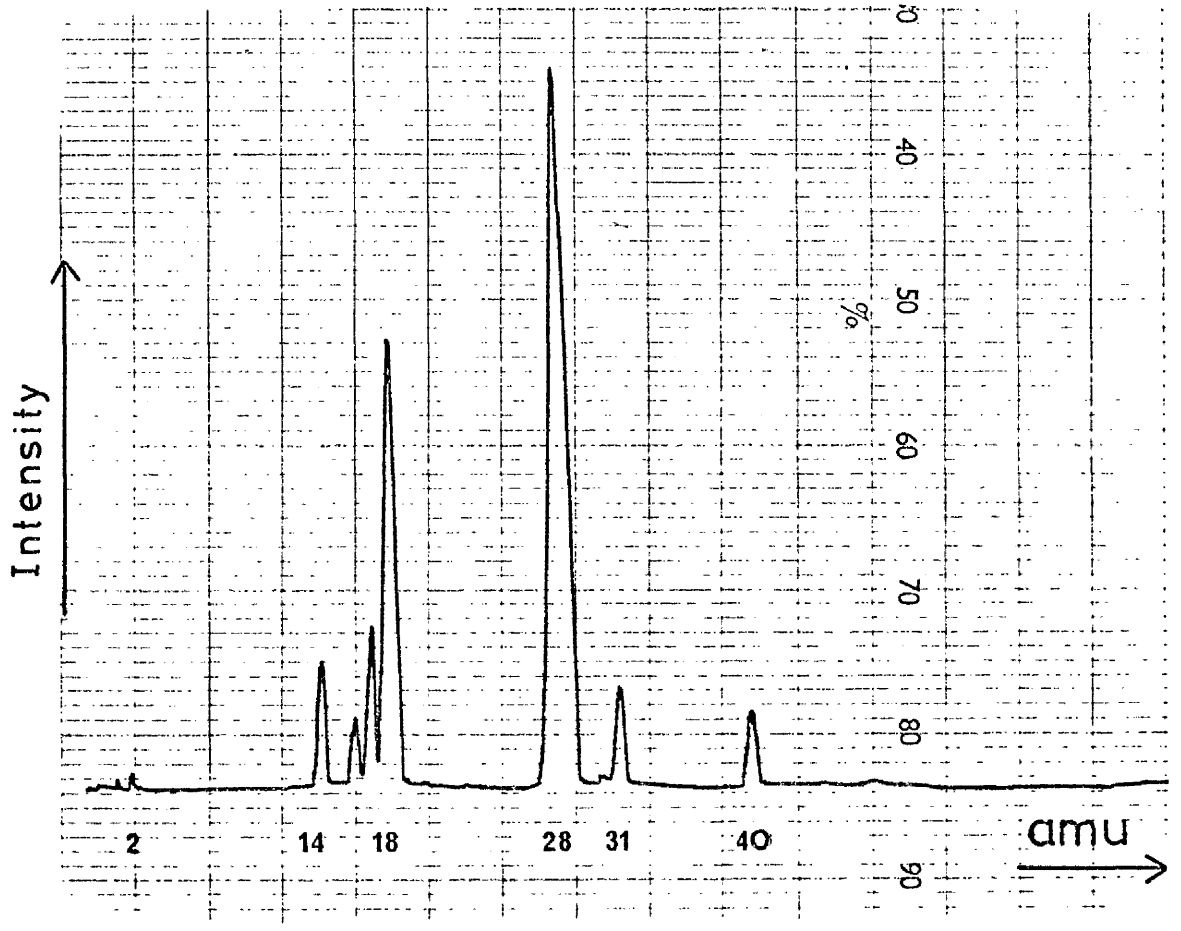

FIG. 3.3 : RESIDUAL GAS MASS SPECTRUM.

SYSTEM PRESSURE = 5×10^{-10} T.

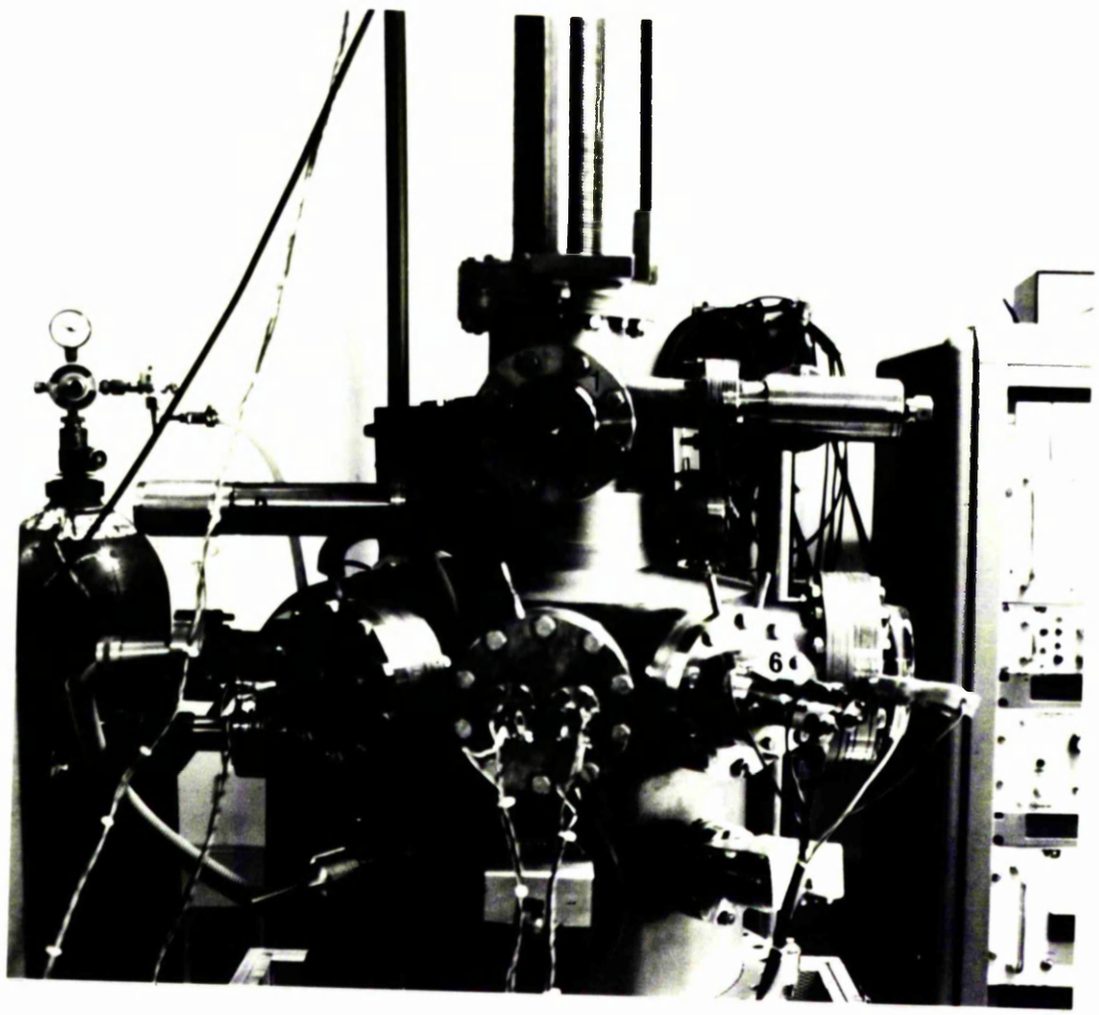

FIG. 3.4 : MBE GROWTH CHAMBER

1. substrate loading port.
2. linear motion drive.

Knudsen ovens —

3. beryllium
4. phosphorus
5. indium
6. zinc

corresponded to 8 to 10 hrs growth time was imposed by the short lifetime of the InP Knudsen oven charge (see Section 3.4.2). The bellows shown in Fig. 3.4 allowed the substrate holder which was located at the end of a linear motion drive rod and X-Y-Z sample manipulator to be lowered from the substrate loading port to the growth plane and also to be positioned at 45^{o} with respect to a Varian argon ion sputter gun. Also shown in Fig. 3.4 are the flanges onto which the molecular beam ovens were horizontally mounted in the growth chamber.

3.3 Knudsen Oven Design

Molecular beam sources for use in MBE systems should be non-reactive, have low gas evolution at their operating temperatures and have rapid thermal response with low radiant power loss. Ideally the sources should be Knudsen ovens as described in Section 2.2.

The design of the Knudsen ovens used in this work is illustrated schematically in Fig. 3.5. Materials with low outgassing rates were used exclusively in the construction of the ovens which consisted of a pyrolytic boron nitride cell, 40mm long and 5mm in diameter (L/r = 16), in which the source charge was placed. The BN cell was contained within a necked quartz tube around which a tantalum heating wire was helically wound while tantalum foil, wrapped onto a quartz former was used to thermally insulate the oven and to provide thermal stability. The oven temperature was monitored by means of a chromel-alumel

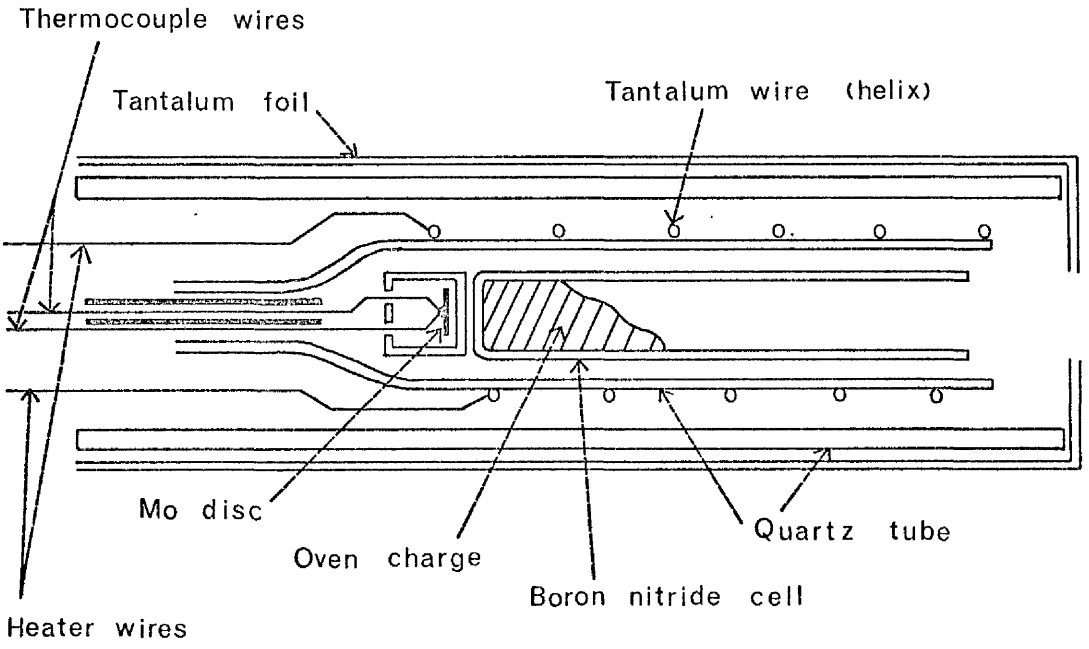

FIG. 3.5 : Schematic of Knudsen oven.

thermocouple spot welded to a molybdenum disc and placed in contact with the BN cell. The whole oven assembly was mounted on a 34mm dia. 4 - way electrical feedthrough flange and surrounded in the vacuum system by a liquid nitrogen-cooled stainless steel shroud as shown in Fig. 3.6. Oven temperatures were stabilised to a level of ± 1°C at 950°C using CRL (model 405) three term temperature controllers; the power consumption of the ovens at 950°C being ∿ 50W.

3.4 Source Material Considerations

The source of predominately P_2 molecules used throughout this work was pre-pulled polycrystalline InP obtained in platelet form from MCP Ltd. Since data relating to the electrical characteristics of the material was not available, its purity was assessed using the photoluminescence technique. Fig. 3.7 shows a typical 77K photoluminescence spectrum obtained from the InP source material using the apparatus illustrated in Fig. 3.8. The half-width of the main luminescence peak at 1.40 eV of ∿ 13meV indicates a free carrier level, $N_D - N_A$, in the material of ∿ 3×10^{16} cm^{-3} (3.3) while a degree of compensation is suggested by the presence of the smaller luminescence peak at 1.37 eV. Both Zn and Si impurities have been assigned to a 1.37eV luminescence level observed in InP material (3.4). Elemental phosphorus is available which is purer (99.9999% pure) than the InP source material used here; however, as discussed in Chapter 2 the growth

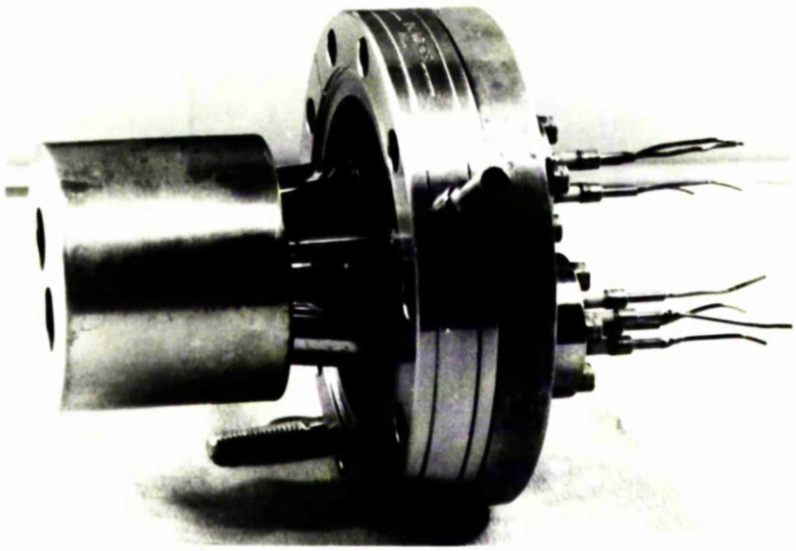

(a)

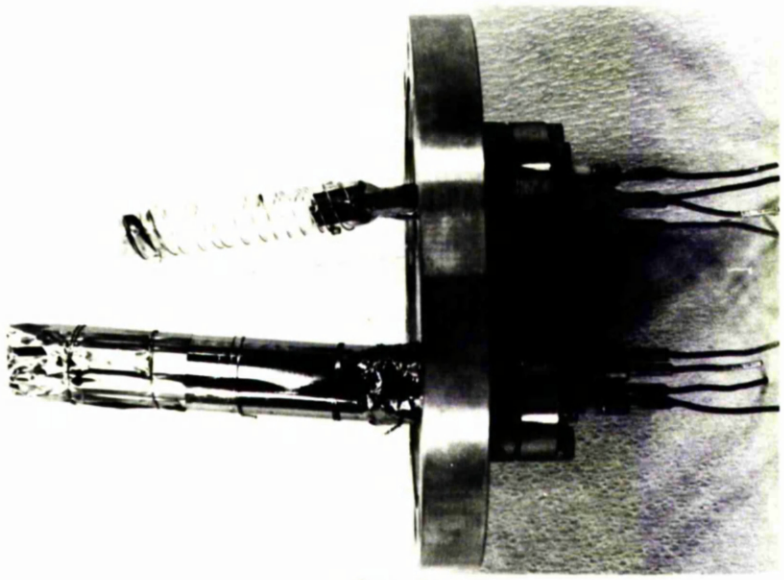

(b)

FIG. 3.6 : KNUDSEN OVEN ARRANGEMENT.

(a) WITH IN_2 - COOLED SHROUD.

(b) MINUS SHROUD AND HEAT SHIELD.

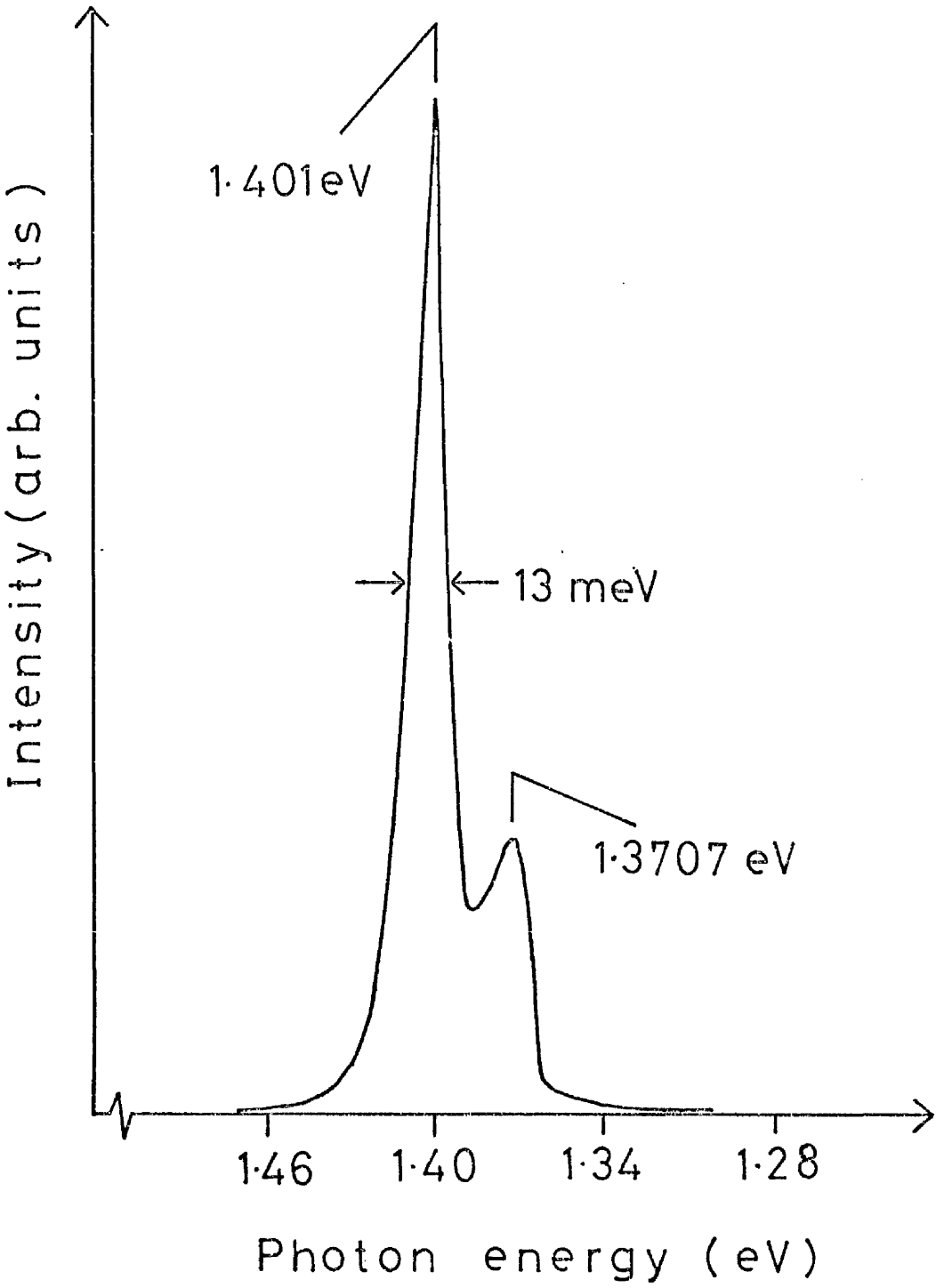

FIG. 3.7 : 77 K photoluminescence spectrum from InP source material.

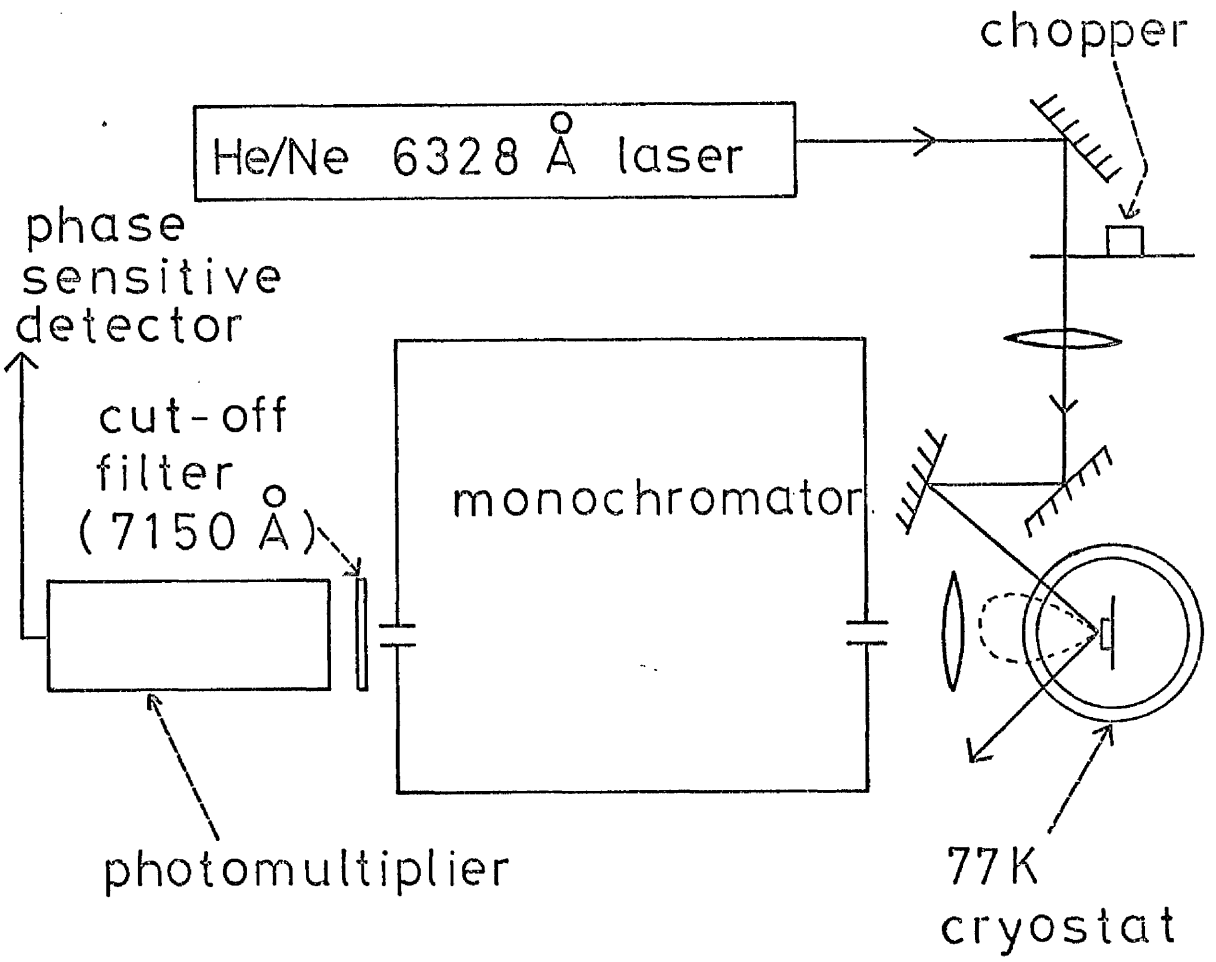

FIG. 3.8 : Schematic of photolumines-
ence set-up.

kinetics are substantially different, implying different optimum growth conditions, using group V tetramers molecules as opposed to group V dimer molecules.

99.9999% pure indium supplied by Johnson Matthey Ltd., was used exclusively as the source of elemental In.

3.4.1 Indium Oven Effusion Species

The V.G. Q8 quadrupole mass spectrometer mounted in the MBE growth chamber as shown in Fig. 3.2, ie in direct line-of-sight with the In and InP ovens, was used to monitor the species effusing from these ovens at their operating temperatures, typically 850^{o}C and 650^{o}C, respectively.

Fig. 3.9(a) records the mass spectrum obtained with the shutter, which operated on both the In and InP ovens simultaneously, closed and with the In and InP ovens at 850^{o}C and 20^{o}C, respectively. Under these conditions only background gases responsible for a background pressure of $\sim 10^{-9}$ Torr were detected. With the shutter open the only additions to the spectrum were the presence of In^{+} isotopes at 115 amu and 113 amu (the accepted natural abundancies of these isotopes are 95.86% In^{115} and 4.16% In^{113}) and In^{2+} at 57 amu; the mass spectrum recorded with the shutter open is shown in Fig. 3.9 (b). Thus, it can be concluded that the shutter was effective in completely blocking the In molecular beam and therefore that the beam was well collimated.

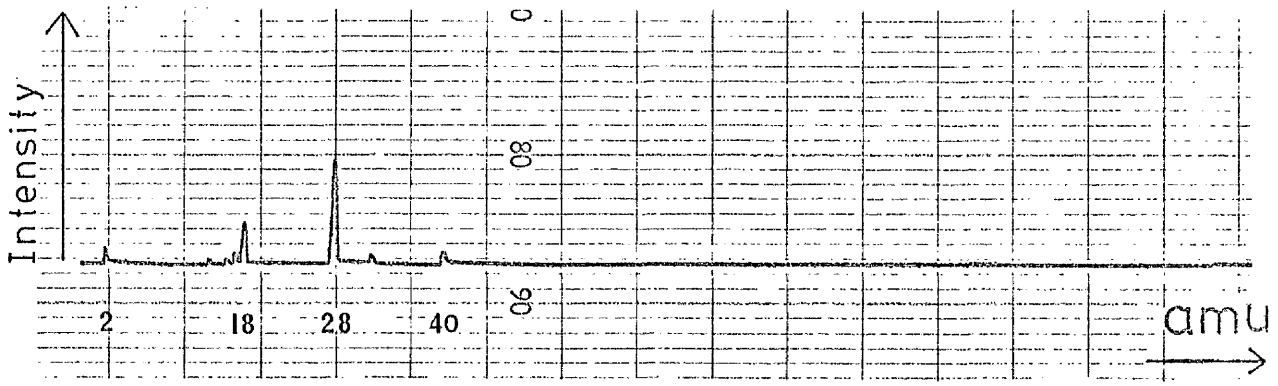

(a)

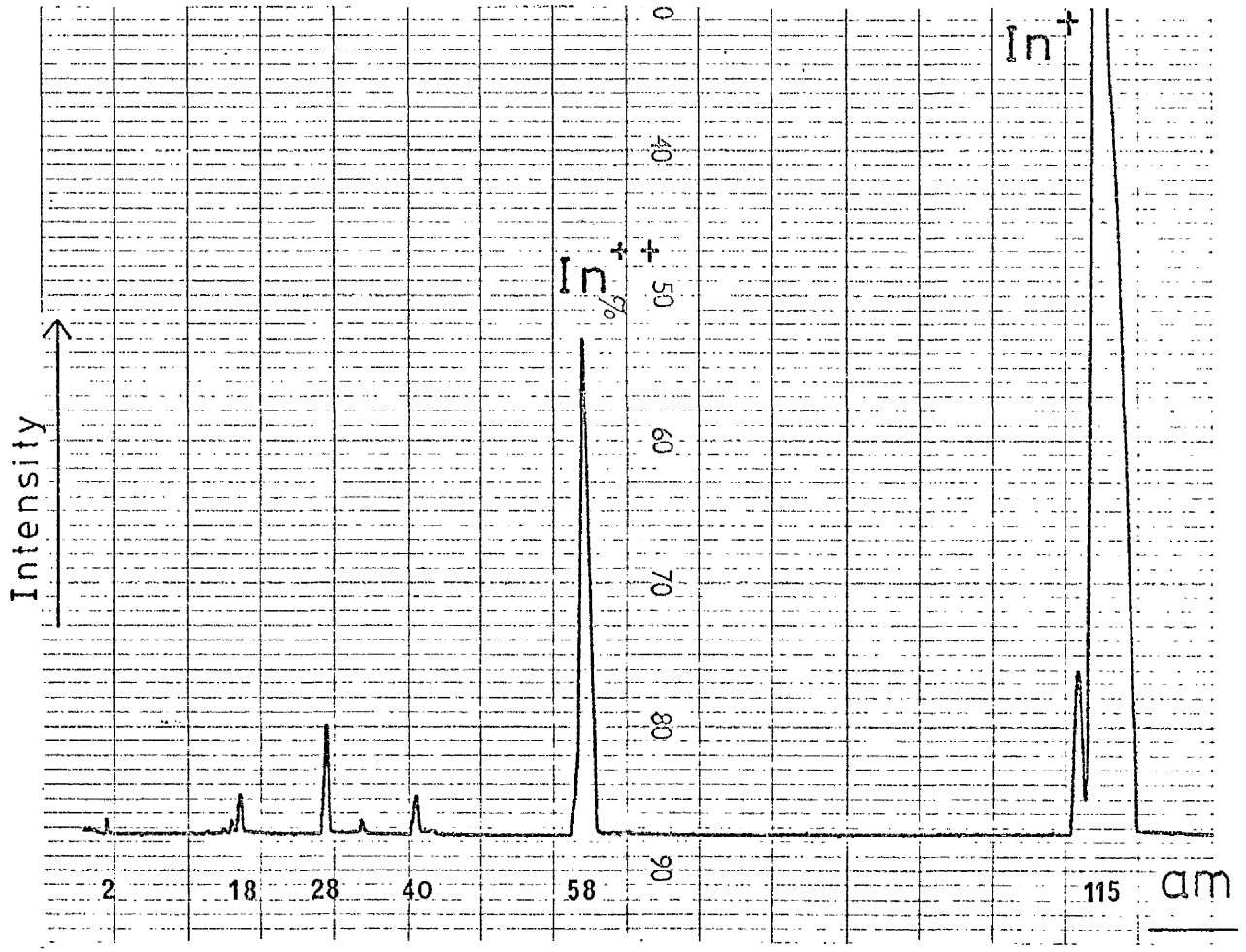

(b)

FIG. 3.9 : MASS SPECTRA WITH INDIUM OVEN AT 850°C.

(a) In oven shutter closed.

(b) Shutter open.

3.4.2 InP Oven Effusion Species

The mass spectrum recorded with the InP and In ovens at 650°C and 20°C, respectively, and with the shutter closed is shown in Fig. 3.10 (a); the cracking pattern of phosphorus is indicated with peaks at 31 amu (P_1^+ and P_2^{2+}), 62 amu (P_2^+ and P_4^{2+}), 93 amu (P_3^+) and 124 amu (P_4^+). As shown in Fig. 3.10 (b) the intensity of each of the peaks detailed above increased by a factor of ∿2 with the shutter in the open position. This corresponded to an increase in the partial pressure of phosphorus in the chamber from 1.2×10^{-8} Torr to 2×10^{-8} Torr. Hence, it can be concluded that the volatile, high vapour pressure phosphorus was not evaporated as a collimated beam but rather heating of the InP created an overpressure of phosphorus in the vacuum chamber. It should be noted here that P_2 and P_4 (90% P_2, 10% P_4) molecules only are evaporated from an InP Knudsen oven at 650°C (together with an extremely small In flux) as shown by Farrow [2.1] from modulated beam mass-spectrometry experiments and thus the relatively large P_4 peak recorded in Figs. 3.10 (a) and 3.10 (b) is attributed to $P_2 + P_2$ association on surfaces in the mass spectrometer ion source region; the P_1^+ and P_3^+ signals are attributed to dissociative ionization of P_2 and P_4 molecules, respectively.

During epitaxial layer growth a constant phosphorus flux level was maintained by monitoring the peak height

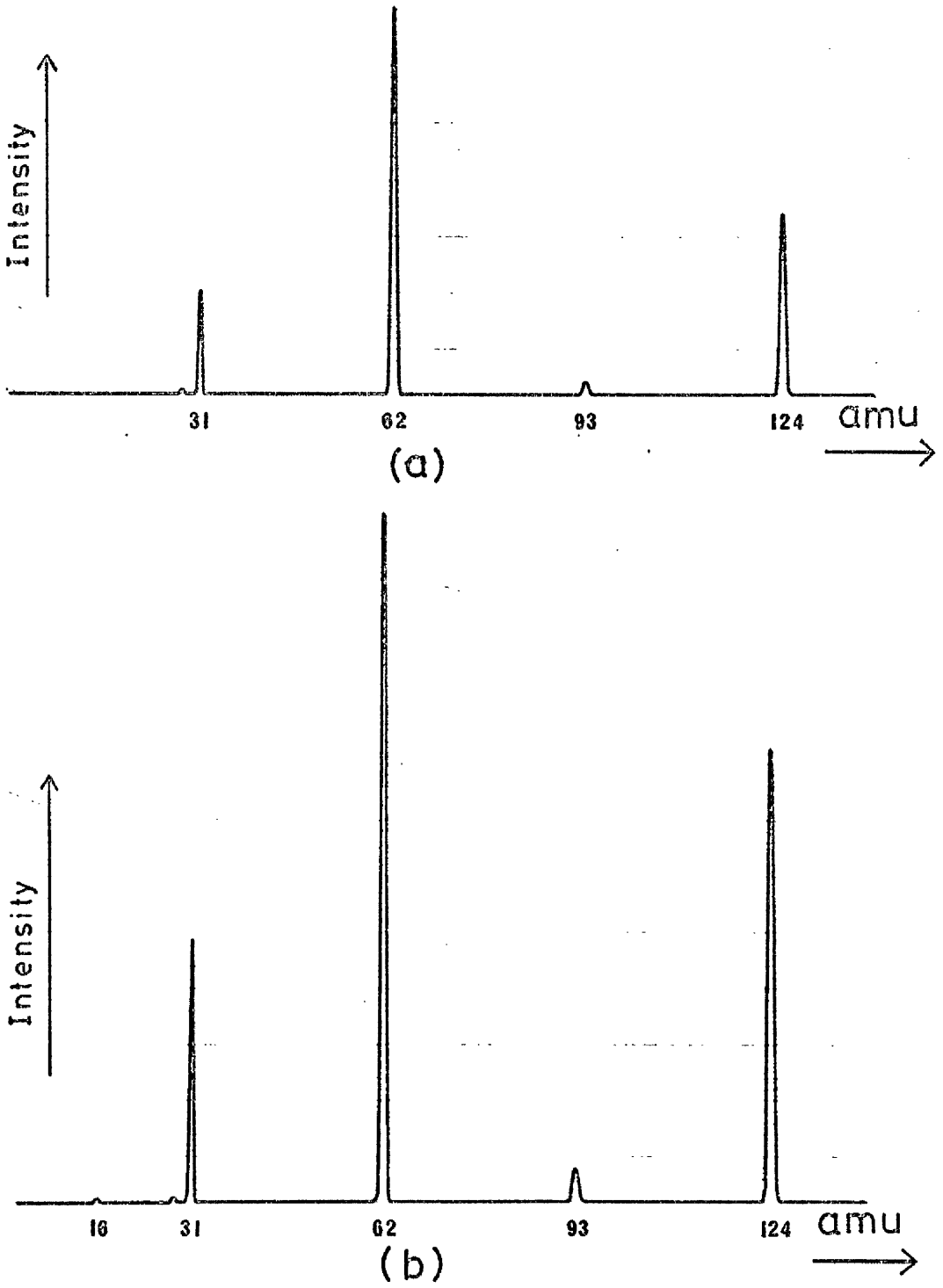

FIG.3.10: MASS SPECTRA WITH InP OVEN AT 650°C.

(a) Shutter closed (b) Shutter open

of the 62 amu ($P_2^+ + P_4^{2+}$) peak. As the InP source became depleted of phosphorus it was found necessary to increase the cell temperature by up to $\sim 20^oC$ in order to maintain the peak height constant. A phosphorus depleted InP charge is shown in Fig. 3.11 which illustrates the accumulation of pure In towards the front end of the cell.

3.5 Substrate Preparation: Ex-Vacuo

Saw-cut 0.5 mm thick (100) InP substrate material grown by the liquid encapsulated Czochralski (LEC) method was supplied by M.C.P. Ltd. Fe-doped semi-insulating substrates were used to allow electrical characterisation of epitaxial layers while Zn-doped p^+-type substrates (2×10^{18} cm^{-3}) were employed in order to facilitate deep level transient spectroscopy measurements (see chapter 6) on p^+-n InP junctions grown by MBE. Substrates having the dimensions 1cm x 0.5cm were attached to a glass block using dental wax and lapped on a polishing pad (hyprocel pellon) which was soaked in a 0.5% Br_2 - methanol solution. After a polishing time of 40 - 60 mins. substrate surfaces were mirror-like and scratch-free with a slight "orange-peel" appearance being observed by Nomarski phase contrast microscopy. Removal of a substrate from the glass block was effected by placing the block in warm trichloroethylene, thus dissolving the dental wax. Substrates were then rinsed in Analar methanol and blow-dried in a pure nitrogen stream prior to loading in the vacuum system. A Nomarski

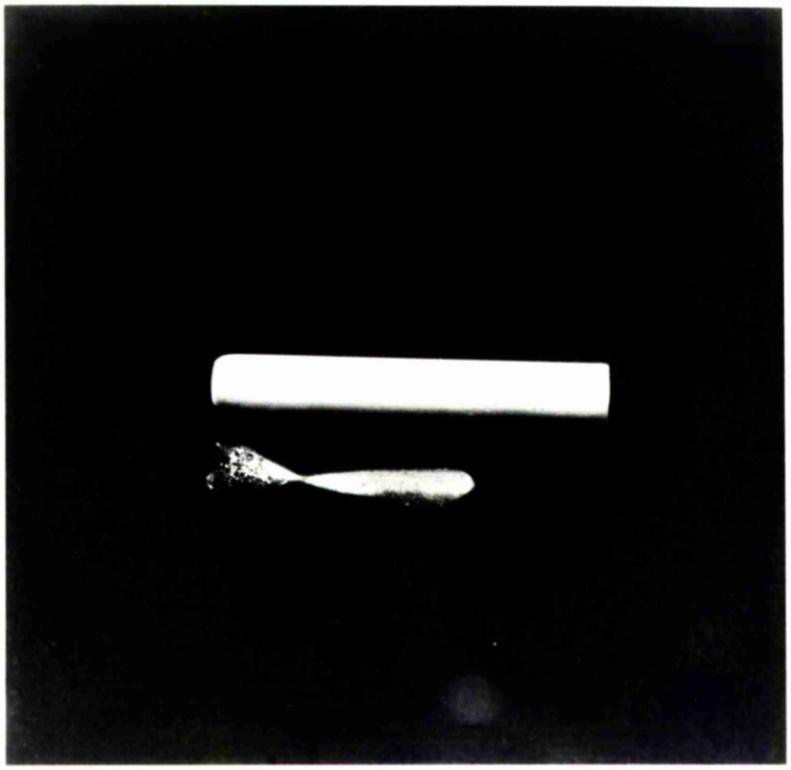

FIG. 3.11 : PHOSPHORUS - DEPLETED InP CHARGE WITH BN CRUCIBLE.

phase contrast micrograph of the surface of an InP substrate after polishing is shown in Fig. 3.12.

Although the polishing technique outlined above is successful in producing smooth and essentially featureless surfaces, substantial amounts of carbon and oxygen remain on the surfaces.[3.6] Furthermore, carbon contamination in excess of 0.2 monolayers on GaAs substrate surfaces has been shown to result in deposited GaAs layers exhibiting twins and surface facetting [1.1]. Therefore it is essential to remove traces of contaminants such as C and O from substrate surfaces prior to film deposition by some in-vacuo substrate cleaning technique.

3.6 Substrate Preparation: In-Vacuo

Substrate surfaces were atomically cleaned in-vacuo by a series of three 1 hour argon-ion sputtering and annealing cycles. 500eV argon-ions were impinged at an angle of 45^{o} with respect to the substrate normal with an ion current density at the substrate of $\sim$ 1μA cm^{-2}; annealing temperatures were typically 280^{o}C. Farrow [3.6] has shown that this technique is effective in reducing the concentrations of surface impurities, principally C and O, to below the detection limit of Auger electron spectroscopy, namely 0.1% monolayer, although Dowsett et al [3.7] have detected surface impurities of 600 ppm using the secondary ion mass spectrometry technique (SIMS).

X 50

FIG. 3.12 : Nomarski phase contrast micrograph of surface of a polished substrate.

In an attempt to observe the sputtered species produced during argon-ion bombardment the quadrupole mass spectrometer was mounted in the vacuum chamber as shown in Fig. 3.13. Zero ionising power was supplied to the mass spectrometer ionisation chamber so that the instrument could only resolve ions which were launched directly into the quadrupole from an external source. Fig. 3.14 (a) shows the mass spectrum recorded with the substrate removed from the sputtering position; incident Ar^+ and Ar^{2+} ions were detected. With the substrate lowered to the sputtering position the mass spectrum recorded is as shown in Fig. 3.14 (b) which illustrates the detection of a smaller proportion of incident Ar^+ ions together with sputtered In^+ ions, ie secondary In^+ ions. Secondary P ions were not detected possibly because sputtered P ions are negatively charged [3.8] and as such are not observable using the quadrupole instrument in its normal operating mode. Sputtered impurity atoms were not observed since their concentrations were well below the detection limit of the mass spectrometer again in its normal operation mode. The basic principles of secondary ion mass spectrometry have been demonstrated here although modifications would have to be made to the quadrupole instrument in order to facilitate proper SIMS analysis.

A sputter-rate of $\sim 250 \text{Å}\ hr^{-1}$ for InP material was obtained from Talystep measurements on substrates which were half-covered by Ta foil prior to being sputter-cleaned. A total of $\sim 375 \text{Å}$ of substrate material therefore

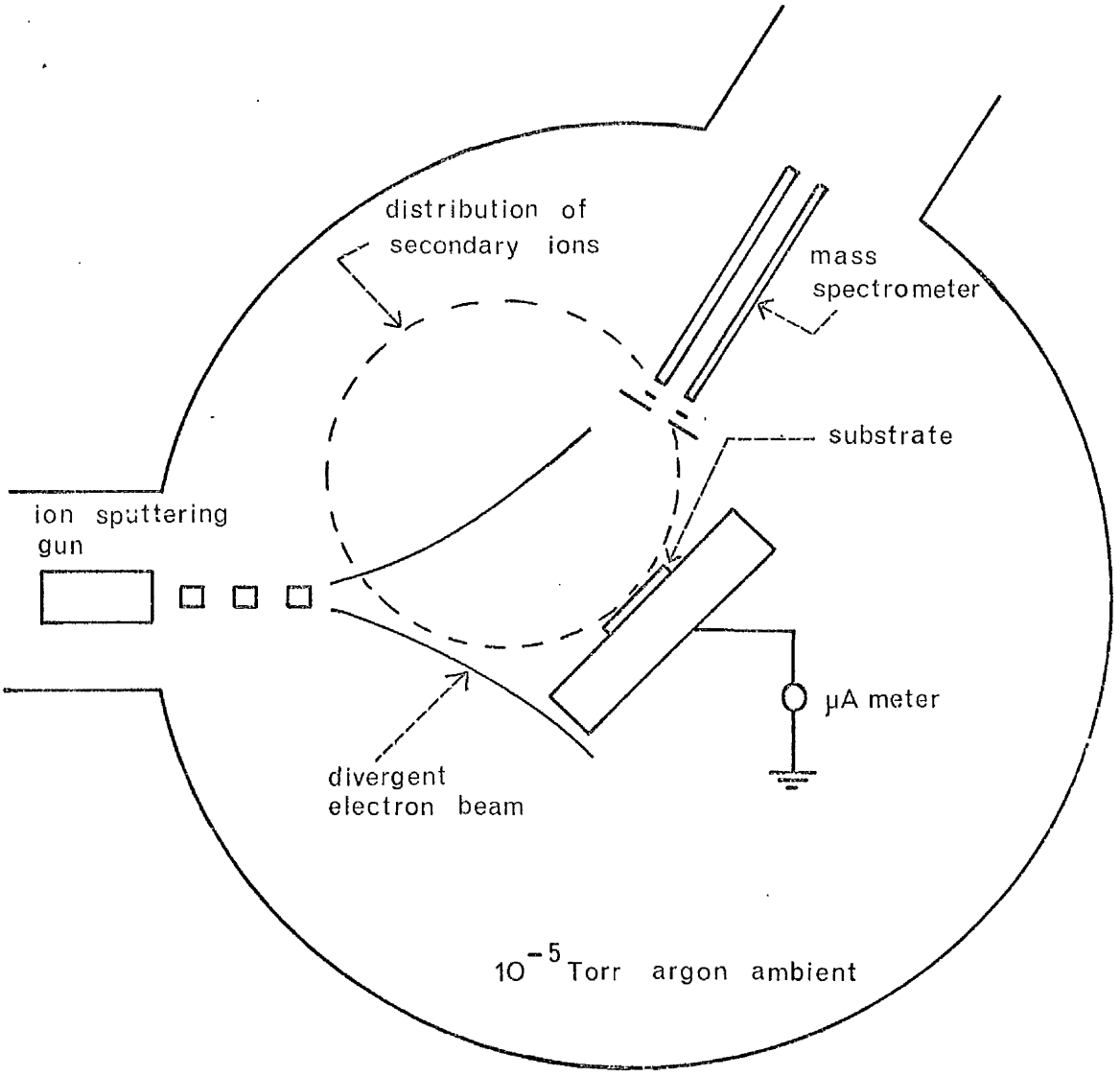

FIG. 3.13 : Schematic of SIMS set-up.

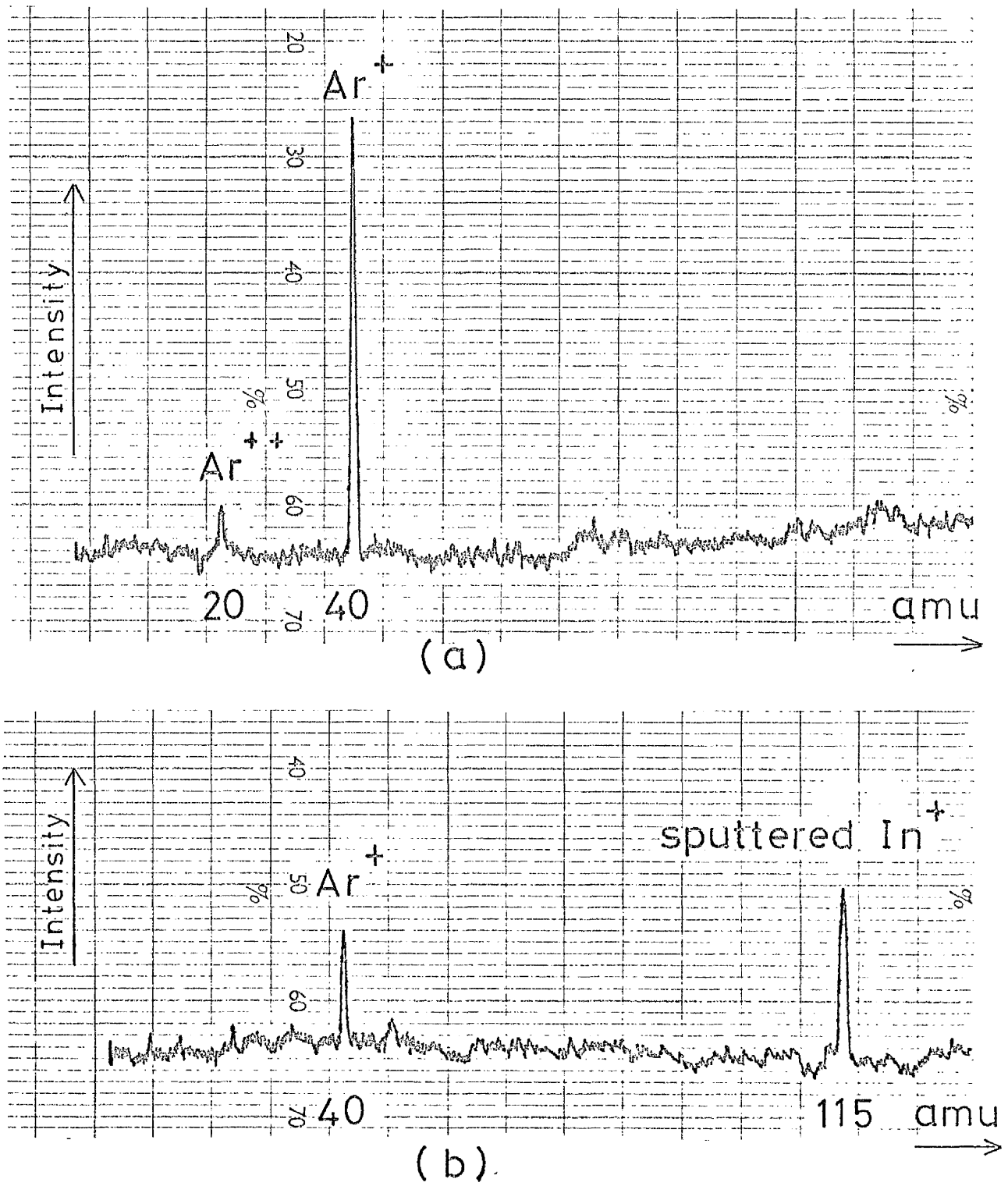

FIG. 3.14 : MASS SPECTRA RECORDED DURING SPUTTERING PROCESS.

(a) Incident 500 eV Ar ions.

(b) Sputtered species.

was removed during the in-vacuo substrate cleaning process outlined above.

3.7 Growth and Characterisation of InP Films

Prior to the in-vacuo substrate cleaning process the In and InP ovens were outgassed for 1 hr at 20°C above their normal operating temperatures, namely at 870°C and 670°C, respectively, after the system had been evacuated to a background pressure of $\sim 5 \times 10^{-10}$ Torr. Following the substrate cleaning stage the In and InP ovens were run up to 850°C and 650°C, respectively, with the shutter in the closed position and maintained at these temperatures for $\sim$ 15 mins. while the substrate temperature was stabilised at 360°C in the phosphorus background (1.2×10^{-8} Torr partial pressure). Film growth was initiated by opening the shutter which allowed the In flux to arrive at the substrate.

3.7.1 Film Thickness Measurement

Substrates were held in place on the molybdenum heating block by means of a 250μm dia. Ta wire which also effectively 'masked' the part of the substrate with which it was in direct contact. This masking effect allowed film thicknesses to be determined using both Tolansky interference microscopy [3.9] and Talystep measurement. Fig. 3.15 (a) shows a Tolansky interference micrograph of a film (growth time = 1 hr) indicating the presence of two steps corresponding to two regions of epitaxial film separated by the masked substrate region. The curved

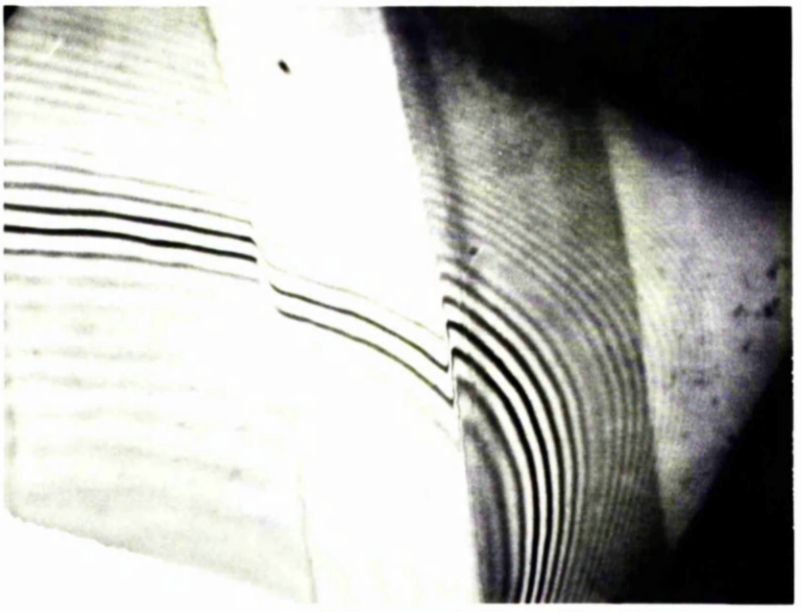

(a)

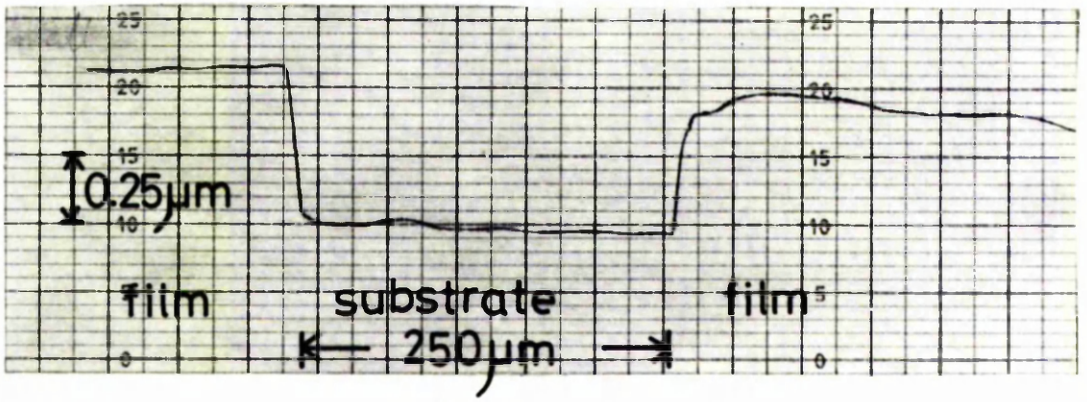

(b)

FIG. 3.15 : FILM THICKNESS MEASUREMENT.

(a) TOLANSKY INTERFERENCE MICRO-GRAPH.

(b) TALYSTEP TRACE.

fringes on the right hand side of the micrograph are due to an edge-rounding effect caused by the chemical polishing process which was reproduced by the epitaxial layer. A Talystep trace which profiles the same film/substrate region is illustrated in Fig. 3.15 (b). Both techniques yielded a film thickness of ∿0.5μm. A plot of film thickness against growth time is shown in Fig. 3.16, indicating that the film thickness increased with growth time in a linear fashion, the experimental points lying on a straight line of slope 0.5 μm hr^{-1}. The theoretical In oven temperature required for a film growth rate of 0.5 μm hr^{-1} is ∿ 870°C as calculated using equations 2.9 and 2.10 which represents a 20°C discrepancy between the theoretical In oven temperature and the monitored temperature. A similar temperature discrepancy was found at different growth rates ranging from 0.3 μm hr^{-1} to 1 μm hr^{-1} and therefore it is concluded that the actual temperature inside the BN crucible was ∿ 20°C higher than the oven temperature as monitored by the thermocouple.

An In oven temperature of 850°C was maintained throughout this work which as deduced experimentally corresponded to a film growth rate of 0.5 μm hr^{-1} and therefore an In flux level at the substrate of ∿ 3×10^{14} cm^{-2} s^{-1}. The phosphorus flux level was not directly determined; however, using the data of Farrow [3.5] for the equilibrium vapour pressure of P_2 over InP and the Knudsen equation (equation 2.9) a theoretical flux level of ∿ 2×10^{15} cm^{-2} s^{-1} for P_2 molecules is obtained

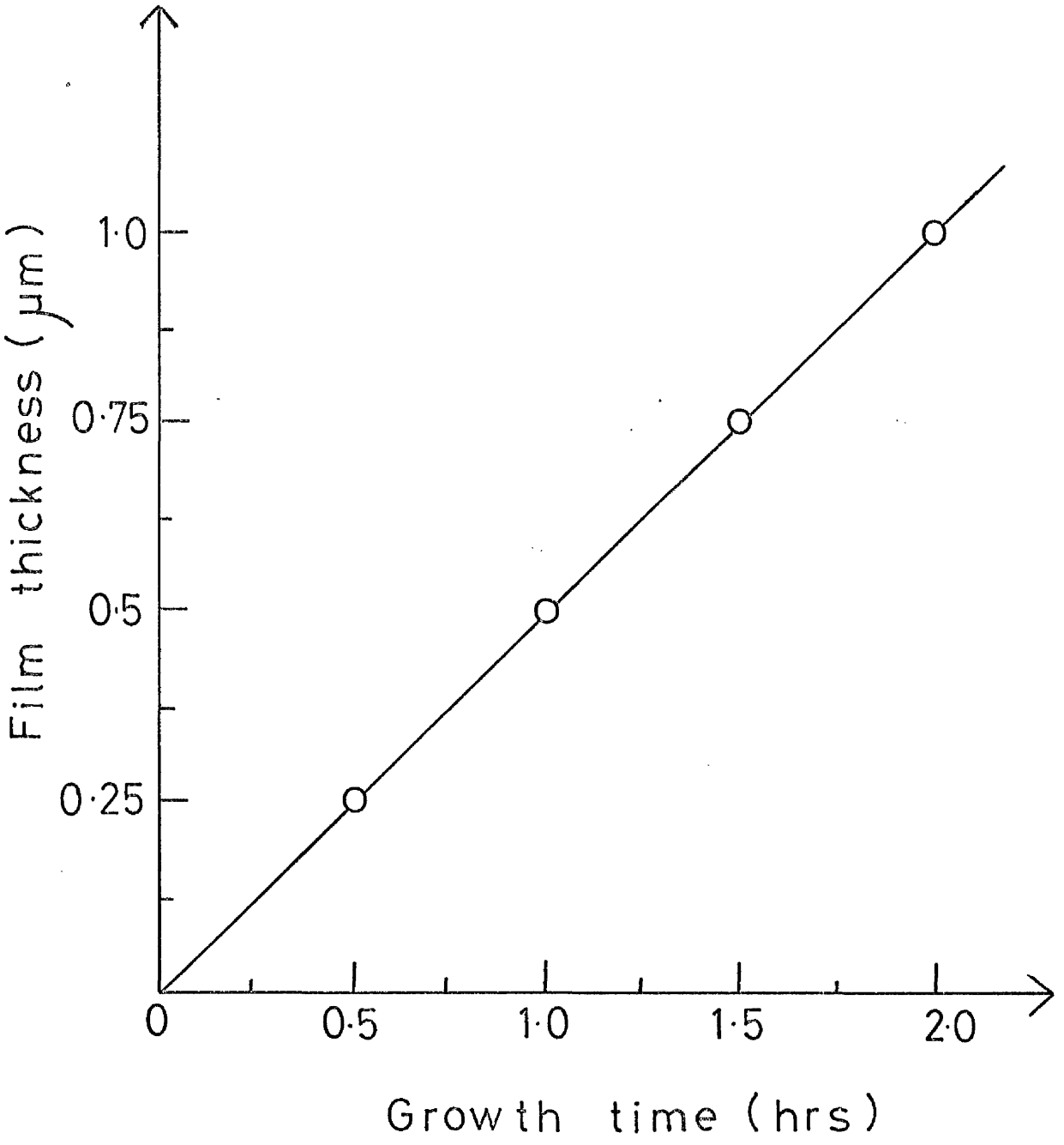

FIG. 3.16 : Film thickness measured by Talystep (±10 Å accuracy) plotted against growth time.

In oven temp = 850°C.

for an InP oven temperature of 650°C. Hence, the ratio J_{P2}/J_{In} used throughout this work was >5.

3.7.2 Visual and Microscopic Assessment of Layers

Films deposited under the conditions outlined above at a typical substrate temperature of 360°C were mirror-like and featureless to the naked-eye while the polished substrate surface "orange-peel" appearance was reproduced on the film surfaces as observed using Nomarski phase contrast microscopy. Fig. 3.17 shows a scanning electron micrograph of the surface of a 1μm thick unintentionally doped InP film at x 10,000 magnification which indicates that film surfaces were smooth and essentially featureless on a microscopic level; the particle to the top right hand corner of the micrograph was located to aid focussing.

3.7.3 Crystallographic Assessment of Layers

The crystallographic quality of MBE grown InP layers was assessed by both X-ray texture camera (see Appendix A.1) and electron channelling [3.10] techniques. Figs. 3.18 and 3.19 show the texture camera and electron channelling patterns, respectively, obtained from a 1μm thick unintentionally doped film grown onto an argon-ion sputtered and annealed substrate at a growth temperature of 360°C. The X-ray diffraction pattern shown in Fig. 3.18 which was recorded using CrKα radiation is indicative of twin-free (100) orientated single crystal material while an electron channelling pattern such as that

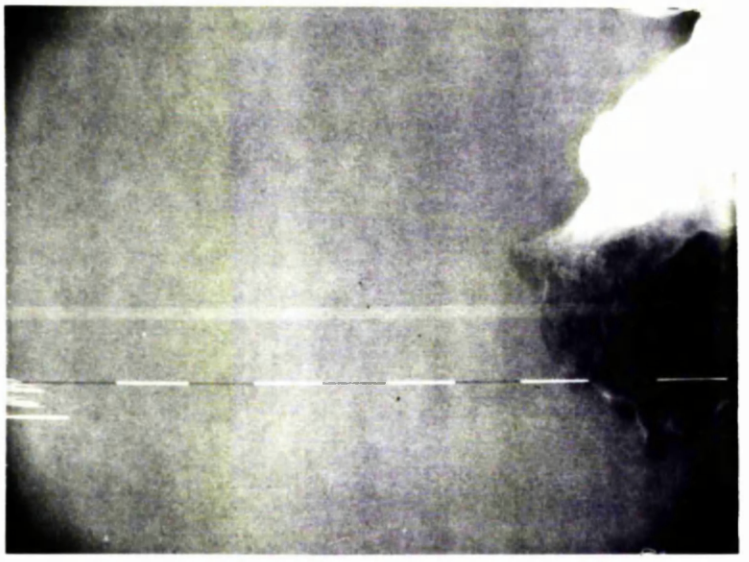

1 μm
markers

X 10 K MAG.

FIG. 3.17 : SEM Micrograph of surface of unintentionally doped InP film.

T_s = 360 °C.

Film thickness = 1 μm.

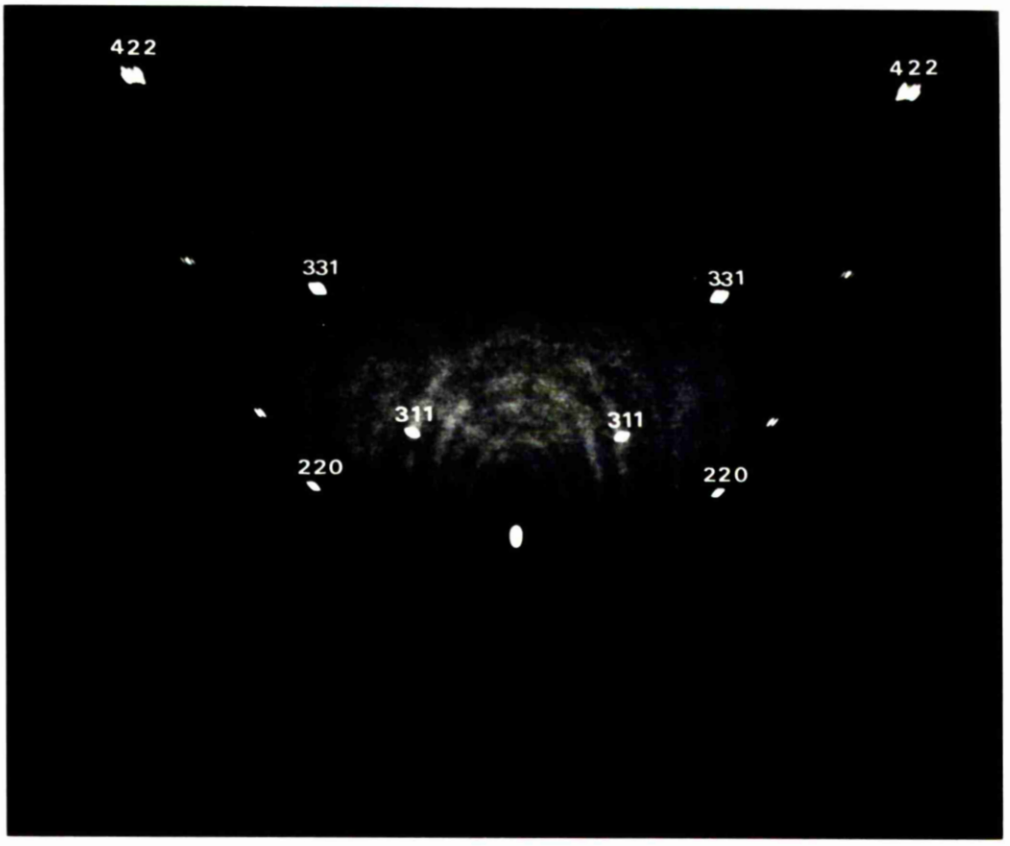

FIG. 3.18 : Texture camera pattern from an unintentionally doped InP film.

illustrated in Fig. 3.19 is only obtained from films having a high degree of surface perfection [3.10]. The electron channelling pattern was observed with a scanning electron microscope operating in the specimen current mode. The rectangular shaped dark area shown in the channelling micrograph is the image of an Al contact pad which was deposited onto the film as part of a Hall-effect contact arrangement (see section 3.7.4). In contrast, Fig. 3.20 shows the X-ray texture diffraction pattern obtained from a film grown onto a substrate which was not cleaned in-vacuo by the argon-ion sputtering and annealing process. Additional reflections from (111) planes can be seen in the pattern of Fig. 3.20, indicating the presence of twins although the film was essentially epitaxial.

3.7.4 Electrical Characterisation of Layers

Hall-effect measurements (see Appendix A.2) and plasma reflectivity measurements [3.11] were used to characterise the electrical properties of <1μm thick unintentionally doped films and the results obtained using both these techniques are detailed below.

(a) Hall-effect measurements

Samples were prepared for Hall-effect measurements as follows: Al contacts were evaporated onto epi-layer surfaces through holes in a metal mask in order to form the 5 pad contact pattern illustrated in Fig. A.2.1; the Al contacts were shown to be 'ohmic' at both 300K and 77K.

Amendment to section 3.7.3

The Electron Channelling Technique

A pseudo Kikuchi effect discovered by Coates [3.10] using a Cambridge Stereoscan SEM permits a rapid qualitative assessment of bulk single crystal samples. The effect, in the form of lines and bands of contrast, is directly observed in both the emissive backscattered and specimen-current modes of operation at beam accelerating voltages from 20kV down to 2kV. A contrast pattern such as that illustrated in Fig. 3.19 is generated as the angle of the incident electron beam changes with respect to the Bragg planes in the specimen. Enhanced electron absorption is seen in the specimen-current mode of operation when the incident beam is parallel to a low-index plane. With this technique, as crystallographic perfection decreases, the contrast decreases and the line widths increase, so that higher order (narrower) lines progressively disappear. In a scale from 0 to 10 devised by Coates to assess the quality of specimens relative to a high quality single crystal having a rating of 10, the channelling pattern shown in Fig. 3.19 has been given a rating of 7 [3.19].

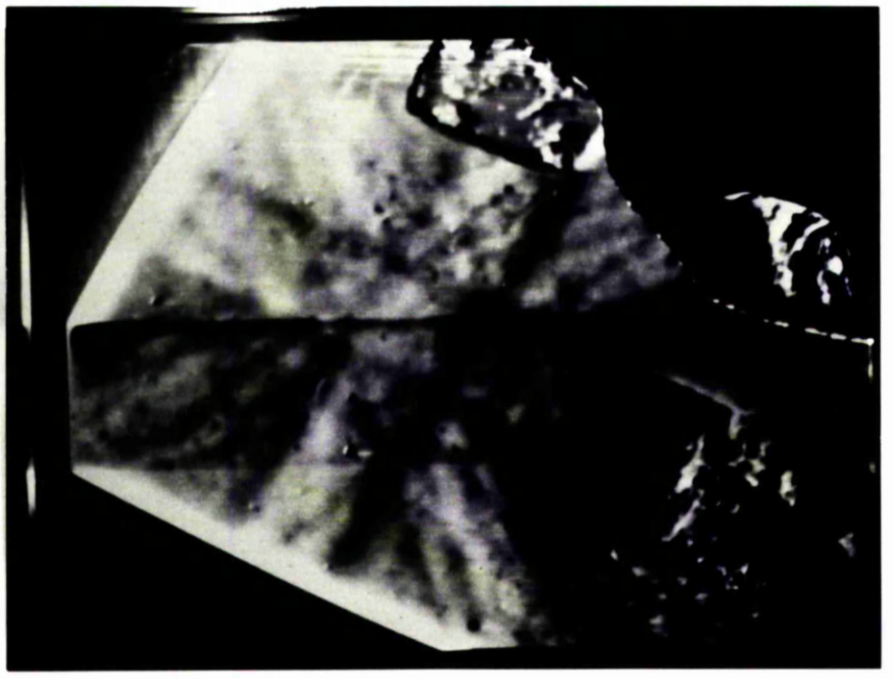

FIG. 3.19 : Electron channelling micrograph from an unintentionally doped InP film.

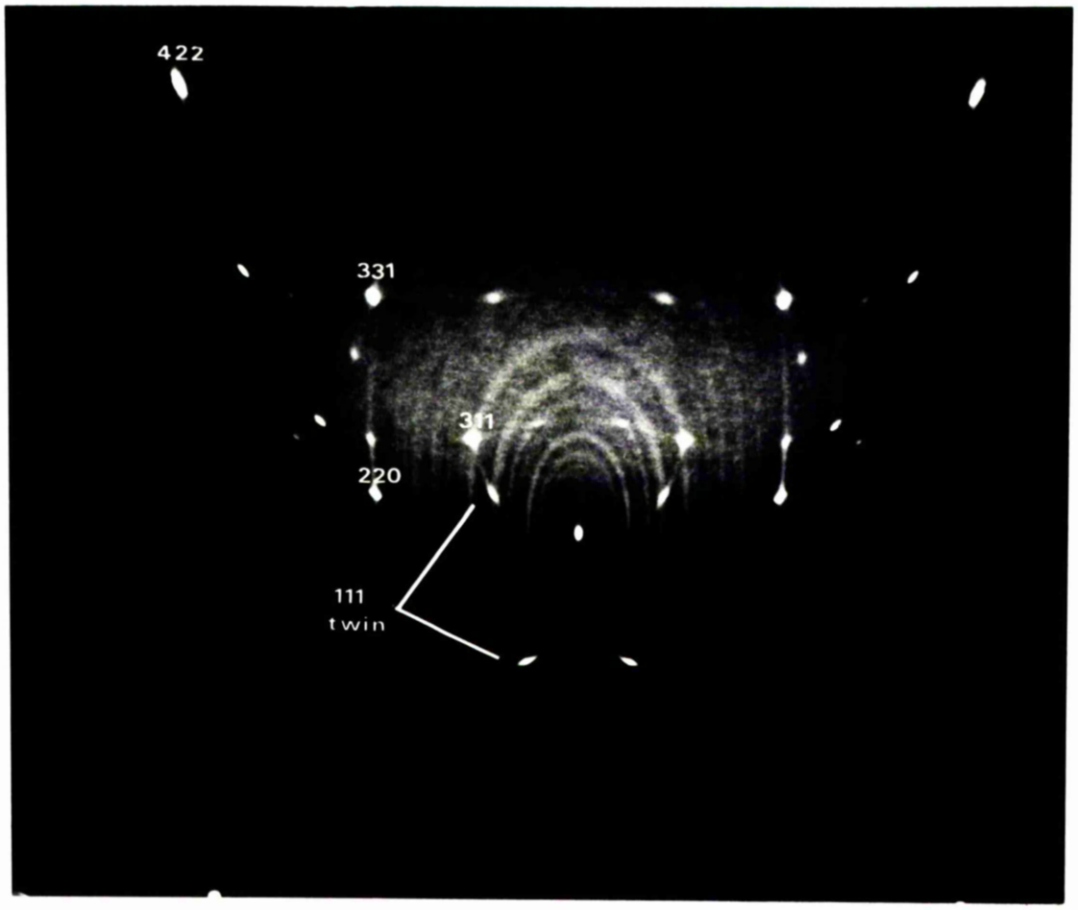

FIG. 3.20 : Texture camera pattern from an InP film grown on an as-loaded substrate.

Samples were then mounted onto a brass cryostat as shown in Fig. 3.21, electrical contact being made to the Al pads by means of gold wires secured with silver dag.

Unintentionally doped InP films were n-type, the free-carrier concentrations and electron mobilities in the films being found to be a strong function of run number following an initial bakeout of the vacuum system. Fig. 3.22 shows a plot of free-carrier concentration and mobility versus growth run number obtained by R.T. Hall-effect measurements. As can be seen from the figure the free-carrier concentration decreased from 10^{18} cm^{-3} (run no. 1) to 2.9×10^{16} cm^{-3} (run no. 5) while electron mobilities increased from 400 $cm^2V^{-1}s^{-1}$ (run no. 1) to $\sim$1,000 $cm^2V^{-1}s^{-1}$ (run no. 5). Typical results obtained at R.T. and 77K for run no. 4 to 5 films are given below;

$$N_D - N_A = 2.9 \times 10^{16} cm^{-3}, \quad \mu = 1000\ cm^2V^{-1}s^{-1} \qquad \text{R.T.}$$

$$N_D - N_A = 2.2 \times 10^{16} cm^{-3}, \quad \mu = 970\ cm^2V^{-1}s^{-1} \qquad \text{77K}$$

These results indicate a compensation ratio, $(N_D + N_A)/(N_D - N_A)$, greater than 5 at R.T. (3.12).

(b) Plasma reflectivity measurements (3.11)

Plasma reflectivity measurements were made on 1μm thick films which exhibited the lowest unintentional doping levels and highest electron mobilities as measured by the

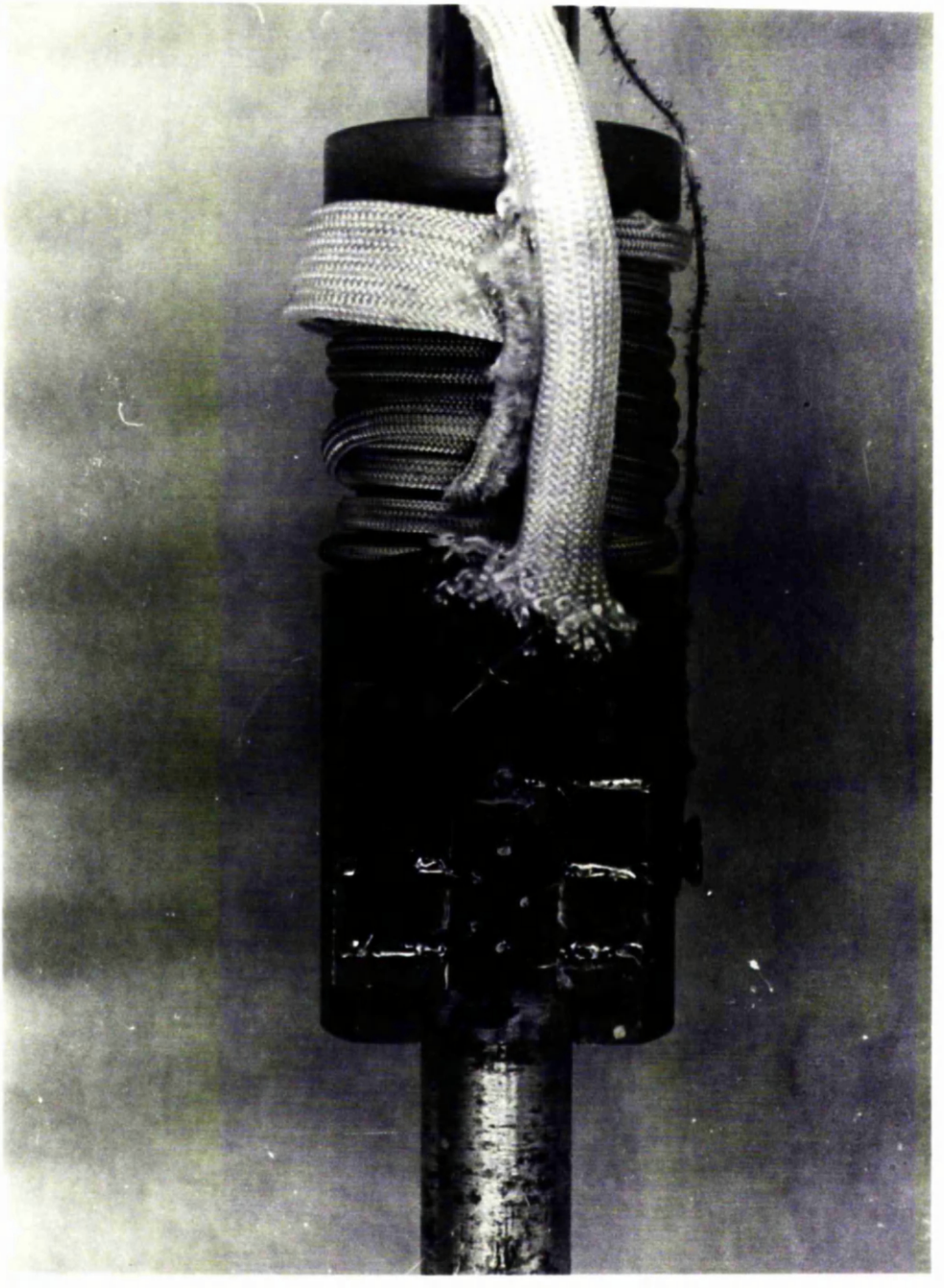

FIG. 3.21 : HALL-EFFECT CRYOSTAT.

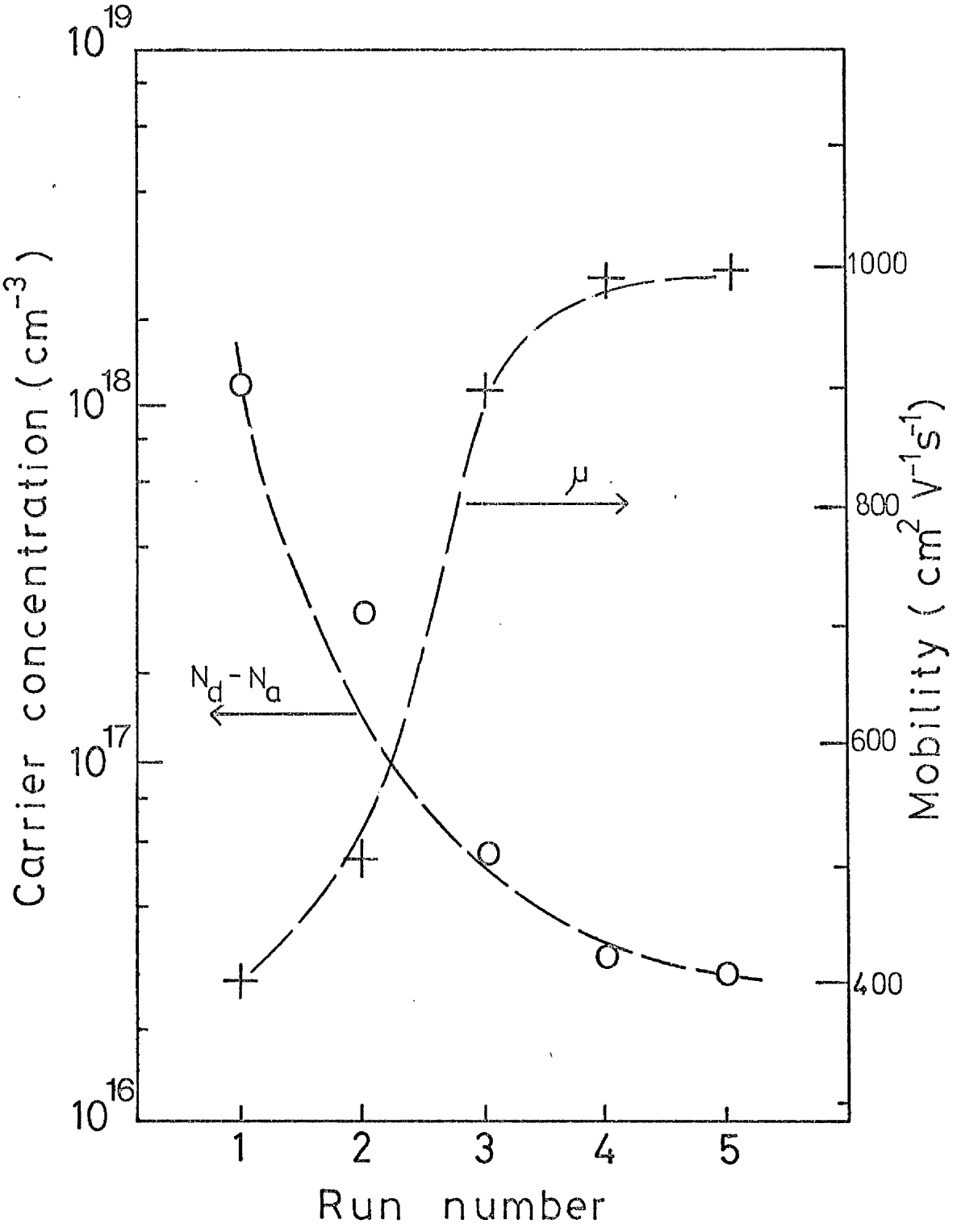

FIG. 3.22 : R.T. Hall-effect data on unintentionally doped InP.

$T_s = 360^{\circ}C$

Hall-effect technique, ie films having $N_D - N_A \simeq 3 \times 10^{16}$ cm^{-3} and $\mu \simeq 1{,}000$ $cm^2V^{-1}s^{-1}$ at R.T. Free-carrier concentrations of $\sim 10^{17}$ cm^{-3} were obtained by plasma reflectivity measurements at R.T. while electron mobilities were in the range 2,500 to 3,000 $cm^2V^{-1}s^{-1}$, indicating a compensation ratio of between 1 and 2 [3.12]. It should be noted here that the penetration depth of the radiation in InP material is only $\sim$ 0.5μm at the resonant frequency in the plasma reflectance technique [3.13] (c.f. a film thickness of 1μm).

3.7.5 Photoluminescence from InP Layers

Unintentionally doped InP films (<1μm thick) grown onto argon-ion sputtered and annealed substrates exhibited zero detectable photoluminescence at both R.T. and 77K although a very weak P.L. signal was observed from films which were cooled to 7K [3.14]; a typical 7K P.L. spectrum is shown in Fig. 3.23, indicating band-to-band recombination at 1.412eV with a peak half-width of 9meV.

3.8 Further Observations Relating to the Argon-Ion Sputter/Anneal-Cleaning Process

The fact that Hall-effect and plasma reflectivity measurements made on epitaxial films provided substantially different results lead to speculation that the substrate/film interface was seriously influencing electrical measurements on epi-layers. In order to verify this hypothesis Hall-effect measurements were made on a

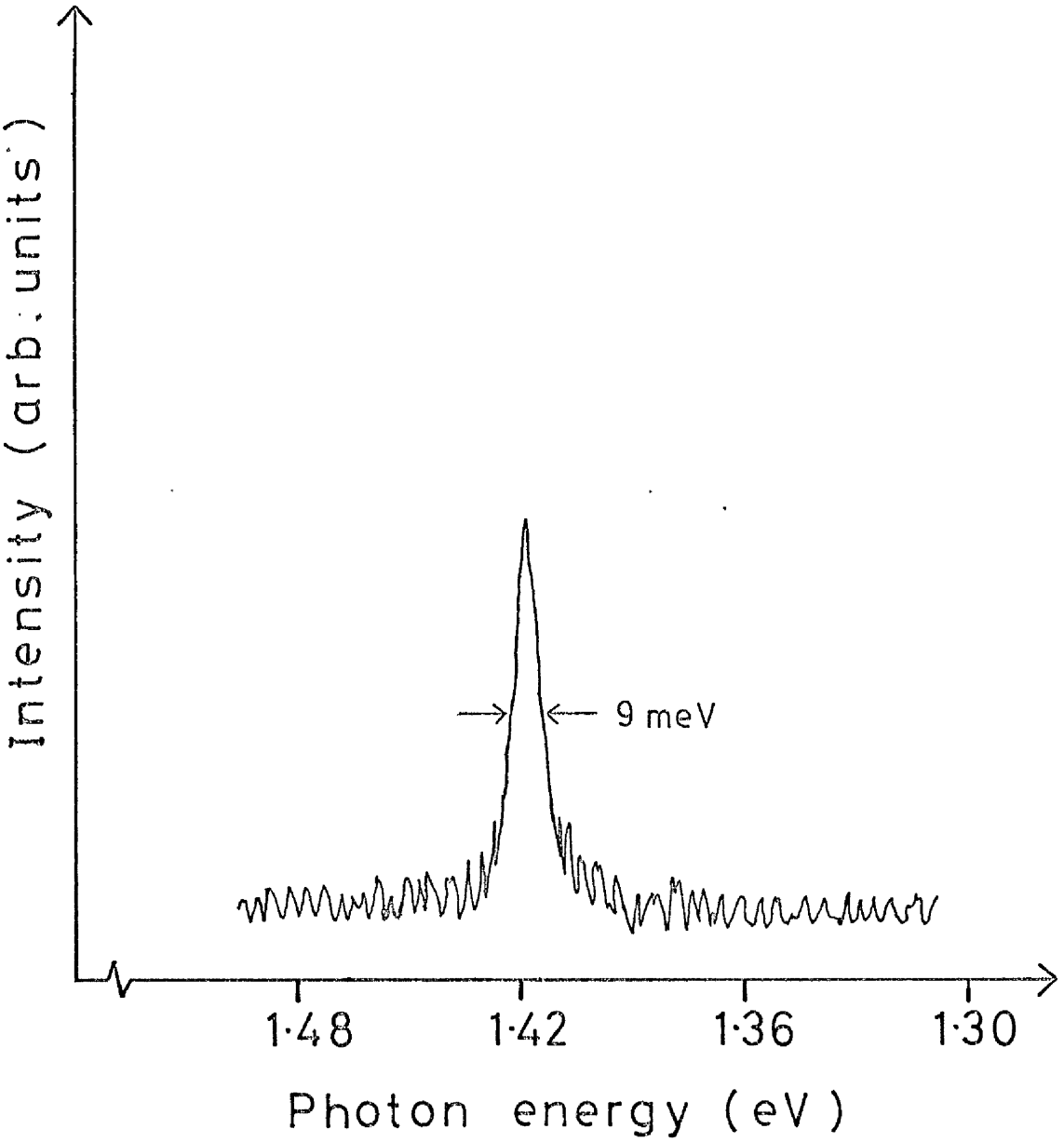

FIG. 3.23 7 K P. L. spectrum from an InP film grown on a sputter-cleaned substrate.

semi-insulating Fe-doped substrate which had been subjected to the argon-ion sputtering and annealing cleaning technique and subsequently removed from the vacuum system without a film being deposited onto it. The first observation made when the contact pattern had been layed down was that the surface of the semi-insulating substrate exhibited conduction. Hall-effect measurements gave the following results;

$$N_D - N_A = 3.9 \times 10^{16} cm^{-3} \qquad \text{R.T.}$$
$$\mu = 786\ cm^2 V^{-1} s^{-1}$$

$$N_D - N_A = 1.2 \times 10^{16} cm^{-3} \qquad 77K$$
$$\mu = 607\ cm^2 V^{-1} s^{-1}$$

assuming the conducting layer to extend $\sim 1000\text{A}^{o}$ below the surface [3.15]. Thus, semi-insulating substrate surfaces would appear to be converted by the argon-ion sputtering and annealing process to n-type. Bachmann et al [3.15] have made similar observations, reporting the measurement of a $\sim 1000\text{A}^{o}$ thick n-type layer with $N_D - N_A \sim 10^{16} cm^{-3}$ on argon-ion sputter/annealed Fe-doped InP substrates.

A second experiment performed to further investigate the effect of the ion-bombardment cleaning technique on substrate surfaces was as follows. An n^+-type substrate (Sn-doped, $10^{18} cm^{-3}$) which was half-covered by Ta foil was argon-ion sputtered and annealed in the usual manner and removed from the vacuum system. The photoluminescence apparatus shown in Fig. 3.8 was used to compare the P.L. yields from the sputtered and unsputtered areas of the

n^+-type substrate. Figs. 3.24 (a) and 3.24(b) illustrate the R.T. photoluminescence spectra obtained from sputtered and unsputtered regions of the substrate, respectively, indicating a 30% reduction in the P.L. intensity as a consequence of the in-vacuo surface treatment. Since argon-ion sputtered and annealed substrate surfaces have been shown to be crystallographically undamaged by RHEED [3.1] it is concluded that the P.L. yield is reduced due to the creation of deep levels at the surface which act as non-radiative recombination centres.

3.9 Discussion of Results

The striking feature of the work described in this chapter is the influence which the substrate/film interface has been found to have on the electrical and optical characterisation of films grown onto argon-ion sputtered and annealed substrates. Substrate surfaces following the in-vacuo cleaning technique have been shown to contain shallow donor and accepter levels as evidenced by the electrical measurements on treated semi-insulating surfaces (section 3.8) and also deep levels as evidenced from the reduced P.L. yield from treated n^+-type substrates (section 3.8). It is postulated that the deep levels are a consequence of vacancies (both In and P) or vacancy-complexes created during the ion-bombardment cycle while impurities may be incorporated from the ambient during the annealing stage resulting in shallow donor and accepter levels although shallow level point defects cannot be ruled out.

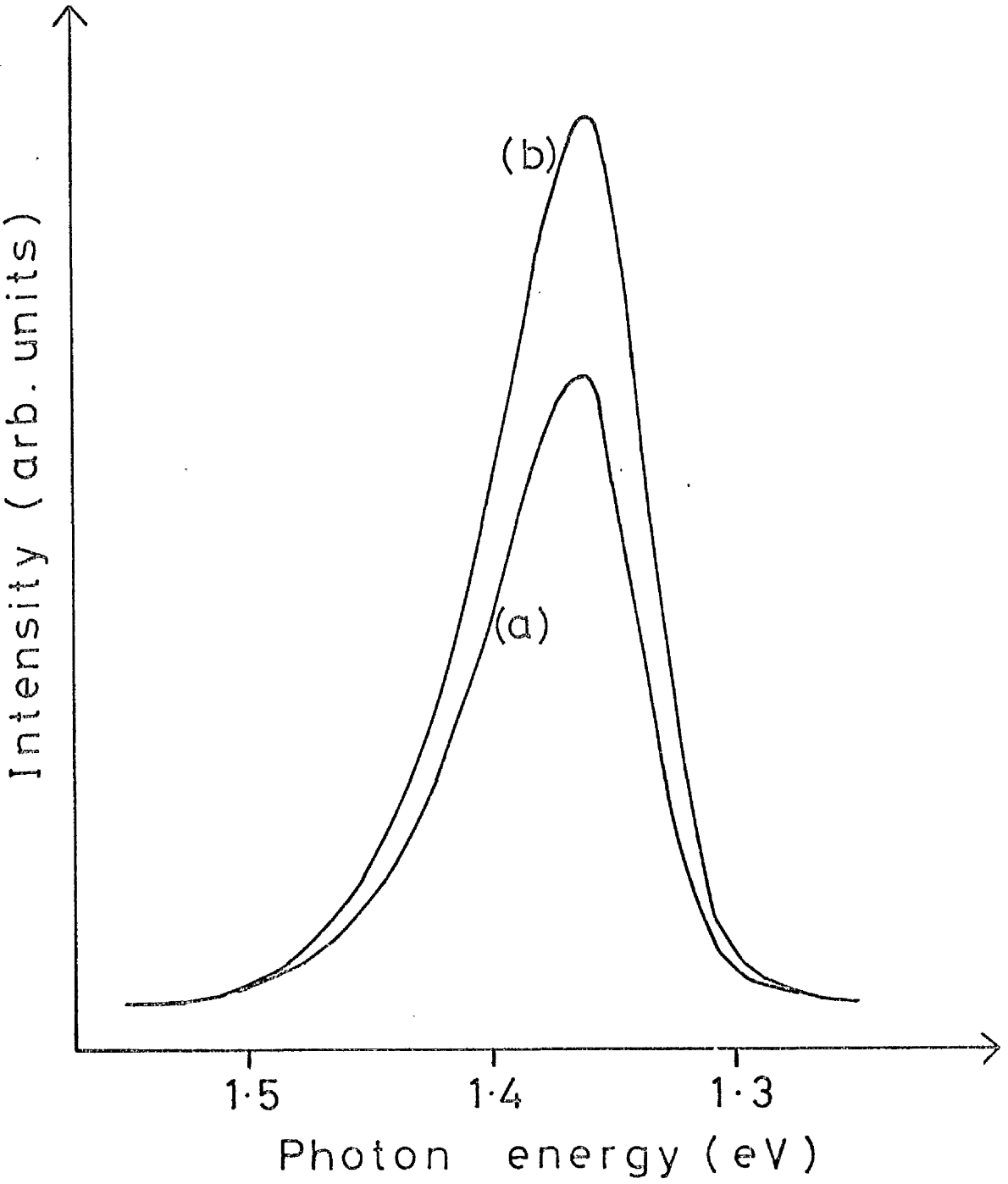

FIG. 3.24 : R.T. photoluminescence from an n-type substrate (10^{18} cm^{-3}).

(a) sputtered/annealed area

(b) masked area

Although the surfaces of argon-ion sputtered and annealed InP substrates have been shown to contain microscopic defects (deep traps), Norris [3.1] reports that such surfaces are smooth and crystalline using the RHEED technique. Norris' observation is confirmed by the fact that high quality (<1μm thick) epitaxial layers have been grown onto sputter-cleaned substrates as indicated by X-ray texture camera and electron channelling analyses (section 3.7.3). Further evidence of the high quality of the layers is provided by the electrical results obtained using the non-contact plasma reflectance technique (section 3.7.4), ie $N_D - N_A \simeq 10^{17} cm^{-3}$ and $\mu = 3,000\ cm^2 V^{-1}s^{-1}$ at R.T., indicating a compensation ratio of between 1 and 2, the influence of the substrate/film interface being minimal on plasma reflectivity measurements. In contrast, the electrical results obtained by Hall-effect measurements (section 3.7.4) would seem to suggest that the layers are of poorer quality with mobilities < 1,000 $cm^2V^{-1}s^{-1}$ at R.T., however, such measurements are seriously influenced by the conducting substrate/film interface and therefore are not representative of the epi-layers themselves.

The extremely weak P.L. response obtained from <1μm thick films grown onto argon-ion sputtered and annealed substrates (section 3.7.5) is probably a consequence of luminescence quenching by deep level non-radiative recombination centres at the substrate/film interface region. Stanley [3.16] has recently grown InP films by MBE using

source materials and growth conditions similar to those which have been described in this chapter but the in-vacuo substrate preparation technique consisted of heating the substrate to $\sim 500^{o}C$ under 10^{-6} Torr of arsenic molecular beam exposure (ie, 3×10^{14} As_4 $cm^{-2}s^{-1}$) rather than argon-ion sputtering and annealing. Such films have exhibited efficient R.T. photoluminescence [3.16] and therefore this result supports the hypothesis of luminescence quenching by deep level substrate/film interface states created by the ion bombardment process.

It is apparent from the measured dependence of the free-carrier concentration in unintentionally doped films on run number (section 3.7.4) that background species in the vacuum system and/or impurities outgassed from the Knudsen ovens are incorporated into growing epitaxial layers as donors (predominately) and acceptors, the background doping level in films being found to decrease with increasing system running time. The ultimate unintentional doping level achieved which was in the range 10^{16}-$10^{17}cm^{-3}$ was probably additionally limited by the purity of the source material used (see section 3.4). Asahi et al [3.17] have recently reported a SIMS analysis of InP films grown by MBE indicating Si to be the main donor impurity in the films with the acceptor impurity Mg and isoelectronic impurities Al and Ga also being detected. It should be noted that Zn which has previously been ascribed to an acceptor level in MBE grown InP films from photoluminescence analysis [3.1] was not detected in the

SIMS study. Si has been shown to be responsible for a shallow donor level in MBE grown GaAs when fused quartz/ Ta resistive substrate heaters are employed [3.18], resulting in unintentionally doped n-typed films. Normally when Mo heaters are used unintentionally doped GaAs films are p-type [3.18]. It is postulated that Si may have been principally responsible for the n-type nature of the unintentionally doped InP films grown in this investigation since both quartz and Ta materials were used in the construction of the Knudsen ovens (see section 3.3).

Amendment to section 3.7.4

Electrical Characterisation of Unintentionally Doped Films

A total of thirty unintentionally doped InP films were grown by MBE and characterised using the Hall-effect technique. The variation of carrier concentration and electron mobility with run number depicted in Fig. 3.22 was repeatedly observed following the InP cell re-charging process which was necessary after five runs and also a bake-out of the vacuum system. The results given on page 75 which are described as typical carrier concentrations and mobilities in run no. 4 to 5 films are in fact mean values obtained from measurements on some twelve films, the variation of both $N_D - N_A$ and μ in the set of twelve run no. 4 to 5 films being < 20%. Of these twelve films four were characterised using the plasma reflectance technique (3.11).

The Plasma Reflectance Technique

The reflectivity spectrum obtained from a semiconductor exhibits a sharp drop to a minimum known as the plasma edge, the position of which is dependent on the carrier concentration. This arises from a resonance between the incident radiation and the natural oscillation frequency of the neutral plasma of free carriers and fixed ions, which is called the plasma frequency. In the simplest case, the refractive index below the plasma frequency is zero and the reflectivity approaches 100%, while above it the index passes through unity and consequently the reflectivity falls to a minimum.

The plasma frequency, ω_p, is given by

$$\omega_p = \left[\frac{(N_D - N_A)e^2}{m^* \varepsilon_\infty \varepsilon_0} \right]^{1/2} \qquad (1)$$

where m^* is the conductivity effective mass, $(N_D - N_A)$ is the carrier concentration and ε_∞ is the high frequency dielectric constant. Thus if the effective mass is known, the carrier concentration may be determined from a measurement of ω_p. ω_p is obtained from the reflectivity as follows. The reflectivity, R, is given by

$$R = \frac{(n-1)^2 + k^2}{(n+1) + k^2} \qquad (2)$$

where n and k are the refractive and absorption indices respectively. n and k may be found from the complex permittivity, $\varepsilon(\omega)$, which may be written using the two-oscillator dielectric model as

$$\varepsilon(\omega) = (n - ik)^2 = \varepsilon_\infty \left[1 + \frac{\omega_L^2 - \omega_T^2}{\omega_T^2 - \omega^2 - i\omega\gamma} \right] - \frac{\varepsilon_\infty \omega_p^2}{\omega(\omega + i/\tau)} \qquad (3)$$

where ω_L and ω_T are the LO and TO phonon frequencies, τ is the scattering time and γ is the phonon damping constant. The two terms on the right-hand side of equation (3) give the separate contributions of the lattice and the free carriers to the permittivity. From a fit to equation (3), ω_p can be found and also an estimate of τ, and hence the mobility μ_{PR}, may be obtained. It should be noted that

$\mu_{PR} \neq \mu_H$ (Hall mobility) and in general μ_{PR} is found to be ~20% less than μ_H. A disadvantage of the plasma reflectance technique is that the mobility cannot be determined exactly since τ can only be estimated from a curve fitting procedure.

CHAPTER 4.

CHAPTER 4

ZINC DOPING OF InP BY MOLECULAR BEAM EPITAXY

4.1 Introduction

As discussed in chapter 2 a major disadvantage associated with the growth of semiconductor materials by MBE is that in general only elements which have a near unity sticking coefficient at the substrate temperatures required for epitaxial growth have been used successfully as dopants. The problem is particularly acute with regard to p-type doping of III-V semiconductors. The group II elements Zn and Cd, for example, which are the most widely used p-type dopants in other epitaxial growth techniques have extremely high vapour pressures at the typical growth temperatures ($\sim 650^{o}C$ for GaAs or $\sim 350^{o}C$ for InP). Zn, for instance, has been shown to have a near zero sticking coefficient on GaAs at temperatures > $100^{o}C$[4.1]. Of the other group II elements Be, which is a low vapour pressure element, has proved the most successful p-type neutral dopant used in the growth of GaAs and $Al_xGa_{1-x}As$ by MBE having a near unity sticking coefficient[4.2]. Be, however, is highly toxic and therefore special safety precautions are required in its handling.

Several years ago Naganuma and Takahashi reported a possible solution to the low sticking coefficient problem of Zn on GaAs[4.3]. These authors grew p-type GaAs layers doped to a level of $\sim 5 \times 10^{19} cm^{-3}$ by placing an

ionisation cell at the opening of a positively biased Zn effusion oven inside their existing MBE growth chamber. A sticking coefficient of ∿ 3% was deduced for low energy Zn ions (200 eV to 1.5 keV) but the electrical quality of the as-grown layers was significantly worse than that of bulk-grown GaAs [4.4]. More recently Bean and Dingle [4.5] employed a differentially pumped Zn ion source external to their growth chamber with mass selection and neutral beam trapping in order to obtain purely Zn^+ species and to minimise ionisation of the large (∿ 10^{-6} Torr partial pressure) As background present during growth. A near unity sticking coefficient was found for Zn^+ on GaAs (c.f. ∿ 10^{-7} for Zn) using this sophisticated apparatus. Furthermore, in contrast to the earlier work, it was found that with a suitable postgrowth anneal Zn^+ doping produced p-type layers with low temperature luminescence and hole mobilities comparable to state-of-the-art LPE layers.

Much less work has been reported on doping studies of InP grown by MBE, in particular p-type doping has received very little attention. Miller et al [4.6] have reported attempts to produce p-type InP using Be and Mg but achieved only limited success. These authors also state that Zn and Cd will not stick on the InP surface during MBE growth because of their high vapour pressures. It is not clear, however, whether this statement was based on experimental evidence or merely an assumption extrapolated from the results on GaAs.

In view of the information discussed above the logical approach to Zn doping of InP by MBE would seem to be via Zn ions as the dopant species and hence this was the method adopted in the work to be described in the following sections. The design, performance and operation of a specially constructed low energy ion source which was incorporated in the InP MBE system as a source of Zn ions are described in chapter 4 (section 4.2 - 4.6). In the latter part of the chapter (section 4.7) rather unexpected results pertaining to the incorporation of neutral Zn into InP grown by MBE are discussed.

4.2 Theory of Ionised-Beam Doping

When MBE layers are doped with ions rather than neutral species doping levels can be directly and instantly known by measuring the ion current at the substrate. In the work described here the ion current was measured by monitoring the compensating electron current flowing between the substrate holder and ground. The method of ion current monitoring used is described in detail in section 4.5.

If the effective sticking coefficient s is defined as the ratio of the number of ions incorporated in the growing layer to the number of ions which arrive at the substrate (obtained from the measured ion current), and if it is assumed that all of the incorporated impurities are electrically activated, then the doping level N is given by

$$N = 2.25 \times 10^{17} \; s \; (J_i/d) \; (cm^{-3}) \qquad (4.1)$$

where J_i is the ion current density (nA cm^{-2}) at the substrate and d is the film growth rate (μm/hr). Hence, if the growth rate d is maintained constant at say 0.5 μm/hr, the doping level is simply proportional to the ion current density at the substrate during growth and is given by

$$N = 4.5 \times 10^{17} \; s \; J_i \qquad (cm^{-3}) \qquad (4.2)$$

Fig. 4.1 shows a plot of the theoretical doping level against ion current density at the substrate for ionised-beam doping. The solid line in Fig. 4.1 is drawn assuming a sticking coefficient of 0.5 for the ions.

4.3 Ion Source Design

The ion source (termed 'Ioncell' [§]) described here was designed and constructed by Oxford Applied Research Ltd., while the characterisation of effusion species and assessment of the ioncell performance were carried out by the author.

Fig. 4.2 shows a photograph of the ioncell which was designed as a direct replacement for conventional molecular beam cells mounted on a 70mm O.D. conflat flange. The low energy ioncell (200 eV → 2 keV) is illustrated schematically in Fig. 4.3. Since the ioncell was designed for operation in an ultra high vacuum system the materials chosen for its construction have relatively low outgassing rates. The material used for the electrical isolator

§ Registered trade mark of Oxford Applied Research Ltd.

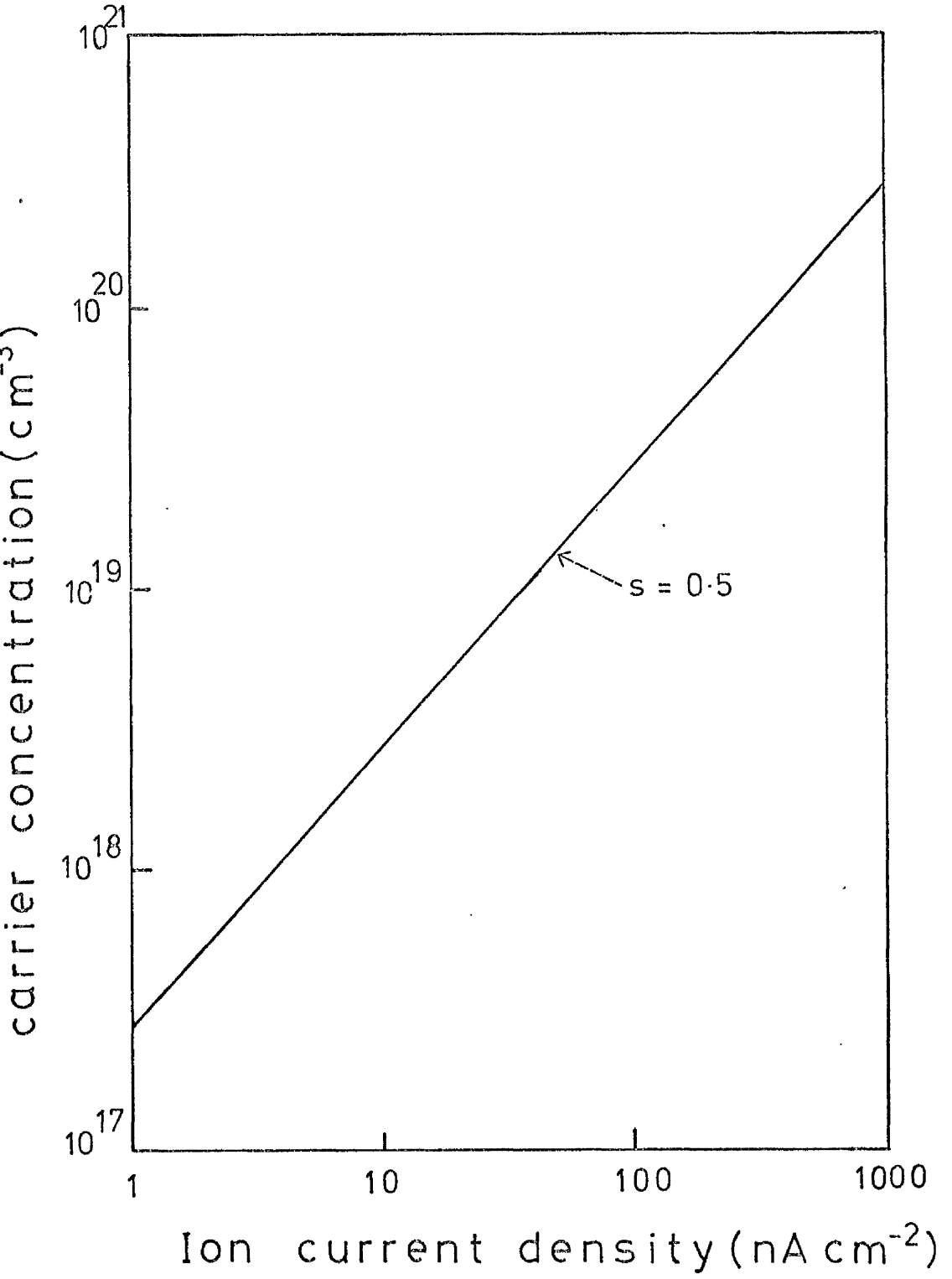

FIG. 4.1 : Theoretical doping level versus ion current at the substrate.

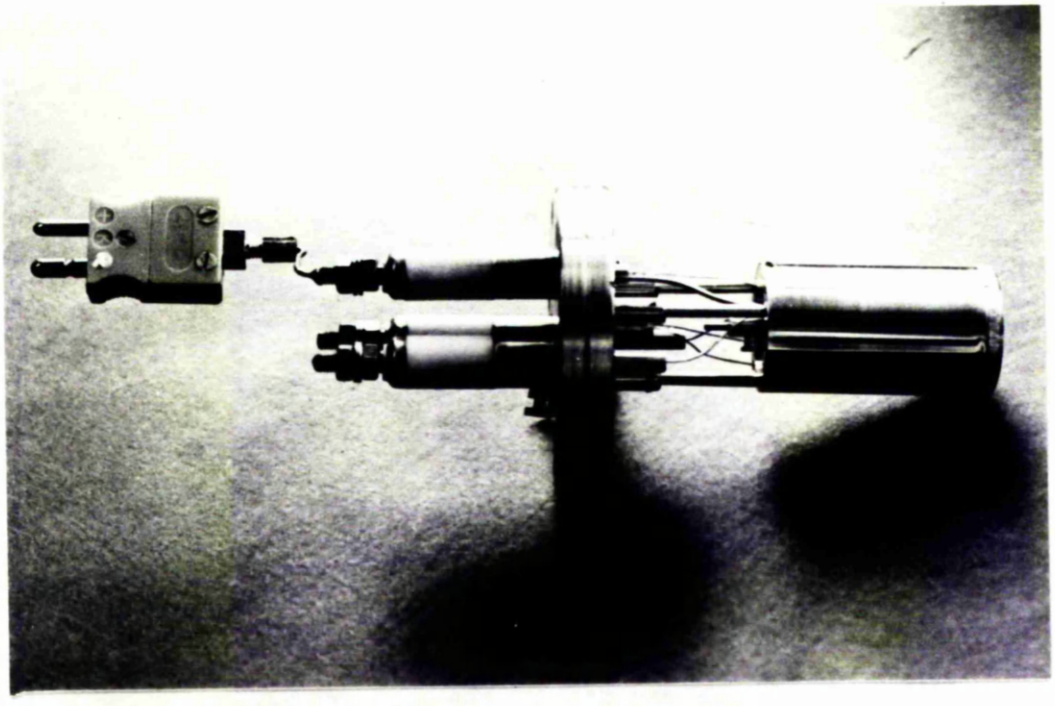

FIG.4.2 : PHOTOGRAPH OF IONCELL.

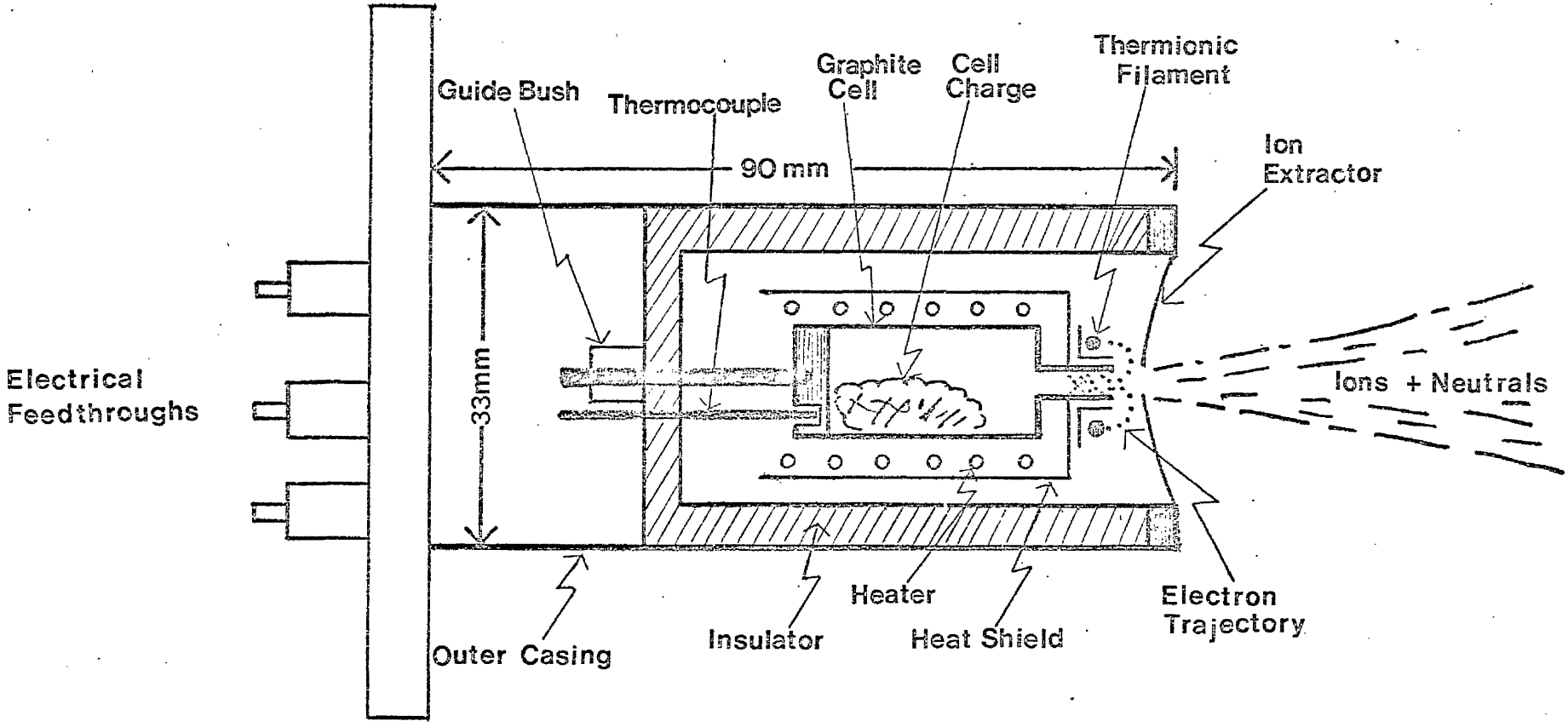

FIG.4.3 : Schematic of the ioncell.

(see Fig. 4.3) is a boric oxide-free high purity grade of hot pressed boron nitride. Other materials of construction are high purity graphite (le Carbone grade 2239 PT) for the cell; high purity Al_2O_3 for the heater former; tantalum for the heater winding and heat shield and Corning grade 9658 machinable glass ceramic for the filament mount.

The ioncell operates as follows: the dopant charge is evaporated on heating through a channel or canal at the orifice of the graphite cell, the cell being maintained at a positive potential (200 eV → 2keV) with respect to ground. Electrons from a heated tungsten filament located out of line-of-sight from the evaporant are electrostatically focussed into the canal and ionise some of the emerging vapour by electron bombardment. Fig. 4.4 shows the geometrical arrangement of the thermionic filament with respect to the cell canal. Positive ions formed by electron impact are accelerated through a grounded exit aperture. Since for doping applications the ion current density required is very low ($< 1\mu A\ cm^{-2}$), the ionising electron energy is designed for simplicity to be equal to the selected ion beam energy. Adequate ionisation is achieved, however, in the source even at electron energies far removed from the maximum ($\sim$ 70 eV for most elements) in the ionisation cross-section curve due to a high electron reflection coefficient exhibited by graphite which aids multiple electron scattering collisions. The magnitude of ion current

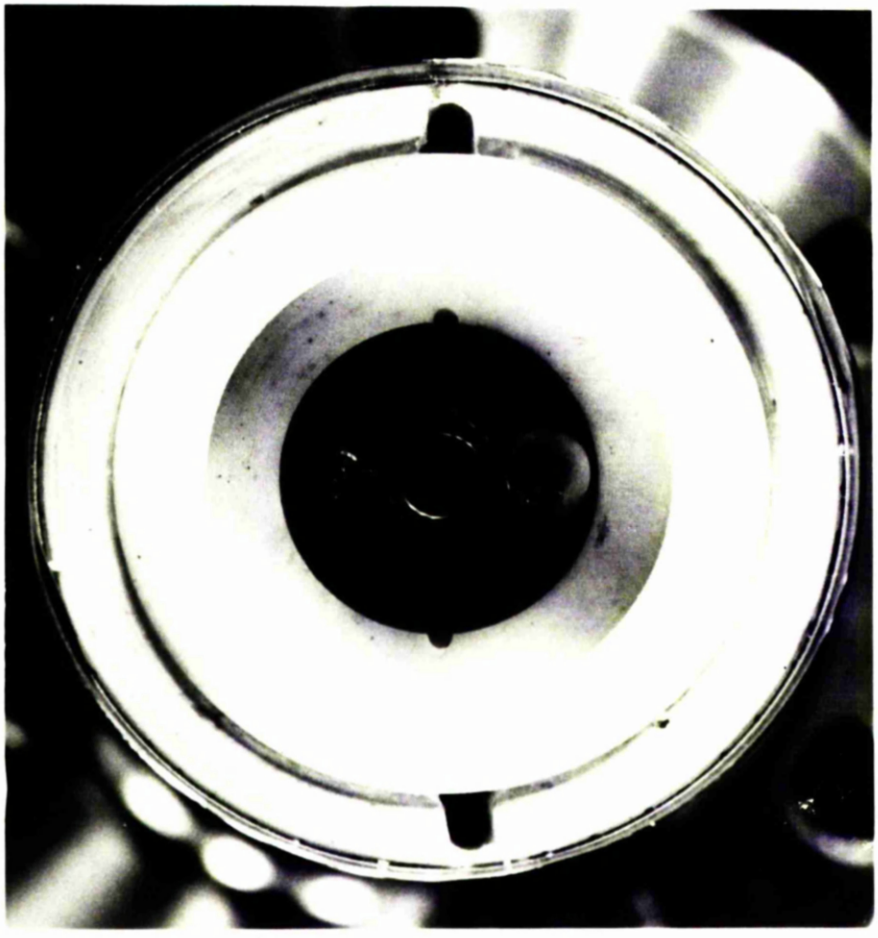

FIG. 4.4 : Ioncell thermionic filament.

required is controlled at a fixed cell temperature by the ionising electron emission current (electron bombardment current). The electron emission current is monitored as drain current in the positive high-voltage supply which provides simultaneously for both ionising electron acceleration and positive ion potential energy. Finally, for fixed ionising electron emission current and ion energy the cell temperature dictates the ion current obtainable with vaporisation of the dopant proceeding according to the Knudsen equation (see chapter 2).

4.4 Characterisation of Species Emitted from the Ion Source

It is important to measure the charge and mass distribution of ion species emerging from the cell in order to estimate the true doping rate during MBE growth from the monitored ion current at the substrate. Although only Zn ion doping by MBE was investigated in this work an ioncell containing Cd was also fully characterised in terms of effusion species and the results obtained from both ioncells are described here.

The Vacuum Generators Q8 quadrupole mass spectrometer previously used to monitor background gases and species present in the MBE system during growth of unintentionally doped InP was used to analyse the neutral and ionised fluxes from both Zn and Cd ioncells. This was possible since the mass spectrometer could be mounted in direct line-of-sight of the ioncell. Neutral isotopes were detected with the quadrupole trap current set to provide

maximum ionising power at an ionisation potential of 70 eV and with zero volts on the ioncell, while ionised species were analysed with zero trap current. With the trap current set to zero the instrument could only mass resolve ions launched into the quadrupole from an external source.

4.4.1 Cadmium Ioncell

The mass spectrum of the neutral Cd beam with the Cd ioncell temperature at 270°C is illustrated in Fig. 4.5(a). The two main groups of peaks are the singly and doubly ionised isotopes of Cd as produced and resolved by the mass spectrometer. All eight isotopes of Cd are present in their correct percentage abundance ratios. The superior resolution of the Cd^+ isotopes compared to the Cd^{2+} isotopes is a function of the quadrupole instrument. Also detected are various residual gases responsible for a pre-bake system pressure of $\sim 5 \times 10^{-8}$ Torr. Fig. 4.5(b) shows the mass spectrum of 200 eV ions emitted by the Cd ioncell; Cd^+ and Cd^{2+} are present. It can be seen that the Cd^+/Cd^{2+} ratios obtained at ionisation electron energies of 70 eV and 200 eV are very similar; a ratio of $\sim$ 2.5 being found in both cases. The mass resolution of energetic ions launched into the quadrupole from the Cd ioncell was found to deteriorate rapidly at ion energies > 200 eV and therefore the Cd^+/Cd^{2+} ratio for ions having energies in the range 200 eV → 2keV could not be determined directly.

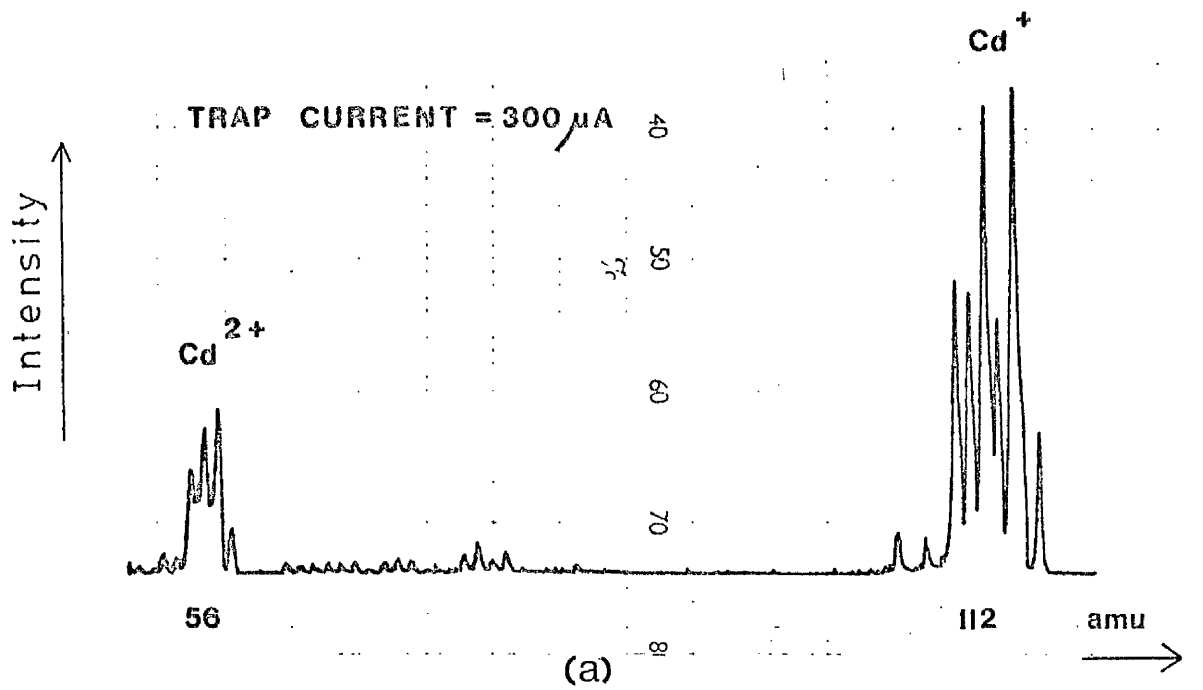

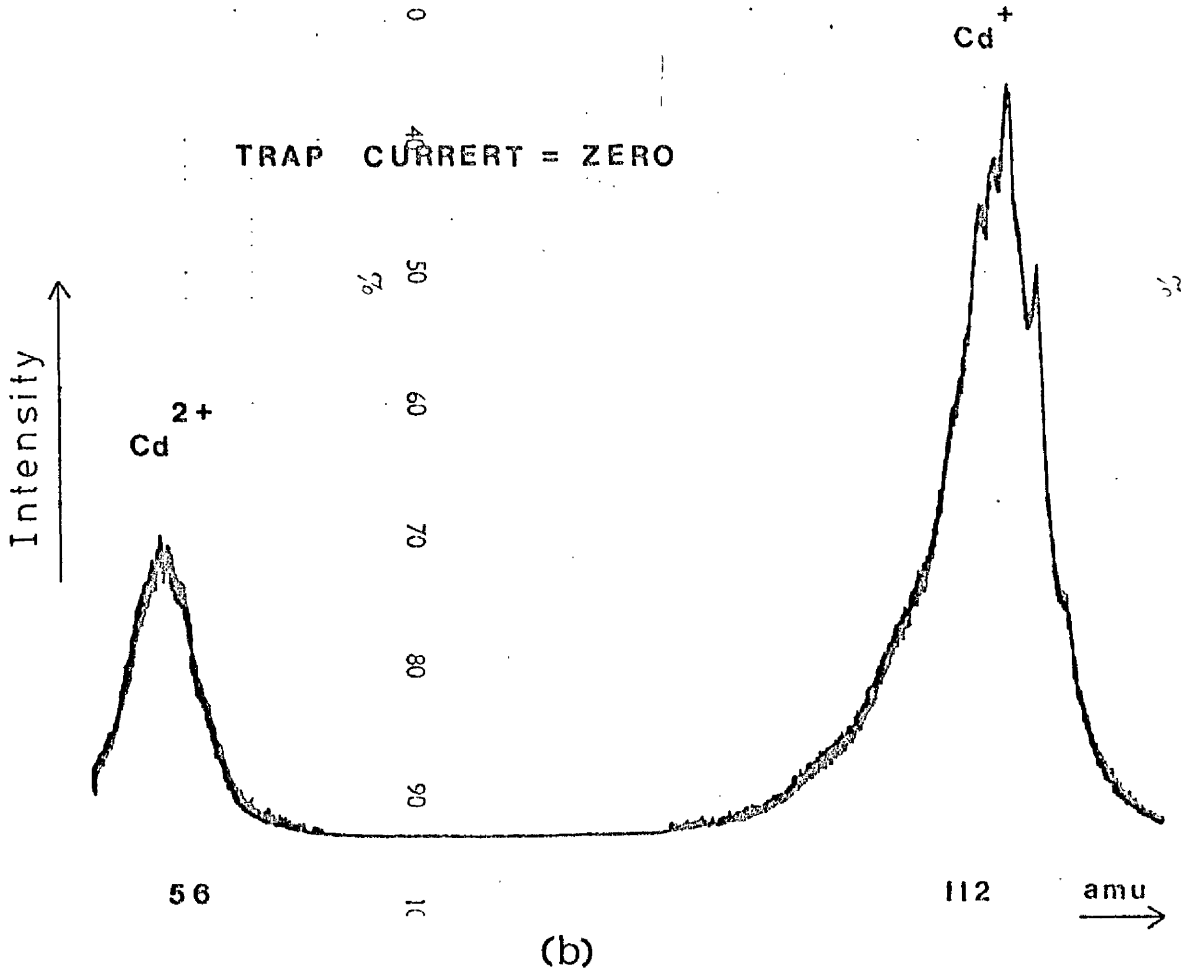

FIG.4.5 : CADMIUM MASS SPECTRA.

(a) Neutral Cd isotopes.

(b) 200 eV Cd ions.

However, it can reasonably be assumed that the ratio found at 70 eV and 200 eV should remain approximately constant for ion energies between 200 eV and 2 keV.

4.4.2 Zinc Ioncell

Fig. 4.6(a) records the mass spectrum of neutral Zn obtained with the Zn ioncell temperature at 320°C. Also detected are background gases responsible for a system pre-bake pressure of $\sim 5 \times 10^{-8}$ Torr. The five isotopes of neutral Zn are better resolved in Fig. 4.7. A 200 eV Zn ion mass spectrum is reproduced in Fig. 4.6 (b); Zn^+ and Zn^{2+} are present in the ratio 9.6 : 1. As mentioned in the preceding section the mass resolution of energetic ions launched into the quadrupole instrument deteriorates at ion energies > 200 eV. This fact is illustrated in Figs. 4.8(a) and 4.8(b) which show the mass spectra of 200 eV Zn ions and 300 eV Zn ions, respectively.

4.5 Ion Source Performance and Efficiency

The following results pertain entirely to the Zn ioncell performance and efficiency, the Cd ioncell results being very similar.

A plot of Zn ion current ($Zn^+ + Zn^{2+}$) detected at the substrate holder as a function of electron emission current for an ion energy of 2 keV is shown in Fig. 4.9, the Zn cell temperature being held constant at 320°C. No correction has been made to account for possible secondary electron/ion effects. The current due to ionised background gases was below the minimum detectable

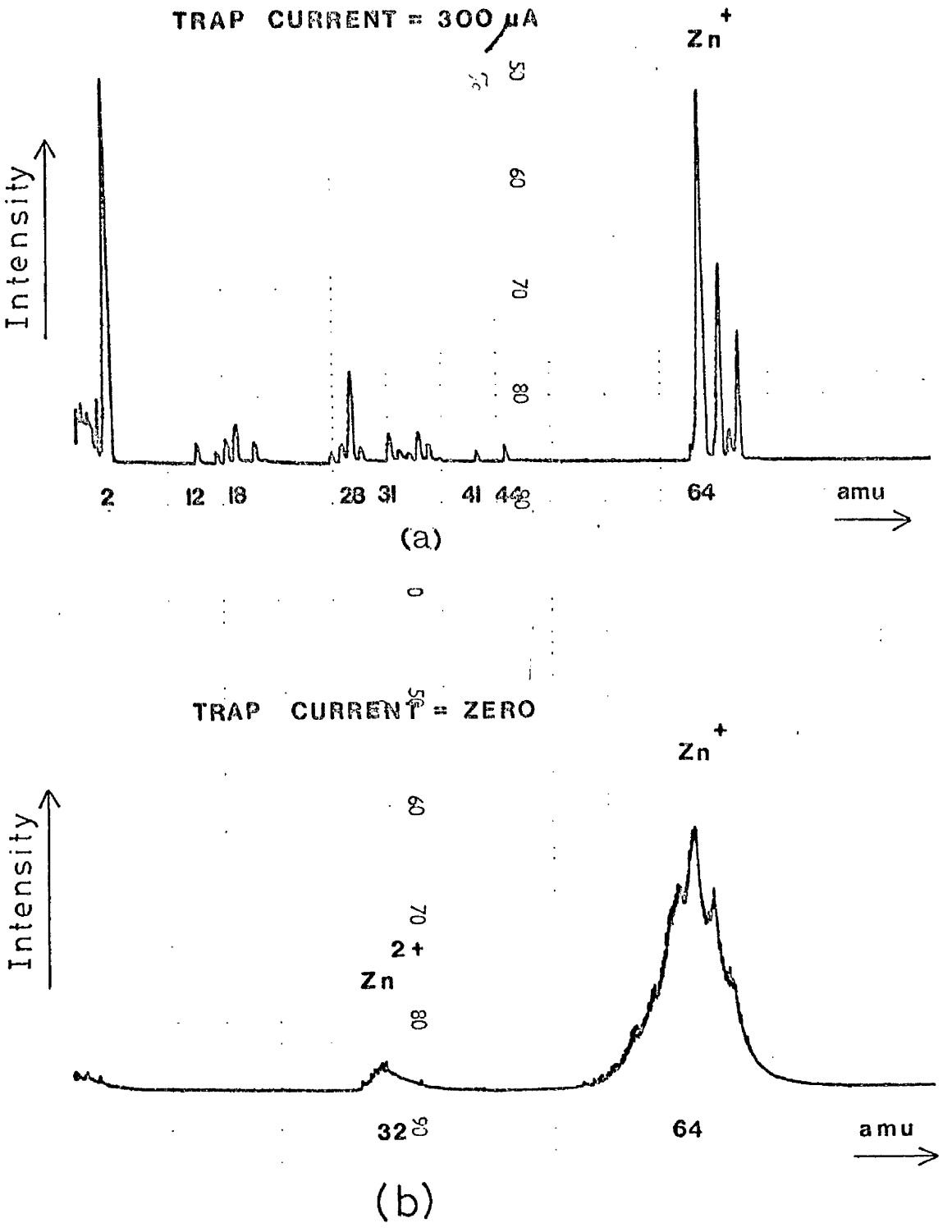

FIG.4.6 : ZINC MASS SPECTRA.

(a) Isotopes of neutral Zn plus residual gases (5×10^{-8} T pressure).

(b) 200eV Zn ions.

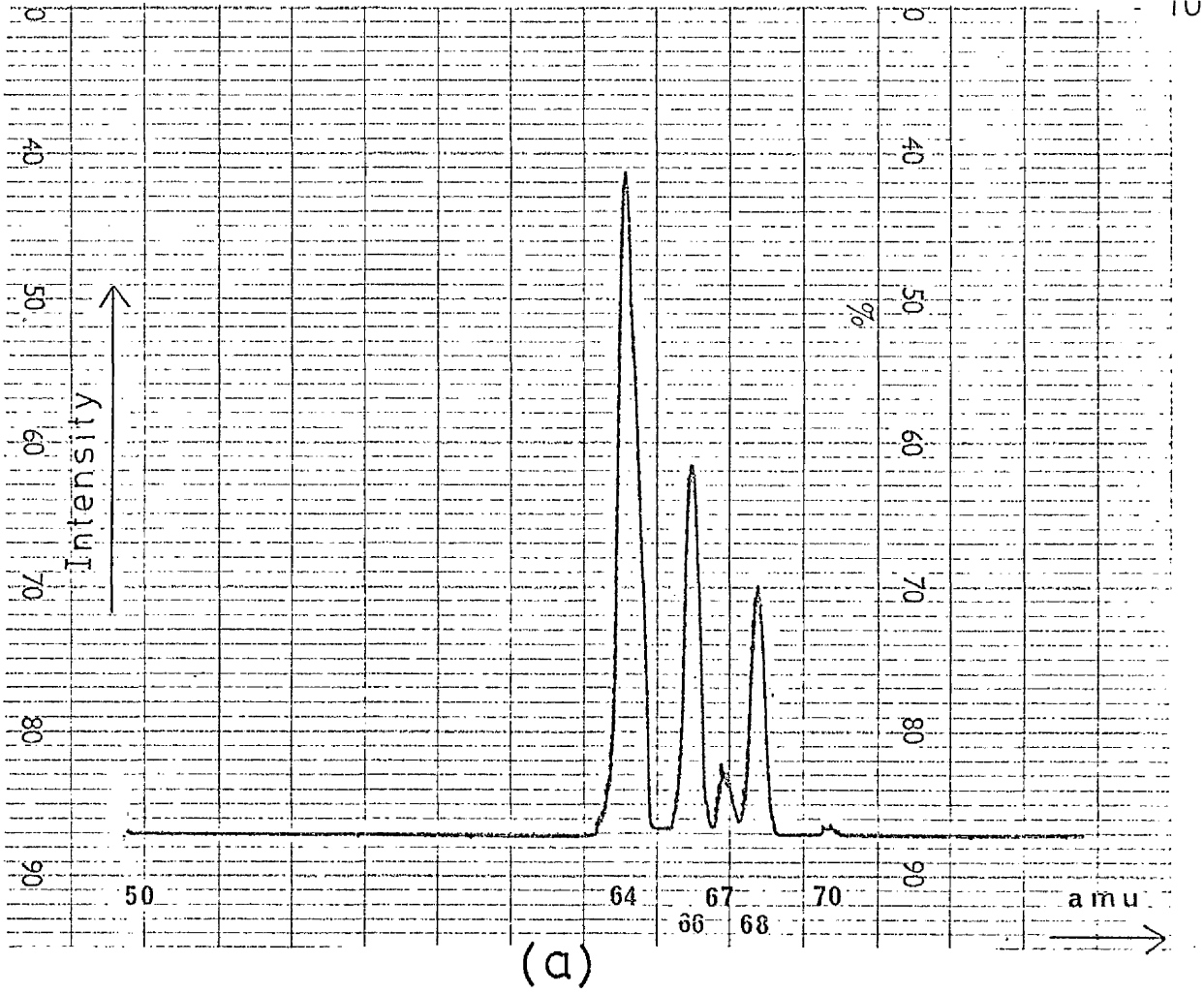

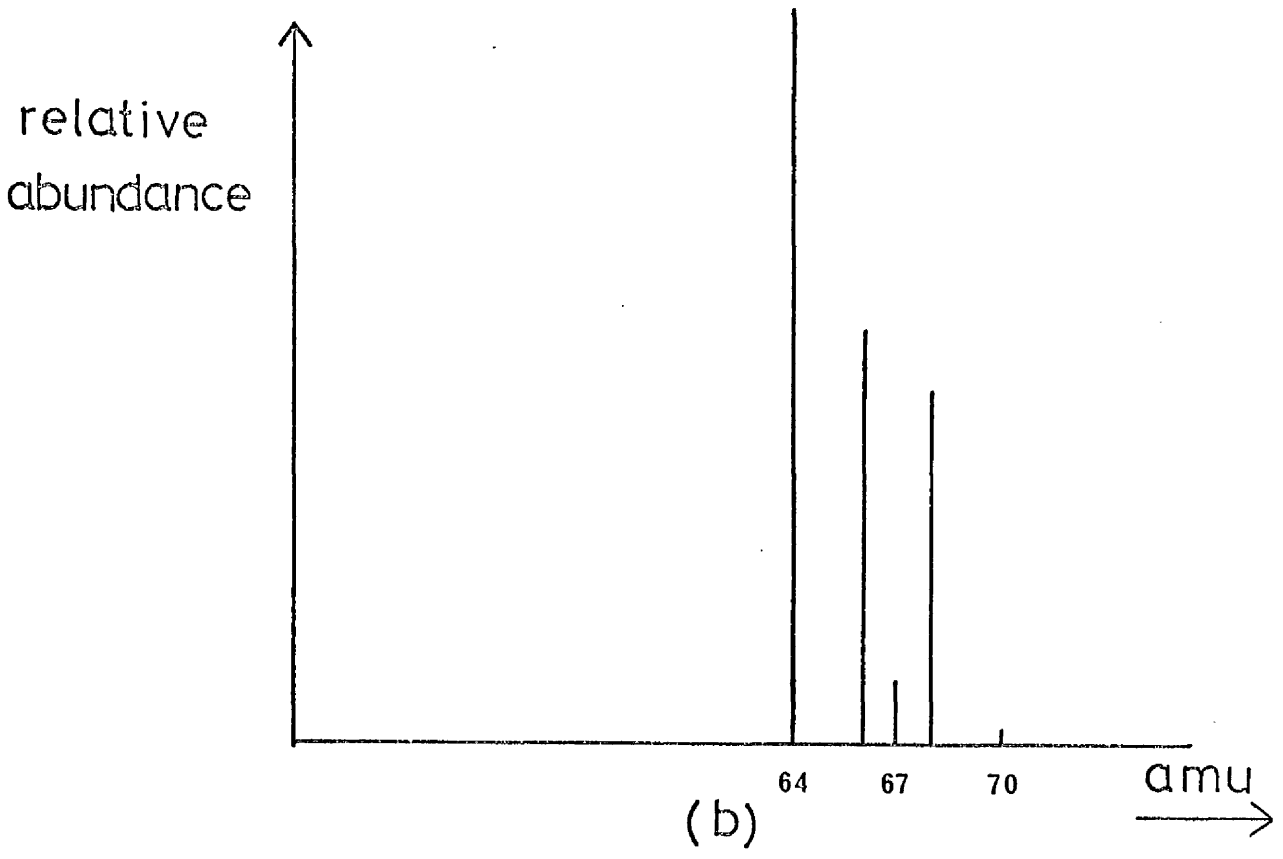

FIG.4.7 : ISOTOPIC DISTRIBUTION OF Zn.

(a) Experiment (b) Theory.

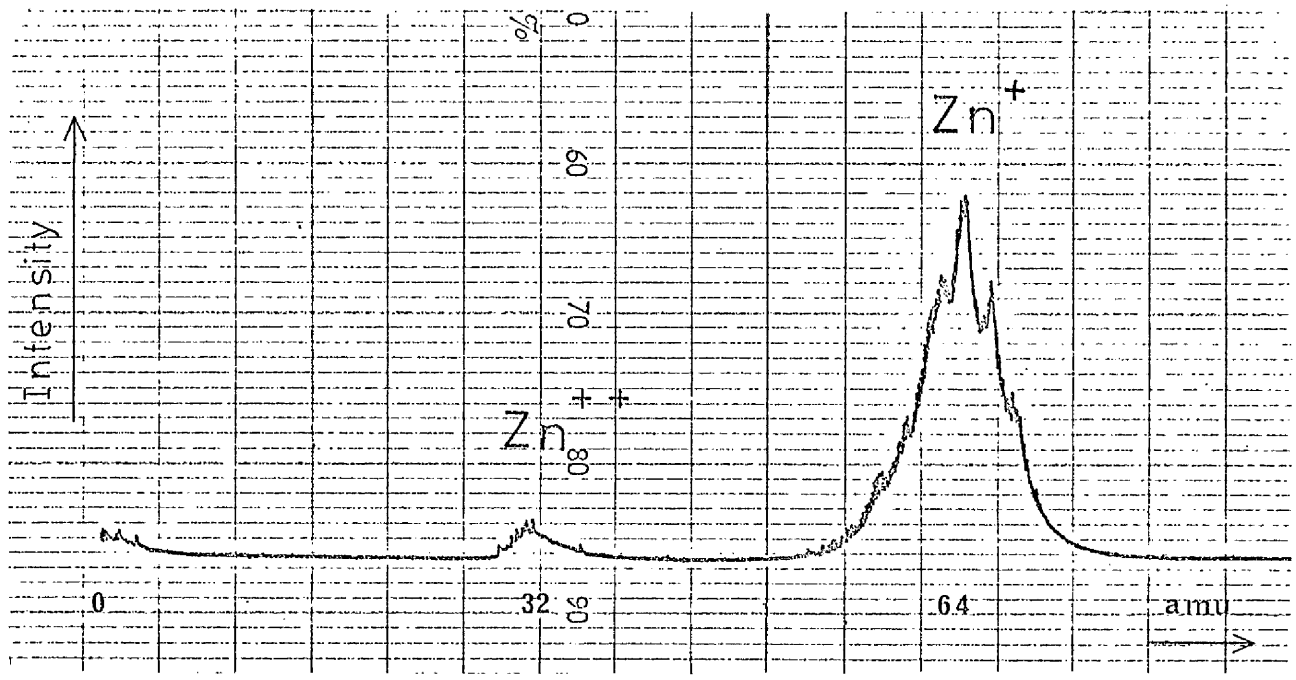

(a)

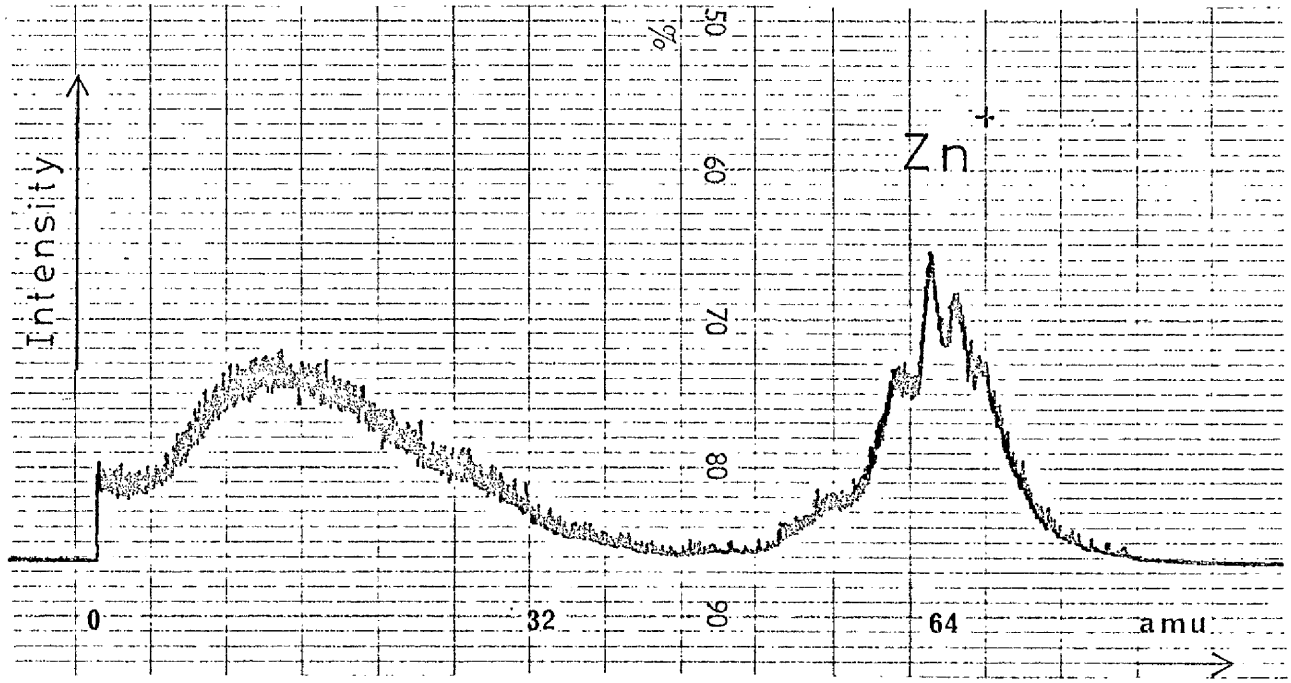

(b)

FIG. 4.8 : MASS SPECTRA OF Zn IONS.

(a) 200eV Zn ions.

(b) 300eV Zn ions.

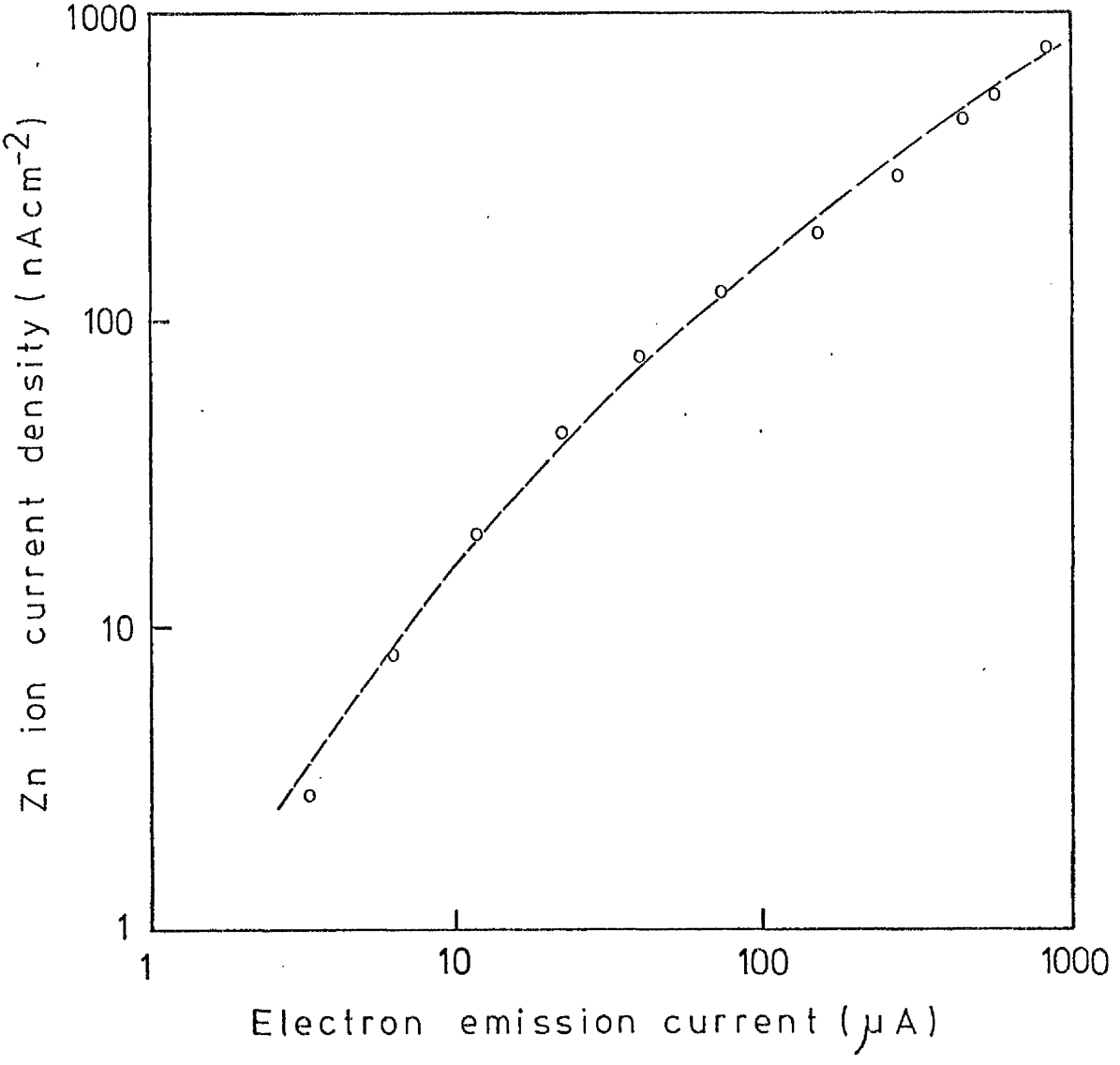

FIG. 4.9 : Measured ($Zn^{+}+Zn^{2+}$) current at the substrate versus electron ionising current.

Zn ion energy = 2 keV

level, $\sim$ 1 nA cm^{-2}, with the cell temperature at $20^{o}C$ (ie, zero Zn effusion) but with maximum ionising power (2 keV, 1 mA emission current) on the ioncell. As can be seen from Fig. 4.9 the Zn ion current at the substrate increases monotonically over three orders of magnitude with increasing electron emission current providing in theory wide control over the acceptor impurity concentration (see Fig. 4.1). In practice the Zn ion current required during MBE layer growth was obtained by setting the ioncell filament current at a particular level. A calibration plot of Zn ion current density at the substrate versus ioncell filament current for various Zn ion energies in the range 200 eV → 2 keV is shown in Fig. 4.10. The cell temperature was again held at $320^{o}C$.

With a view to optimising the ioncell efficiency the position of the thermionic filament with respect to the canal at the cell orifice (see Fig. 4.4) was varied. The effect of changing the filament position was to alter the trajectory of electrons emitted from the filament to the inner canal wall. Maximum efficiency was obtained with the filament located directly in line with the cell orifice plane, shown as position 1 in Fig. 4.11. The electron current collected in the canal (emission current) at a particular filament current was found to be maximised with the filament located in this position. Fig. 4.11 shows plots of electron emission current versus filament current for two filament locations. The data

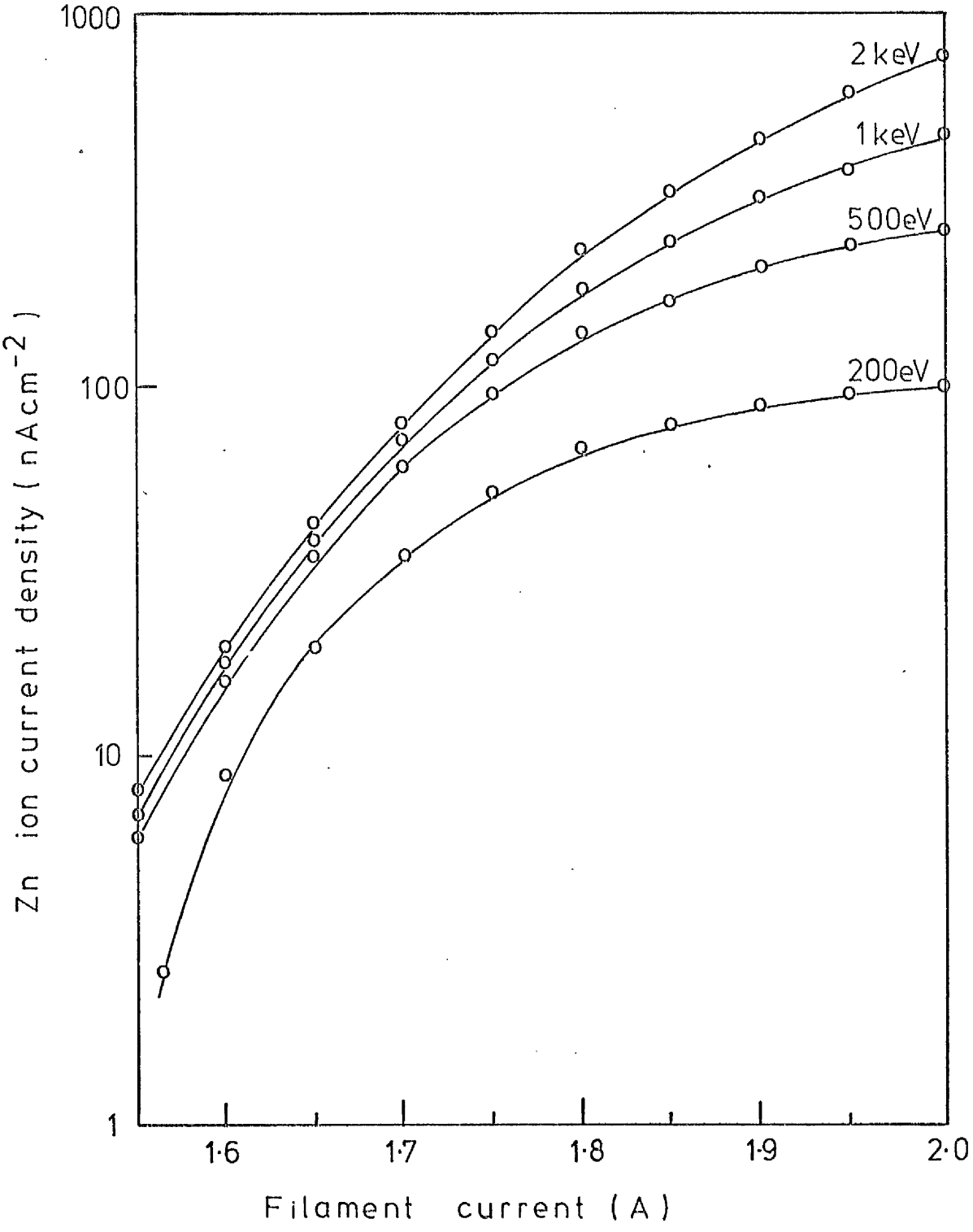

FIG. 4.10 : Calibration plots of Zn ion current at the substrate versus filament current for various ion energies.

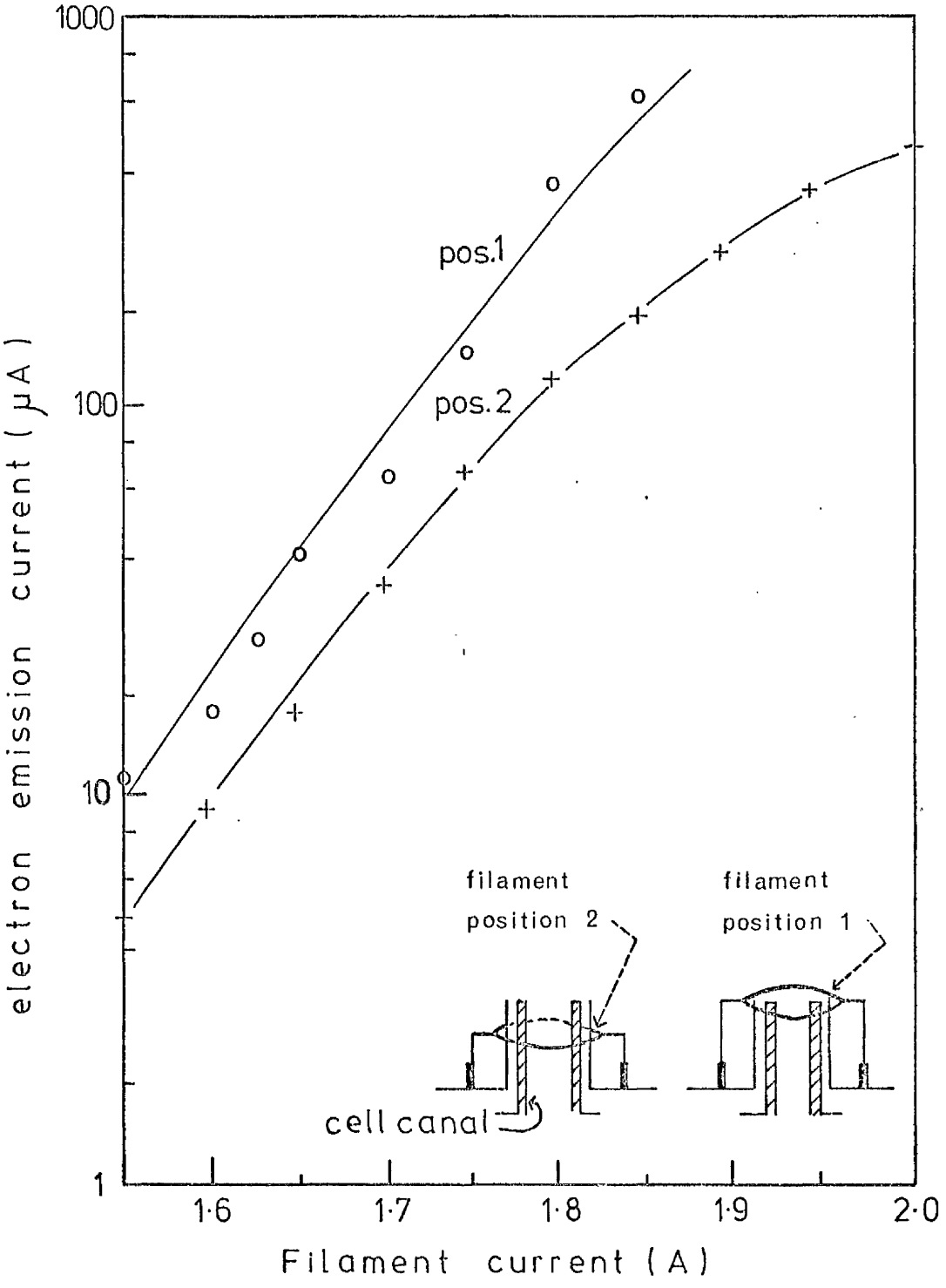

FIG. 4.11 : Electron ionising current versus filament current for two filament positions.

recorded in Figs. 4.9 and 4.10 was obtained with the filament in the optimum position. An estimate of the ioncell efficiency, defined as the ratio of Zn ion to Zn neutral species emitted by the source, can be made using the ion current monitored at the substrate and the Knudsen equation for molecular flow as given in chapter 2. From Fig. 4.10 the maximum Zn ion current density measured at the substrate was $1\mu A\ cm^{-2}$ with maximum ionising power on the ioncell and a cell temperature of $320^{o}C$. For a cell temperature of $320^{o}C$ the Knudsen equation yields a theoretical Zn neutral flux density at the substrate of $\sim 2 \times 10^{14}\ cm^{-2}\ s^{-1}$. Thus, the maximum ioncell efficiency η is given by

$$\eta = \frac{\text{(ion current density at substrate)}/q}{\text{neutral beam flux density}}$$

$$= \frac{1 \times 10^{-6}/1.6 \times 10^{-19}}{2 \times 10^{14}}$$

$$\simeq 3\%$$

It should be noted here that the neutral Zn flux level of $\sim 2 \times 10^{14}\ cm^{-2}\ s^{-1}$ required to obtain a maximum Zn ion current density of $1\mu A\ cm^{-2}$ at a Zn cell temperature of $320^{o}C$ is similar in magnitude to the In flux level ($\sim 3 \times 10^{14}\ cm^{-2}\ s^{-1}$) normally used during epitaxial growth (see chapter 3).

In order to maintain a constant Zn ion dose at the substrate, corresponding to a uniform doping profile, an ion current control circuit shown in Fig. 4.12 was

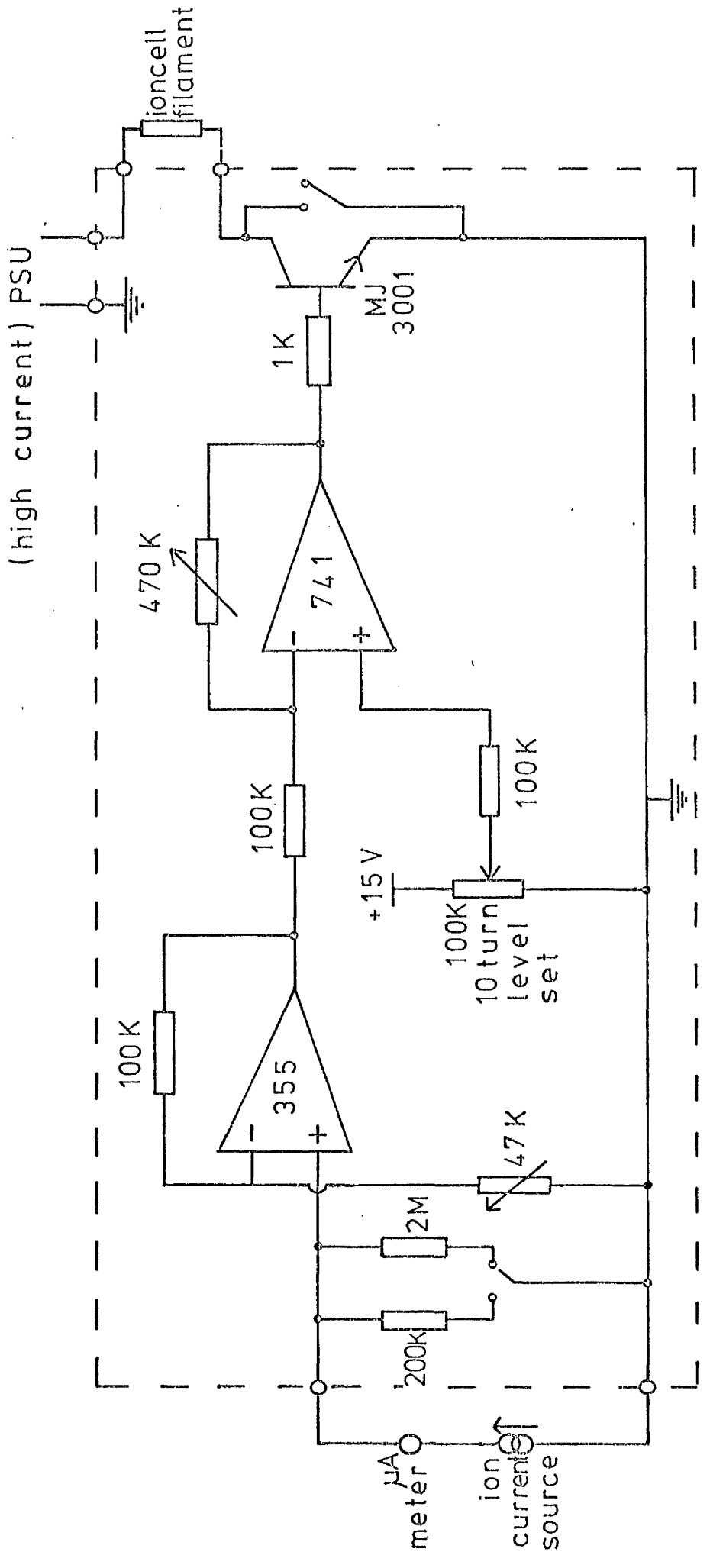

FIG.4.12 : Ion current control circuit.

designed. The circuit operates by varying the ioncell filament current about a set point in response to ion current fluctuations, ie, if the ion current increases above the desired level the circuit reduces the filament current and hence reduces the ionising power of the ioncell. The opposite response results due to a decrease in the desired ion current level. The circuit shown in Fig. 4.12 stabilised the ion current at the substrate to $\sim \pm 1\%$.

4.6 Growth of InP in the presence of Zn Ions and Neutrals

A Zn ioncell containing 5 N(8) purity Zn was incorporated into the MBE system previously used to grow unintentionally doped InP as described in chapter 3. The basic substrate preparation techniques, both ex-vacuo and in-vacuo, and growth procedures outlined in chapter 3 were employed.

A schematic diagram of the growth arrangement with the Zn ioncell added is shown in Fig. 4.13. As can be seen from the figure the total Zn ion current arriving at the substrate during growth was estimated by measuring the electron current flowing between the substrate holder and ground. The Zn ion current density ($\mu A\ cm^{-2}$) was calculated from a knowledge of the substrate holder surface area and the Zn ion flux distribution at the substrate holder (see Fig. 4.14). 1μm thick Zn ion-doped InP films were grown onto Fe-doped semi-insulating substrates cut 2^{o} off the [100] direction with Zn ion

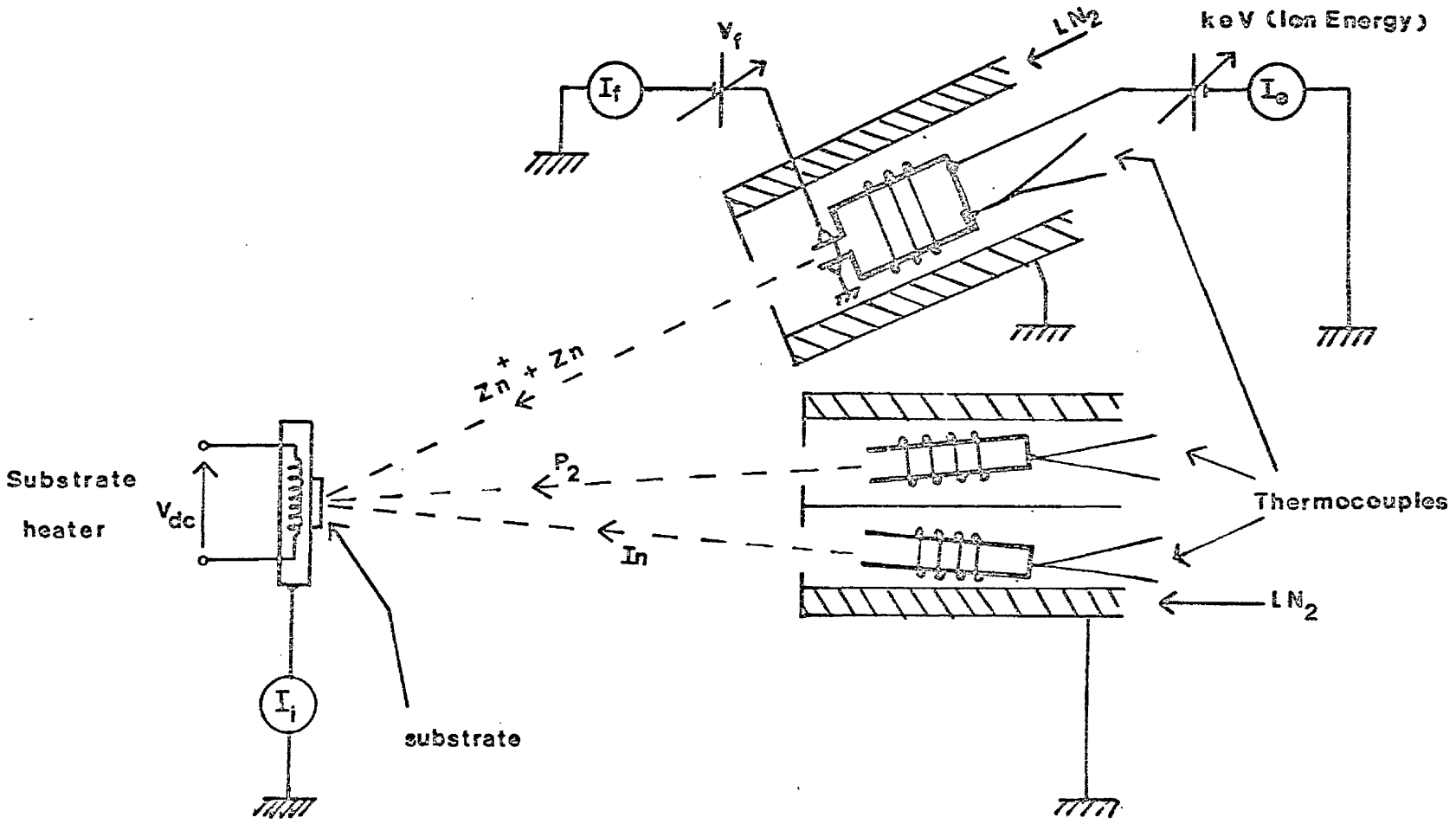

FIG. 4.13 Schematic of Zn ion doping arrangement.

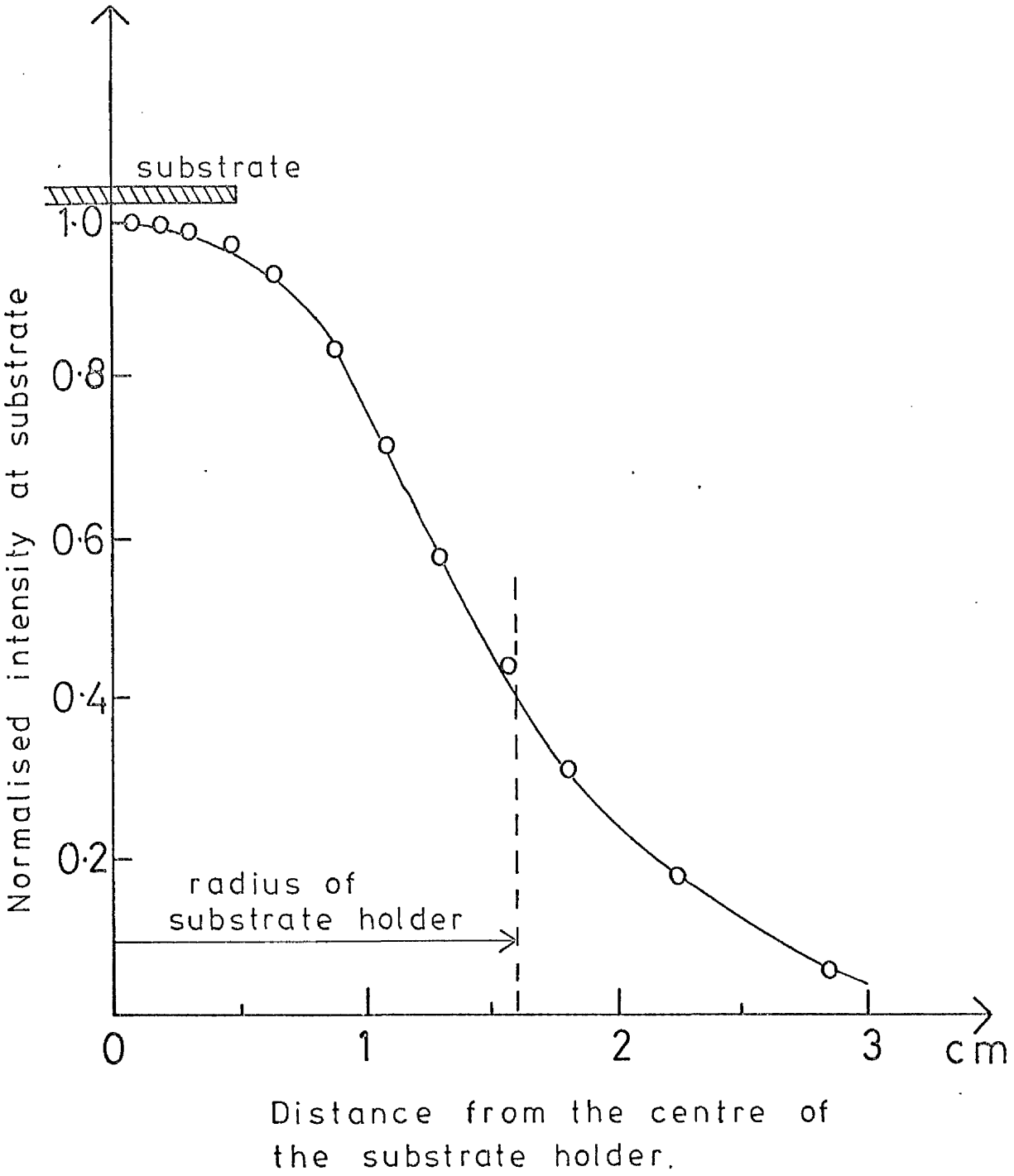

FIG. 4.14 : Lateral Zn ion flux distribution at the substrate plane.

current densities at the substrate ranging from 2nA cm^{-2} to 1μA cm^{-2}, corresponding to theoretical doping levels ranging from 4.5×10^{17} cm^{-3} to 2.25×10^{20} cm^{-3} (see Fig. 4.1); the Zn ion energy was 1 keV with the cell temperature maintained throughout at 320°C. The substrate temperature during film growth was 360°C.

4.6.1 Visual and Microscopic Assessment of Layers

The Zn ion-doped films appeared mirror-like and featureless to the naked-eye over the full range of Zn ion current densities used. Microscopically the surfaces of the films were also featureless and smooth as shown in Figs. 4.15 and 4.16. Fig. 4.15 shows a Nomarski phase contrast micrograph of the surface of an InP film grown in the presence of a beam of 1keV Zn ions (plus Zn neutrals) with an ion current density at the substrate of 1μA cm^{-2}. A scanning electron micrograph of the same surface is shown in Fig. 4.16. (The particle to the top right hand corner of the micrograph was located to aid focussing.)

4.6.2 Crystallographic Assessment of Layers

The crystallographic quality of as-grown Zn ion-doped layers was examined by both X-ray texture camera (A.1) and electron channelling (3.10) analyses. Figs. 4.17 and 4.18 show the texture camera and electron channelling patterns, respectively, obtained from a film grown in the presence of 1keV Zn ions, the ion current density being 1μA cm^{-2}. The X-ray diffraction pattern

X 400 MAG.

FIG. 4.15 : Nomarski phase contrast micrograph of surface of a Zn ion doped InP film.

$J_i = 1 \mu A\, cm^{-2}$.

Ion energy = 1 keV.

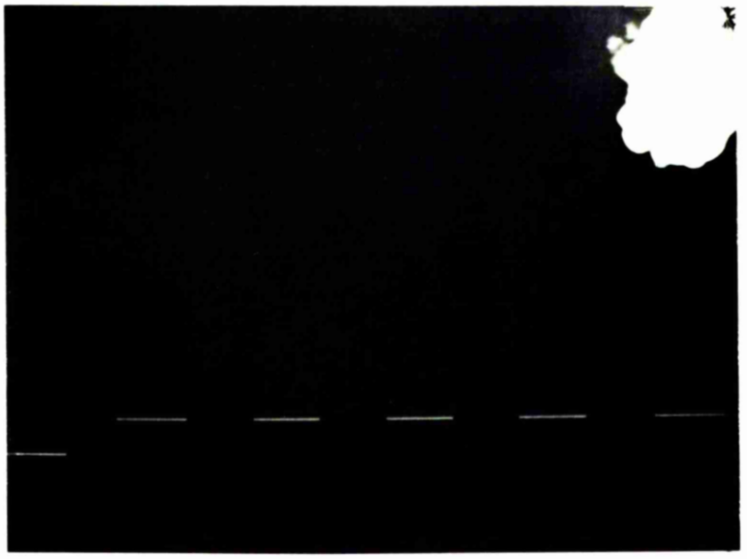

1 μm markers

X 10K MAG.

FIG.4.16 : SEM micrograph of surface of a Zn ion doped InP film.

$J_i = 1 \mu A cm^{-2}$.

Ion energy = 1keV.

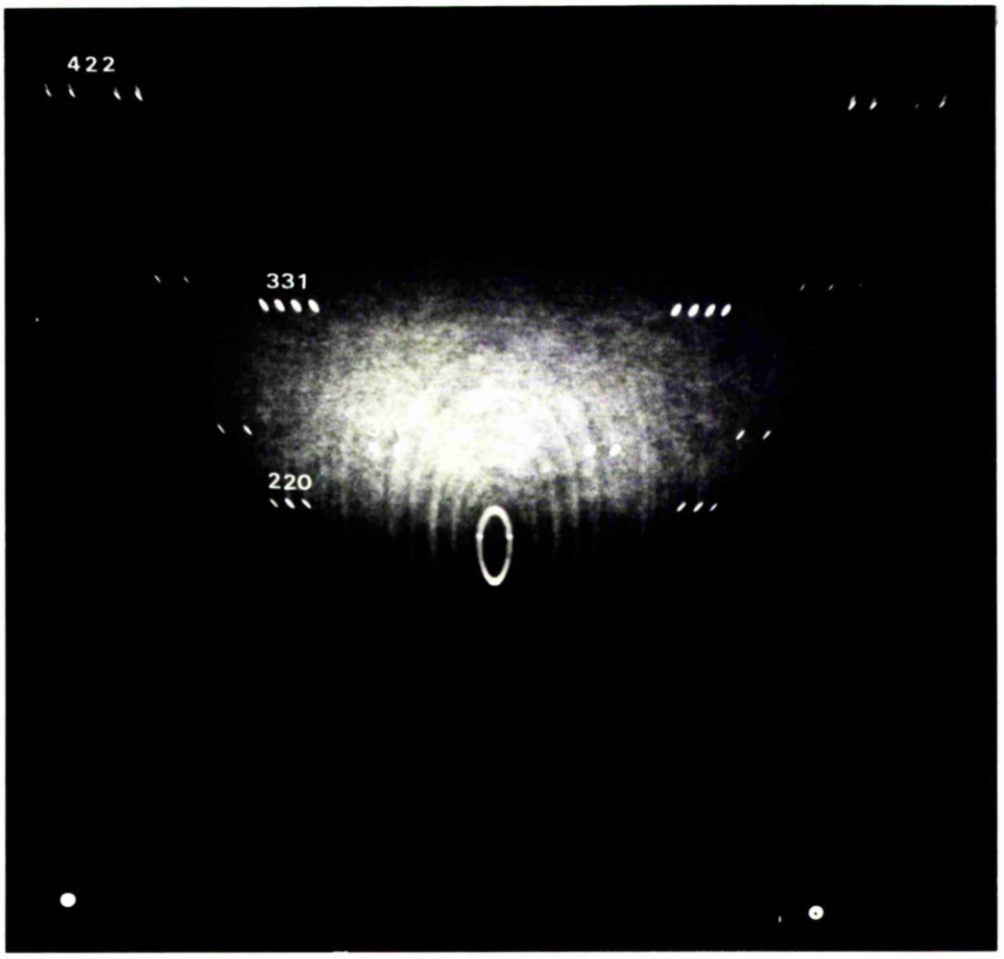

FIG. 4.17 : Texture camera pattern from a Zn ion doped InP film.

$J_i = 1 \mu A cm^{-2}$.

Ion energy = 1keV.

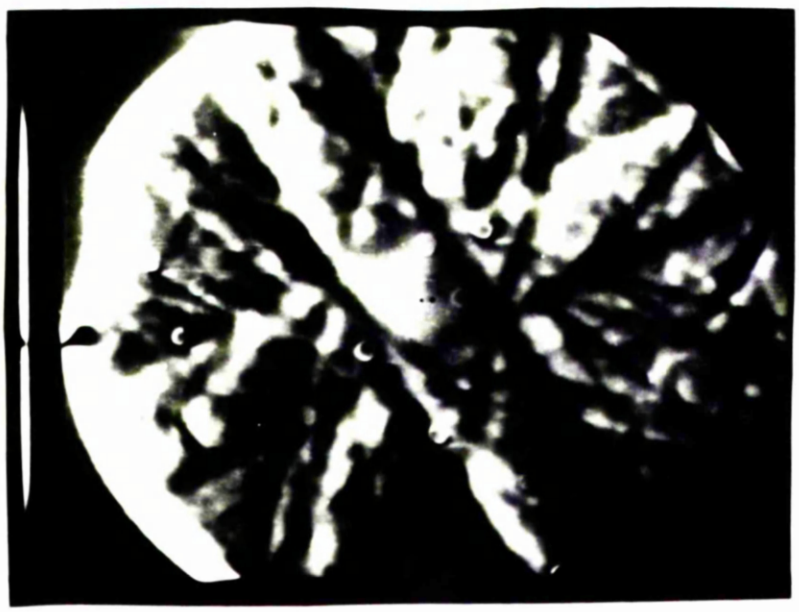

FIG 4.18 : Electron channelling micrograph from a Zn ion doped InP film.

$J_i = 1 \mu A cm^{-2}$.

Ion energy = 1 keV.

shown in Fig. 4.17 which was recorded using CrKα radiation is indicative of twin-free epitaxial material and is identical to that obtained from unintentionally doped films. A high degree of film surface crystallinity is also indicated by the electron channelling pattern recorded in Fig. 4.18. Thus the as-grown Zn ion-doped films were shown to be good quality single crystal.

4.6.3 Electrical Characterisation of Layers

The Zn ion-doped films were characterised electrically by plasma reflectivity measurements since as discussed in chapter 3 the sputtering/annealing substrate cleaning procedure converts the surface of semi-insulating substrates to n-type with $n \simeq 3 \times 10^{16}$ cm^{-3}. The result of the electrical measurements was that the Zn ion-doped layers were n-type, with $n \simeq 10^{17}$ cm^{-3} and $\mu \simeq 3{,}000$ cm^2 V^{-1} s^{-1} at 300K, irrespective of the Zn ion current density used during epitaxial layer growth.

4.6.4 Chemical Analysis of Layers

Atomic absorption spectrometry analysis [4.7] was performed on the full range of Zn ion-doped films in order to determine the level of chemical incorporation of Zn in the layers as a function of Zn ion current density at the substrate. The outcome of this analysis was that all the films had a Zn atom concentration of $\sim 3 \times 10^{20}$ cm^{-3}, irrespective of the Zn ion current density used. This result lead to spectulation that Zn

neutrals were being incorporated into the growing epi-layers since Zn concentrations as high as 3×10^{20} cm^{-3} were not possible from the measured ion current densities at the substrate. The following section describes experiments which were performed using a neutral Zn molecular beam in order to verify this hypothesis.

4.7 Neutral Zn doping of InP

The Zn ioncell was used as the source of a neutral Zn molecular beam simply by thermally evaporating Zn from the Knudsen oven with zero ionising power placed on the ioncell. 1μm thick Zn-doped films were grown onto Fe-doped semi-insulating substrates with the Zn cell temperature being varied over a range from 190°C to 360°C. The substrate temperature was maintained at 360°C.

4.7.1 Chemical Analysis of Layers

Fig. 4.19 shows a plot of Zn atom concentration in the films versus the reciprocal of the Zn cell temperature. The experimental points were obtained by atomic absorption spectrometry while the solid line represents the theoretical Zn concentration as calculated using the standard Knudsen equation for molecular effusion (see chapter 2) and assuming a unity sticking coefficient for the Zn atoms. As can be seen from Fig. 4.19 Zn is chemically incorporated into InP grown by MBE with a near unity sticking coefficient to concentrations of $\sim 10^{19}$ cm^{-3} whence, with higher Zn fluxes, the Zn content appears to saturate at an incorporation level of $\sim 6 \times 10^{20}$ cm^{-3}.

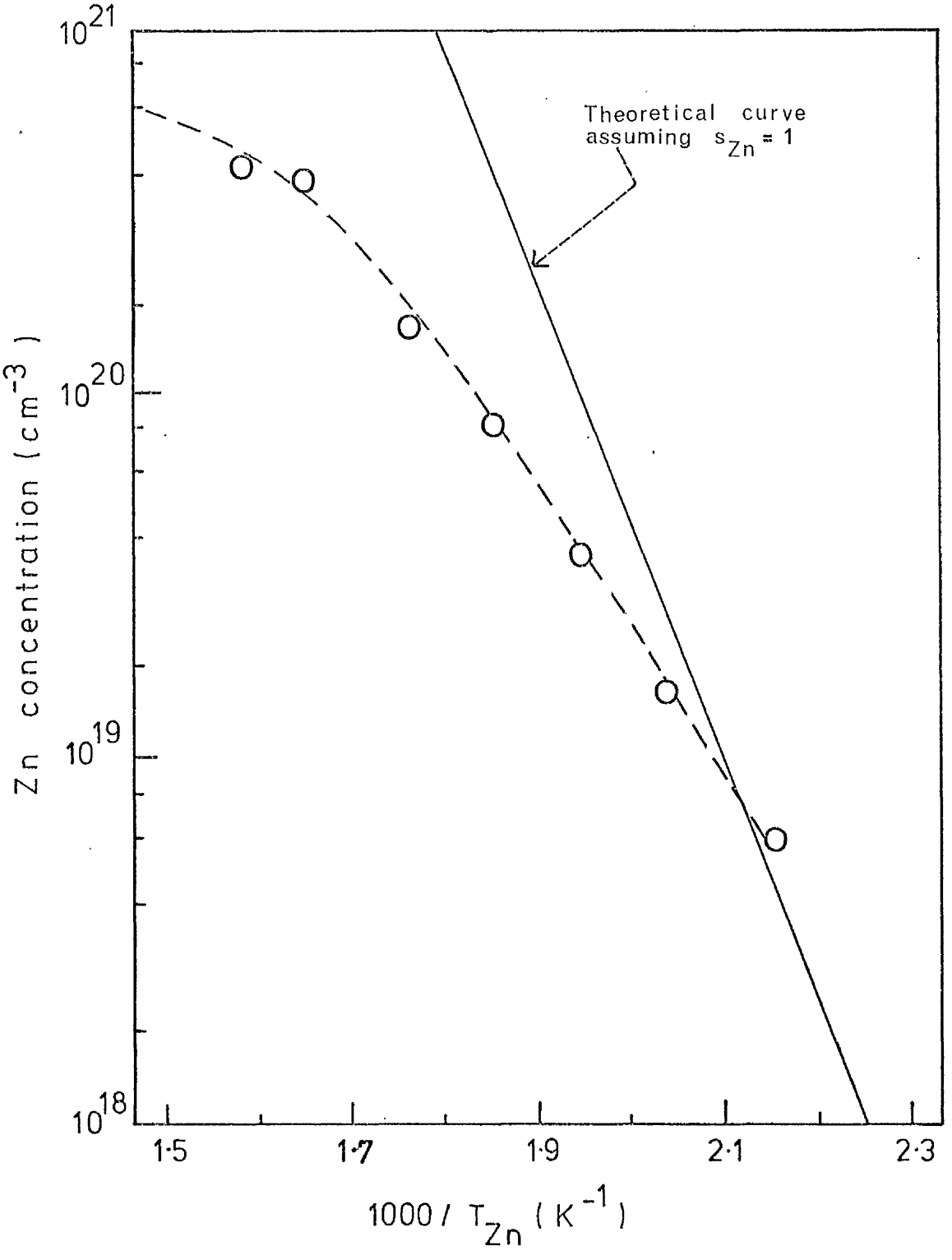

FIG. 4.19 : Zn atom concentration in InP films versus Zn oven temperature.

4.7.2 Crystallographic Assessment of Layers

The neutral Zn doped films were mirror-like and featureless and were shown to be good quality single crystal by both X-ray texture camera and electron channelling analyses. Figs. 4.20 and 4.21 show texture camera and electron channelling patterns, respectively, obtained from a film having a Zn atom concentration of 3×10^{20} cm^{-3}. Double crystal X-ray diffractometry analysis (see reference 4.16), which is capable of resolving lattice constant changes $\Delta a/a$ as small as 10^{-3}%, failed to reveal any evidence for lattice strain (as judged by a small change in the lattice constant) in films with Zn atom concentrations in excess of 10^{20} cm^{-3}. A double crystal diffractometry trace which illustrates the (400) Bragg reflection obtained from a film with a Zn atom concentration of 3×10^{20} cm^{-3} is shown in Fig. 4.22. The figure shows a single peak with a half-width of $\sim$ 8 secs. of arc with no additional sidelobes present which is indicative of strain-free single crystal material.

4.7.3 Electrical Characterisation of Layers

Electrical characterisation by plasma reflectivity measurements revealed that the films were n-type, with $n \simeq 10^{17}$ cm^{-3} and $\mu \simeq 3{,}000$ cm^2 V^{-1} s^{-1} at 300K, irrespective of the Zn flux level used. Hence, the electrical activity of Zn in as-grown films is judged to be less than $1 : 10^3$,

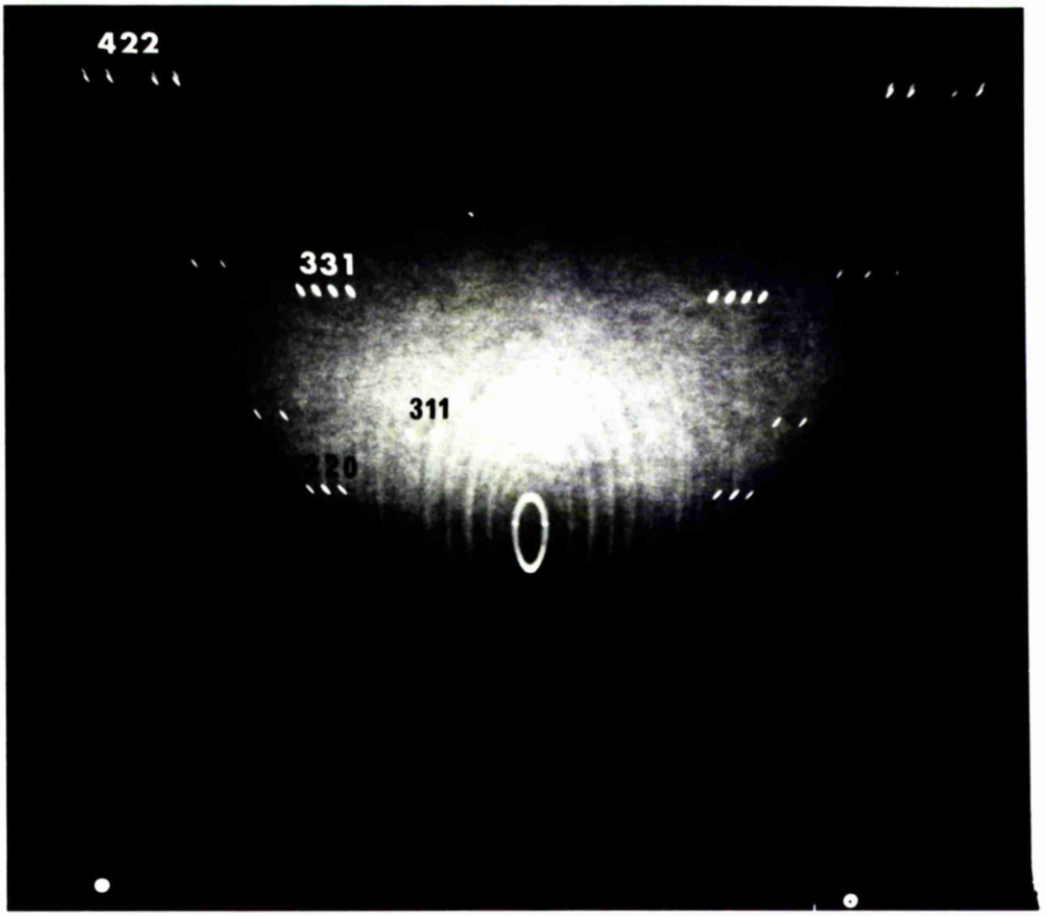

FIG. 4.20 : Texture camera pattern from a Zn (neutral) doped InP film.

Zn atom concentration in the film = 3×10^{20} cm^{-3}.

FIG.4.21 : Electron channelling micrograph from a Zn doped InP film.

Zn atom concentration in the film = 3×10^{20} cm^{-3}

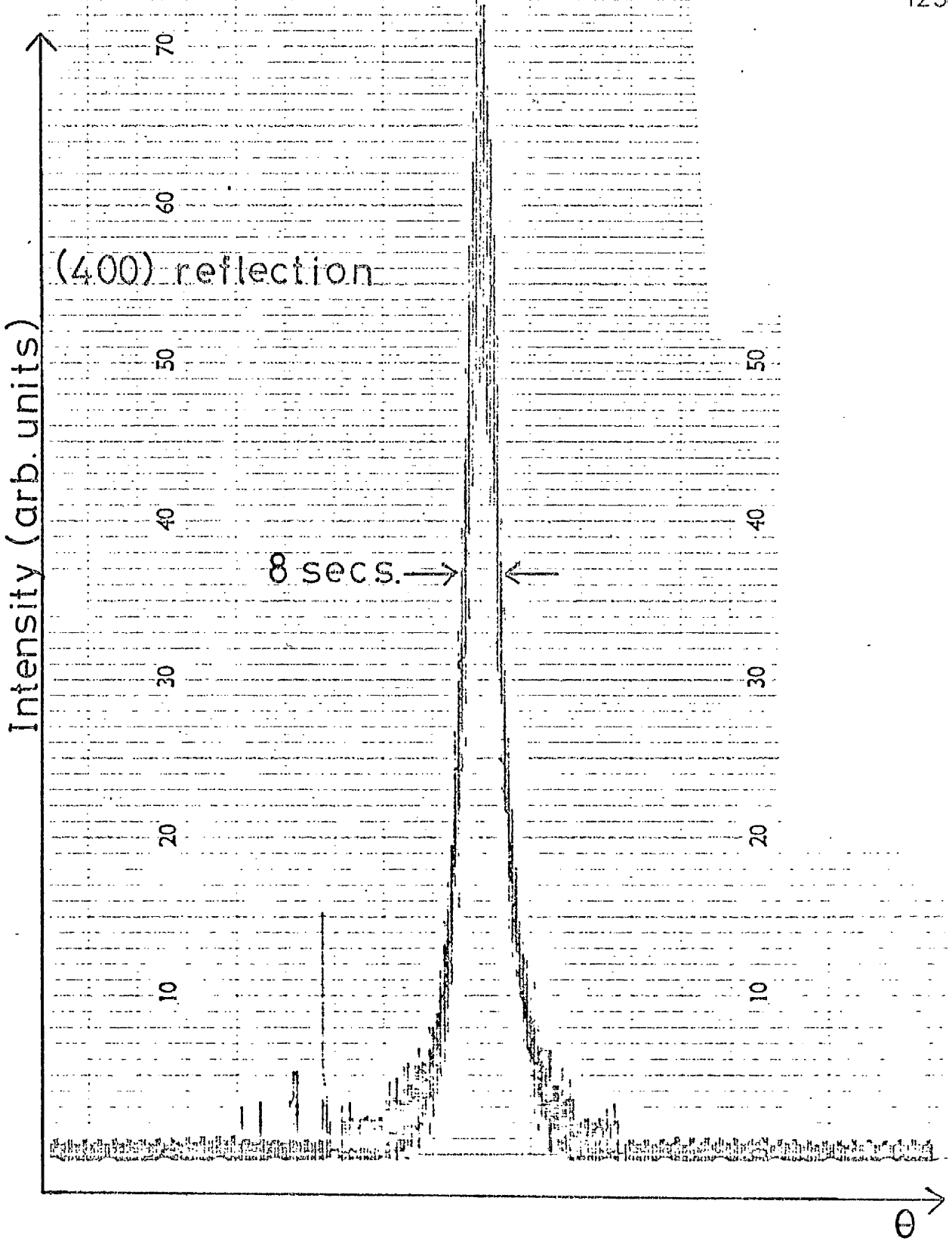

FIG.4.22 : Double crystal diffractometry trace from a Zn doped film.

Zn atom concentration = 3×10^{20} cm^{-}

since no apparent change in compensation was detected (which would indicate the presence of acceptors), relative to unintentionally doped material (see chapter 3) even with a Zn atom concentration within the film as high as 4×10^{20} cm^{-3}.

4.8 Discussion of Results

In contrast to the expected result neutral Zn has been shown to have a near unity sticking coefficient on (100) InP grown by MBE at substrate temperatures around $360^{o}C$ up to concentrations of $\sim 10^{19}$ cm^{-3}. With higher Zn fluxes the Zn atom concentration in the layers tend to an apparent saturation level of $\sim 6 \times 10^{20}$ cm^{-3}. It is possible that 6×10^{20} cm^{-3} represents the solid solubility limit of Zn in InP grown under non-equilibrium MBE growth conditions with excess Zn being re-evaporated at high Zn flux levels ($> 3 \times 10^{11}$ cm^{-2} s^{-1}). Astles et al [4.8] have reported a solid solubility limit of $\sim 3 \times 10^{18}$ cm^{-3} for Zn in InP grown under the thermodynamic equilibrium conditions of LPE. This result reinforces the assumption that the kinetic processes controlling crystal growth in MBE are far from those consistent with thermodynamic equilibrium being reached (see chapter 2).

Zn atom concentrations as high as 4×10^{20} cm^{-3} have been achieved in MBE grown InP with no apparent degradation of either the surface morphology or crystal structure of the layers as indicated by scanning electron microscopy

and X-ray texture camera analyses, respectively. The double crystal diffractometry analysis (see section 4.7.2) provides further evidence to suggest that heavily Zn-doped layers (> 10^{20} cm^{-3}) are strain-free single crystals. Casey [4.9] has reported that a double crystal diffractometry study of bulk GaAs heavily doped with Zn failed to reveal any evidence for lattice strain induced by the high Zn impurity concentrations ($\sim 10^{20}$ cm^{-3}). In marked contrast, Sullivan [3.2] has recently shown from a Sn doping study of InP grown by MBE that the InP lattice is distorted by twins as a consequence of Sn concentrations in the material, deduced from Hall measurements, in excess of $\sim 5 \times 10^{18}$ cm^{-3}. Sullivan [3.2] postulates that at high Sn doping levels a proportion of the Sn is incorporated into interstitial sites causing stacking faults or micro-twins.

In as-grown MBE Zn-InP less than one incorporated Zn atom in 10^3 is judged to be electrically active with no evidence having been found to suggest the presence of an appreciable amount of Zn occupying substitutional sites. A large discrepancy between the concentrations of holes and Zn atoms in Zn-diffused InP has been reported by several authors including Kundukhov et al [4.10] and Hooper and Tuck [4.11]. Hooper and Tuck [4.11] have found surface hole concentrations as low as $\sim 5 \times 10^{17}$ cm^{-3} obtained by Hall measurements while the Zn atom concentration at the surface was found using a radiotracer technique (active Zn^{65} being diffused) to be 2×10^{20} cm^{-3}.

In an attempt to account for the inequality found in Zn-diffused InP between the number of electrically active carriers and the total number of indiffused Zn atoms Tuck and Hooper [4.12] have proposed a model in which most of the Zn occurs in the form of the complex $V_P Zn_{In} V_p$ with a small proportion of Zn atoms also occupying substitution and interstitial sites. (V_P = a vacant P site and Zn_{In} = Zn on an In site). Zn precipitation in heavily Zn-doped material could also contribute to a reduction in the free carrier concentration. Mahajan et al [4.13] have observed fine precipitates in highly Zn-doped bulk-grown InP using transmission electron microscopy.

Mg-doped GaAs grown by MBE also exhibits an inequality between impurity atom and free carrier concentrations. Joyce and Foxon [4.14] found that Mg has a unity sticking coefficient on GaAs by atomic absorption spectrometry whereas earlier Cho and Panish [4.15] deduced a sticking coefficient of $\sim 10^{-5}$ from electrical measurements on GaAs films grown in the presence of a Mg flux. These results indicate that Mg is incorporated chemically into GaAs with a unity sticking coefficient but only one incident Mg atom in 10^5 is electrically active.

It is postulated that most of the Zn in Zn doped MBE grown InP is tied up in some form of complex such as that proposed by Tuck and Hooper [4.12] to account for the large carrier/atom inequality in Zn-diffused InP thus rendering

the Zn content electrically in-active. Clearly, however, there is insufficient data to allow a model to be proposed to account for the carrier/atom inequality found in MBE grown Zn doped InP. An extended investigation would be required involving the measurement of the carrier/atom ratio as a function of both the growth stoichiometry and substrate temperature in order to obtain a greater appreciation of the mechanism involved.

CHAPTER 5.

CHAPTER 5

BERYLLIUM DOPING OF InP BY MBE

5.1 Introduction

Ilegems [4.2] has reported that Be behaves as an ideal p-type dopant in GaAs and $Al_xGa_{1-x}As$ grown by MBE, the Be doping level (acceptor concentration) in epitaxial films being easily controlled by varying the Be oven temperature. Be doping levels up to the mid-10^{19} cm^{-3} range have been achieved in both GaAs and $Al_xGa_{1-x}As$ [4.2] with surface morphologies remaining comparable to those obtained in unintentionally doped films. Furthermore, the acceptor concentration in GaAs films grown at a substrate temperature of $\sim 600^{o}C$ has been found to be independent of growth stoichiometry (As rich or Ga rich) [4.2] indicating that Be is incorporated as a simple substitutional acceptor on Ga sites. More recently, Ploog et al [1.4] have reported using Be as the p-type dopant in their "nipi" GaAs crystals grown by MBE (see section 1.1).

Since, as discussed in chapter 2, the general MBE growth mechanism appears to be similar for most III-V compounds it is not unreasonable to expect Be to be incorporated as an acceptor impurity in InP grown by MBE. The objective of the work to be described in the following sections was to investigate the incorporation behaviour of Be in InP grown by MBE with a view to producing p-type InP epitaxial films.

5.2 Experimental Arrangement and Observations

In order to facilitate a Be doping study a separate Knudsen oven containing Be was incorporated into the MBE growth chamber; the Be doping arrangement is shown schematically in Fig. 5.1. The Knudsen oven design was identical to that described in section 3.3 and therefore requires no further comment. Despite being the purest material available [§] the Be source material used in this work contained the following impurities: Cu(20ppm), Al(20ppm), Fe(70ppm),Si(20ppm),Zn(100ppm) and Pb,Mg,Mn,Mo,Cr < 10ppm.

Prior to commencing the doping study the V.G. Q8 quadrupole mass spectrometer was used to observe the species effusing from the Be oven. Figs. 5.2(a) and 5.2(b) show the mass spectra recorded with the Be oven shutter in the closed and open positions, respectively, while the oven temperature was maintained at 990°C. In addition to the residual gases detected with the shutter closed (Fig. 5.2(a)) a small signal at atomic mass number 9 was observed with the shutter in the open position (Fig. 5.2(b)), indicating the presence of Be in the mass spectrum. From the Knudsen equation (equation 2.9) the theoretical Be flux level, J_{Be}, at an oven temperature of 990°C is only

§ The Be was supplied by C.T. Foxon of P.R.L. (Redhill, Surrey).

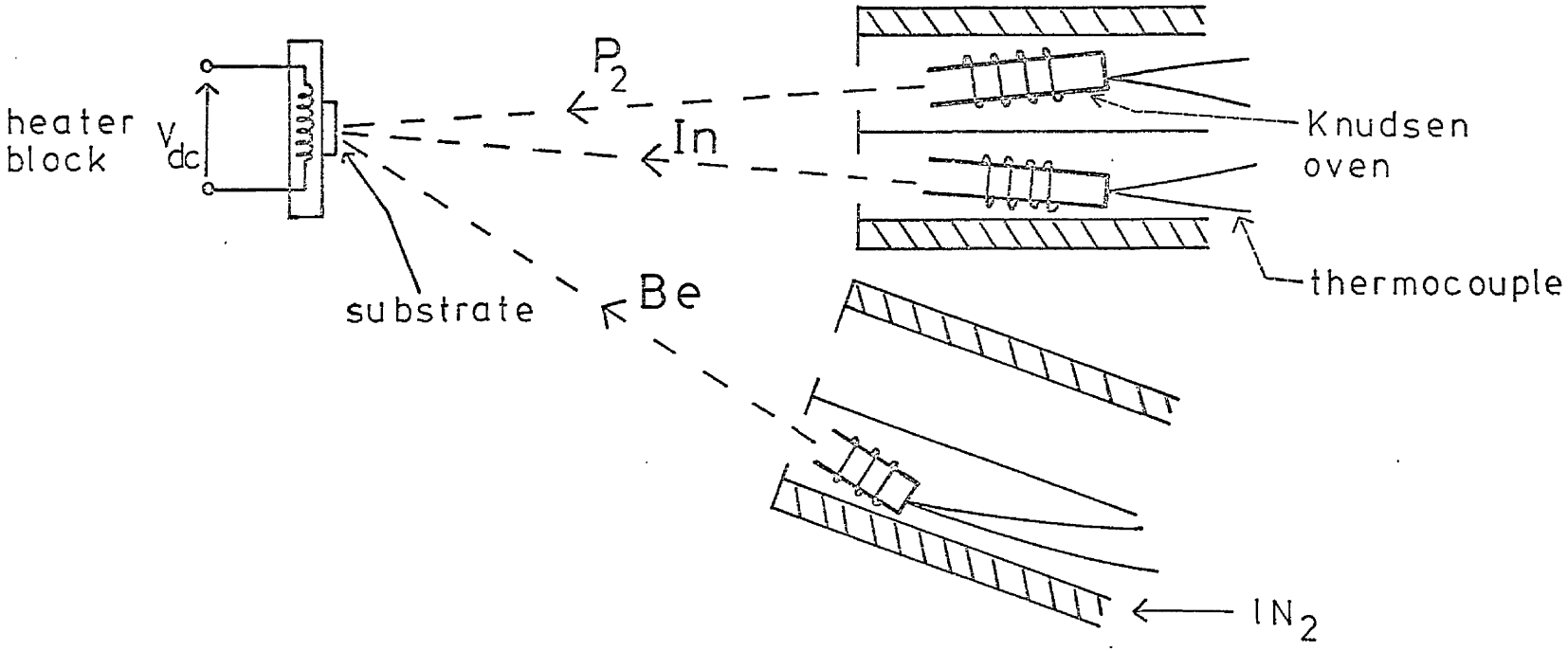

FIG. 5.1 : Schematic of Be doping arrangement.

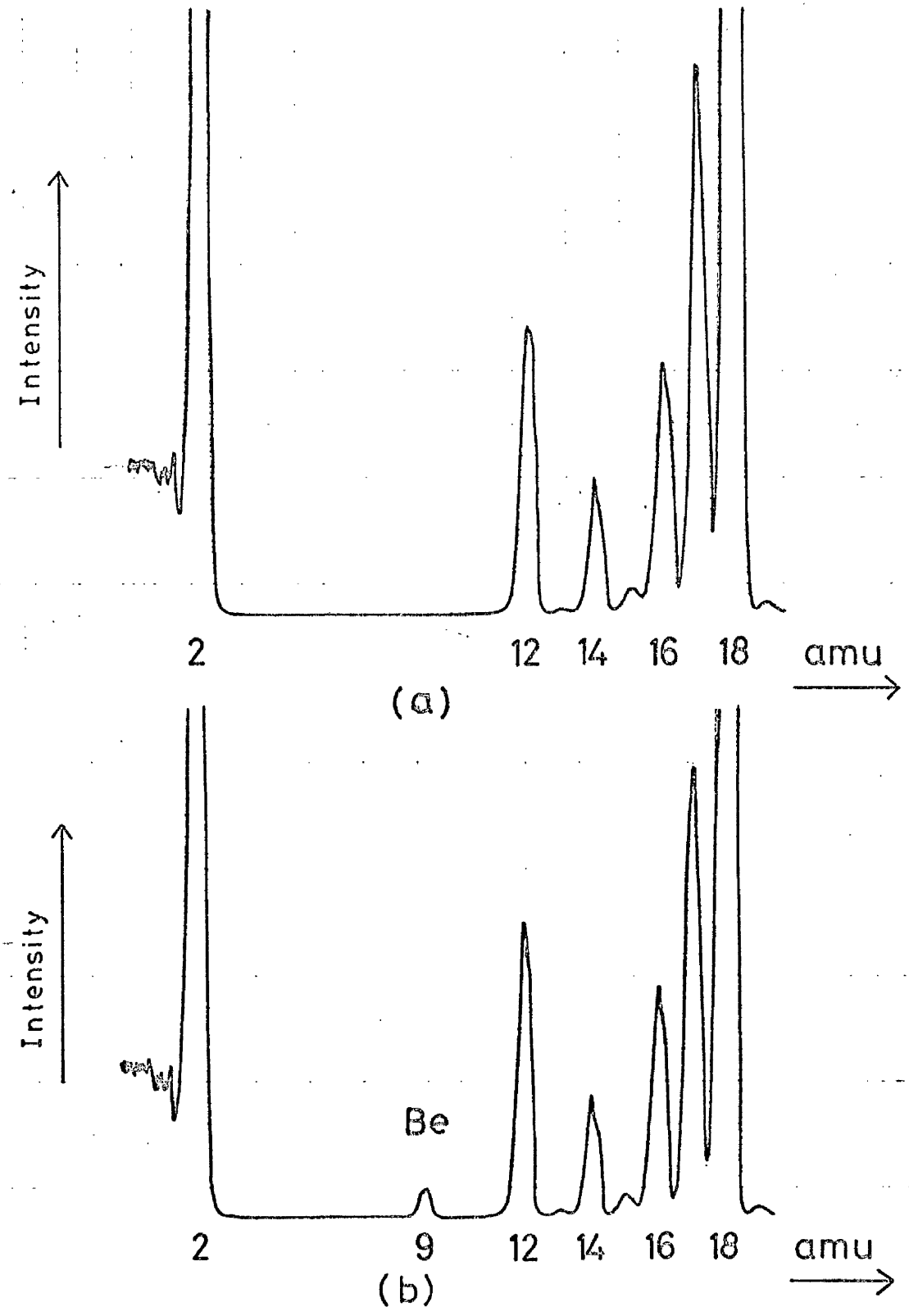

FIG. 5.2 : Mass spectra with Be oven at 990°C.

(a) shutter closed (b) shutter open.

$2 \times 10^{13} cm^{-2} s^{-1}$ (c.f. $3 \times 10^{14} cm^{-2} s^{-1}$ for In at 870°C, for example). It can be concluded from Figs. 5.2(a) and 5.2(b) that the Be evaporated as a collimated atomic beam.

5.3 Growth and Characterisation of Be Doped InP Films

1μm thick Be doped InP films were grown onto Fe doped semi-insulating substrates cut 2° off the [100] direction at a substrate temperature of 360°C with the Be oven temperature varied over a range from 720°C to 850°C. The basic substrate preparation techniques, both ex-vacuo and in-vacuo, and growth procedures outlined in chapter 3 were employed.

5.3.1 Chemical Analysis of Films

Fig. 5.3 illustrates a plot of Be atom concentration in the films versus the Be oven temperature during film growth. The experimental points shown in the plot were obtained by atomic absorption spectrometry analysis while the solid line represents the theoretical Be concentration as calculated using the Knudsen equation (equation 2.9) and assuming a unity sticking coefficient for the Be atoms. As can be seen from the figure the experimental points lie very close to the theoretical curve, indicating that the Be sticking coefficient, S_{Be}, is indeed unity or, in other words, the incorporation rate of Be atoms is simply equal to their arrival rate at the substrate. 20°C was added to each of the monitored Be oven temperature readings in

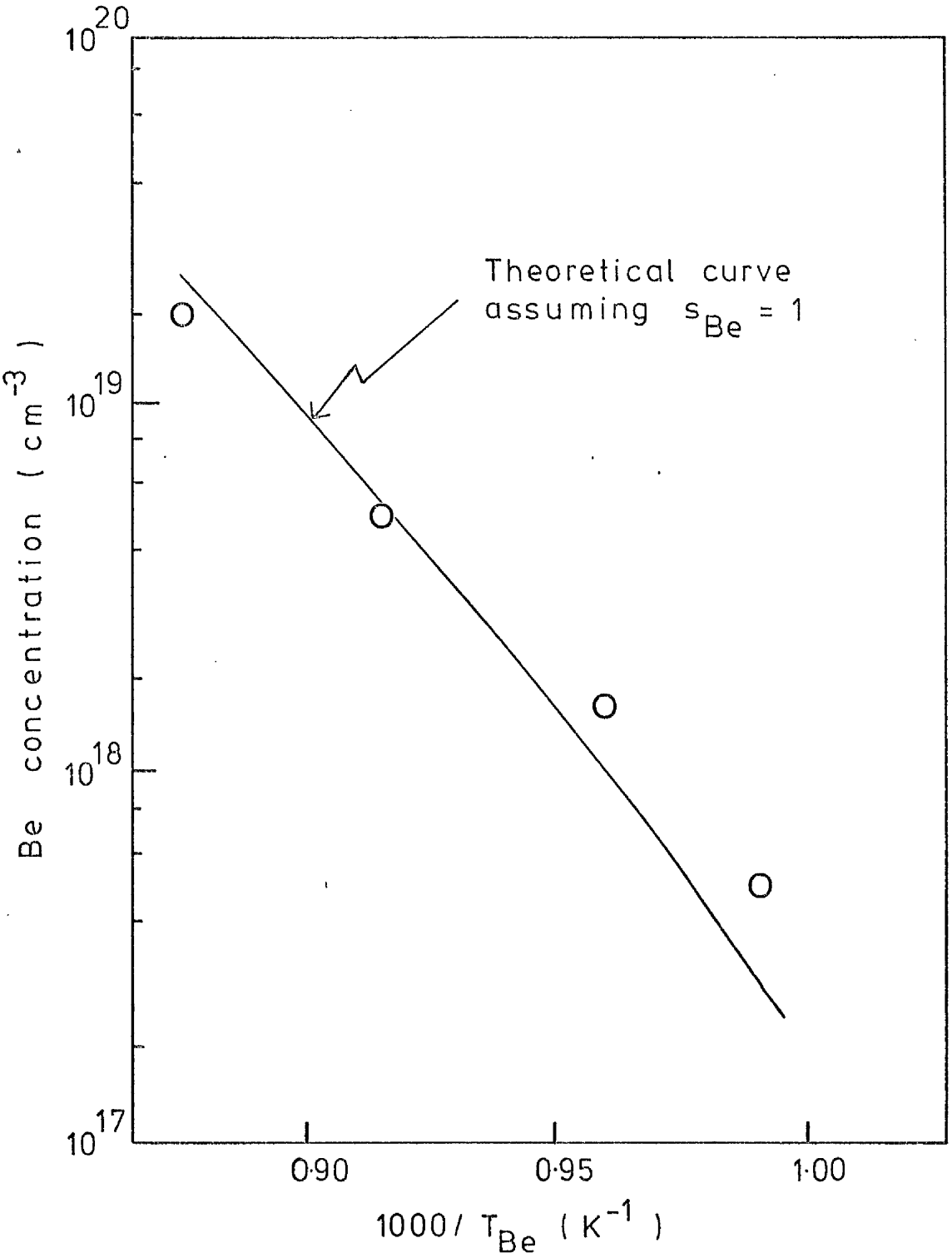

FIG. 5.3 : Be atom concentration in InP films versus Be oven temperature.

order to obtain the experimental points shown in Fig. 5.3 since, as discussed in section 3.7.1, the actual oven charge temperature is $\sim 20^{o}C$ higher than the monitored oven temperature for the Knudsen oven design employed in these experiments.

5.3.2 Microscopic and Crystallographic Assessment of Films

The surface of the complete range of Be doped films appeared mirror-like and featureless to the naked-eye while the surface morphology observed using Nomarski phase contrast microscopy remained identical to that of unintentionally doped InP films even for films having a Be atom concentration > 10^{19} cm^{-3}. Hence, surface roughening at high Be doping levels due to surface segregation was not apparent. The surface of Be doped films also appeared featureless at high magnification; Fig. 5.4 shows an SEM micrograph (x 10K mag) of the surface of a film having a Be atom concentration of 2 x $10^{19}cm^{-3}$. (The particle to the top left hand corner of the micrograph was located to aid focussing).

Texture camera analysis [A.1] was used to assess the crystallographic quality of the Be doped InP films. The complete range of Be doped films with Be concentrations ranging from 5 x $10^{17}cm^{-3}$ to 2 x $10^{19}cm^{-3}$ were shown to be twin-free single crystal providing texture camera diffraction patterns such as that illustrated in Fig. 5.5 which was recorded from a film having a Be atom concentration of 2 x $10^{19}cm^{-3}$.

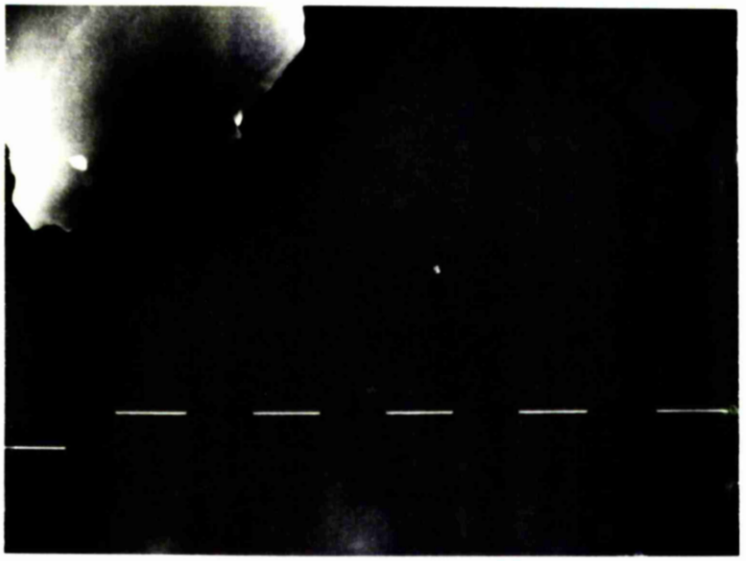

1μm markers

X 10K MAG.

FIG. 5.4 : SEM micrograph of surface of a Be doped InP film.

Be atom concentration in the film = 2×10^{19} cm^{-3}.

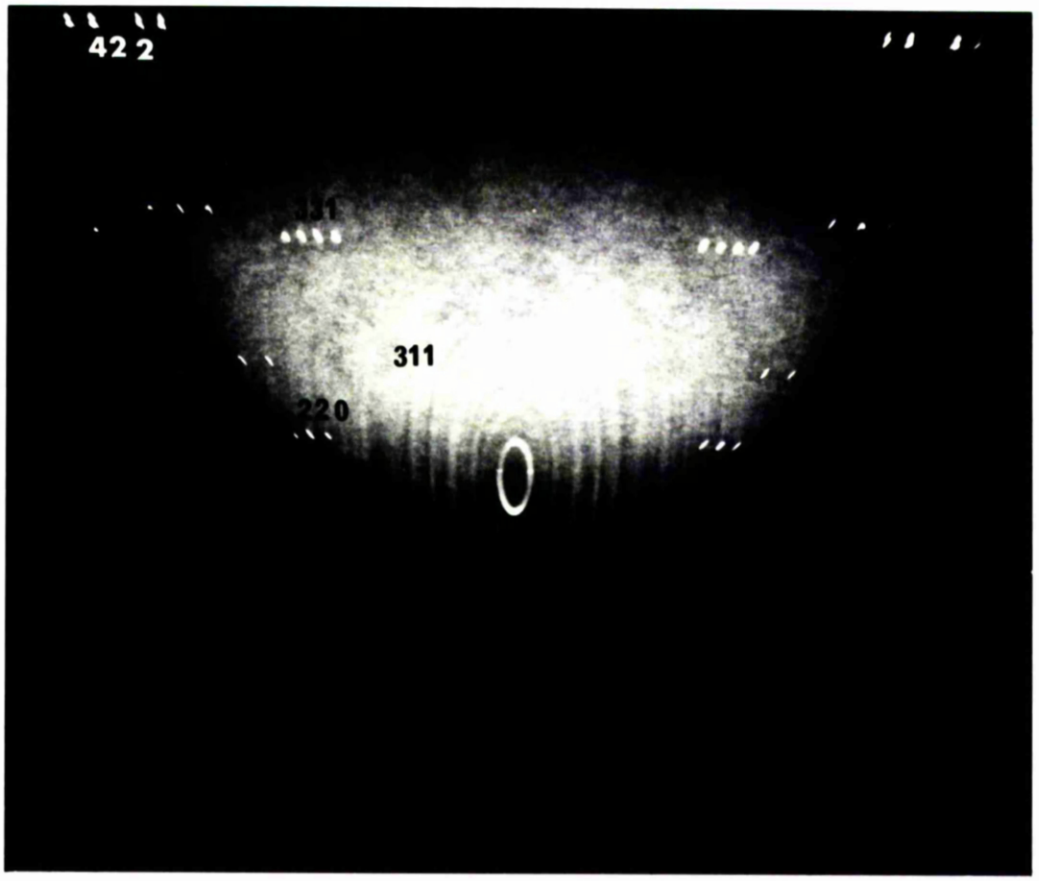

FIG. 5.5 : Texture camera pattern from a Be doped InP film.

Be atom concentration in the film = 2×10^{19} cm^{-3}.

5.3.3 Electrical Characterisation of Films

A great deal of difficulty was experienced in trying to make good electrical contact to the Be doped films which was the first indication that the Be was having some effect on the electrical properties of the films. Aluminium contacts which were normally "ohmic" on unintentionally doped (and Zn doped) InP films exhibited rectifying characteristics. Zn/Au alloyed contacts were attempted which are normally "ohmic" on p-type InP but these contacts were generally unsuccessful on the Be doped films. Only one Be doped film having a Be atom concentration of $2 \times 10^{19} cm^{-3}$ was successfully contacted using Zn/Au alloyed contacts and Hall-effect measurements on this film showed the layer to be n-type with $N_D - N_A$ in the low-$10^{15} cm^{-3}$ range, indicating the film to be highly compensated.

5.4 Discussion of Results

It has been established that Be has a near unity sticking coefficient on (100) InP grown by MBE at substrate temperatures around $360^{o}C$, the incorporation rate of Be atoms in growing InP films being approximately equal to their arrival rate at the substrate. Thus, Be doping levels can be readily controlled by setting the Be oven temperature to provide the required Be flux level. Since Be doped films were shown to be twin-free single crystal by texture camera analysis over the complete range of Be doping levels, ie 5×10^{17}-$2 \times 10^{19} cm^{-3}$, it can be concluded

that Be is easily accommodated in the InP lattice even at doping levels > $10^{19}cm^{-3}$ (c.f. Sn in MBE grown InP[3.2]). Moreover, surface roughening due to Be segregation at high doping levels was not apparent from Nomarski phase contrast microscopy observations, the surface morphology of highly doped films remaining identical to that of unintentionally doped films. Characterisation of the electrical properties of Be doped InP grown by MBE was severely hindered due to problems encountered in making good electrical contact to the films. Since evaporated Al contacts which were "ohmic" on unintentionally doped films exhibited rectifying characteristics on Be doped films it is concluded that the Be content was at least partially activated and consequently altered the electrical properties of the films. The one successful Hall-effect measurement which was made on a highly doped film indicated that the material was still n-type but highly compensated relative to unintentionally doped material which again suggests a degree of activation of the Be content.

CHAPTER 6.

CHAPTER 6

DEEP LEVEL TRANSIENT SPECTROSCOPY

6.1 Introduction

Deep levels in the energy gap of a semiconductor are normally considered as being secondary to shallow donor and acceptor levels. Impurities responsible for shallow levels typically have concentrations ranging from 10^{16} cm^{-3} to 10^{19} cm^{-3} whereas deep levels are normally a consequence of unintentionally incorporated impurities or lattice defects, such as vacancies, interstitials and vacancy-complexes, having typical concentrations in the range 10^{12} cm^{-3} - 10^{15} cm^{-3}. Energy levels more than $\sim$ 0.1 eV removed from the band edges can be thought of as deep.

The importance of deep levels in practice lies with their role as generation-recombination centres or carrier traps. As G-R centres they can be responsible for a sharp reduction in minority carrier lifetime and diffusion length which may, for example, limit bipolar transistor performance. They give rise to excess leakage currents in reverse-biased p-n junctions, dark current in IR detectors or photo-cathodes and noise in Gunn diodes. One of their more serious manifestations is as non-radiative recombination centres in light-emitting diodes or lasers, resulting in reduced radiative efficiency.

A convenient and powerful technique for characterising deep level traps in semiconductor materials involves the measurement of the capacitance of a p-n junction or

Schottky barrier diode. The so-called capacitance transient technique which was first used by Williams [6.1] provides a sensitive measure of the charge state of a deep trap. Information about a deep level in the depletion region of a p-n junction or Schottky barrier diode can be obtained by observing the capacitance transient associated with the return to thermal equilibrium of the occupation of the level following an initial non-equilibrium condition. The time constant of the transient can be measured as a function of temperature and the activation energy of the level obtained. The initial magnitude of the transient is related to the trap concentration.

A highly sophisticated form of the capacitance transient technique was developed by Lang [6.2] and is known as deep level transient spectroscopy (DLTS). The essential feature of DLTS is the ability to set an emission-rate window such that the measurement apparatus only responds when it sees a capacitance transient with a rate within this window. The DLTS technique is able to distinguish between majority and minority carrier traps and provides information about the concentrations, energy levels and capture rates for these traps. In addition the technique is spectroscopic in nature in the sense that the signals due to different traps can be resolved from one another and are reproducible in position when plotted against a single variable, namely, the sample temperature. DLTS is also capable of

measuring traps over a wide range of depths, including both radiative and non-radiative centres.

As is the case for doping studies of III-V semiconductors grown by MBE it is GaAs which has been the most extensively studied material with regard to deep traps. Fifteen different electron traps with thermal activation energies to the conduction band ranging from 0.83 eV to 0.15 eV have been characterised in VPE, MBE and bulk-grown GaAs from DLTS experiments. These traps have been catalogued by Martin et al [6.3]. In contrast no electron traps have been detected in unintentionally doped LPE grown material. One of the striking results of the work on GaAs is that many different electron traps are found in VPE, MBE and bulk-grown materials but only a few of them are common to the different methods of crystal growth.

It has also been shown in the case of epitaxial GaAs that growth parameters such as substrate growth temperature and surface stoichiometry during growth, can have a profound effect on the concentration of deep traps. For example, Stall et al [6.4] have reported an increase in the concentrations of three traps, termed M1, M2 and M3, in MBE grown GaAs as the growth temperature is lowered below $\sim 500^{o}C$, the normal growth temperature being $\sim 650^{o}C$. Trap M3, for instance, increases in concentration from 10^{12} cm^{-3} to 2×10^{15} cm^{-3} as the substrate growth temperature is lowered from $550^{o}C$ to $430^{o}C$.

In contrast to the extensive work on GaAs the study of deep traps in InP is only in its infancy. Several deep electron traps have already been detected, however, in VPE and bulk-grown InP by DLTS as reported by White et al [6.5] and Wada et al [6.6]. Only one of the traps detected in InP has been assigned to a particular impurity or lattice defect. Recently, Bremond et al [6.7] have shown that a commonly found trap in both VPE and bulk-grown InP having a thermal activation energy of 0.63 eV to the conduction band is due to a residual Fe impurity. To date, however, no results have appeared in the literature on deep trap studies of InP grown by the MBE technique.

The aim of the work to be described in chapter 6 was to construct a DLTS system in order to facilitate the detection and possible identification of deep traps in MBE grown InP. A principle objective behind this work was to provide feedback information to improve the quality of InP grown by MBE.

6.2 Principles of DLTS

Before beginning a discussion on the principles of DLTS an explanation is required concerning the two types of trapping centres, namely, majority carrier and minority carrier traps. In the case of n-type material majority carrier traps are termed electron traps whereas minority carrier traps are termed hole traps. The converse terminology applies to p-type material. Thus, when

Schottky-barriers are employed on n-type material only majority-carrier or electron traps can be observed since Schottky-barrier diodes are majority-carrier devices. Minority-carrier or hole traps, however, can be detected using p^+-n junctions since holes can be injected into the n-type material by forward biasing the p^+-n junction.

Consider a Schottky-barrier or p^+-n junction containing a shallow level with nett donor concentration N_D-N_A and a deep level electron trap at an energy E_T below the conduction band having a concentration N_T. A schematic band diagram of such a junction under reverse-bias is shown in Fig. 6.1. In the DLTS technique the diode is repetitively pulsed either from a reverse-bias level to zero-bias (for the case of majority-carrier traps) or pulsed into forward-bias (for the case of minority-carrier traps in p^+-n junctions). The diode transient capacitance responses for both these cases are shown in Fig. 6.2.

As mentioned in the introduction the essential feature of DLTS is the ability to set an emission-rate window such that the measurement apparatus only responds when it sees a capacitance transient with a rate within this window. Thus, if the emission-rate (or the reciprocal of the capacitance transient time constant) is varied by varying the sample temperature, the instrument will show a response peak at the temperature when the trap emission-rate is within the window. The DLTS apparatus described in detail in section 6.3 makes

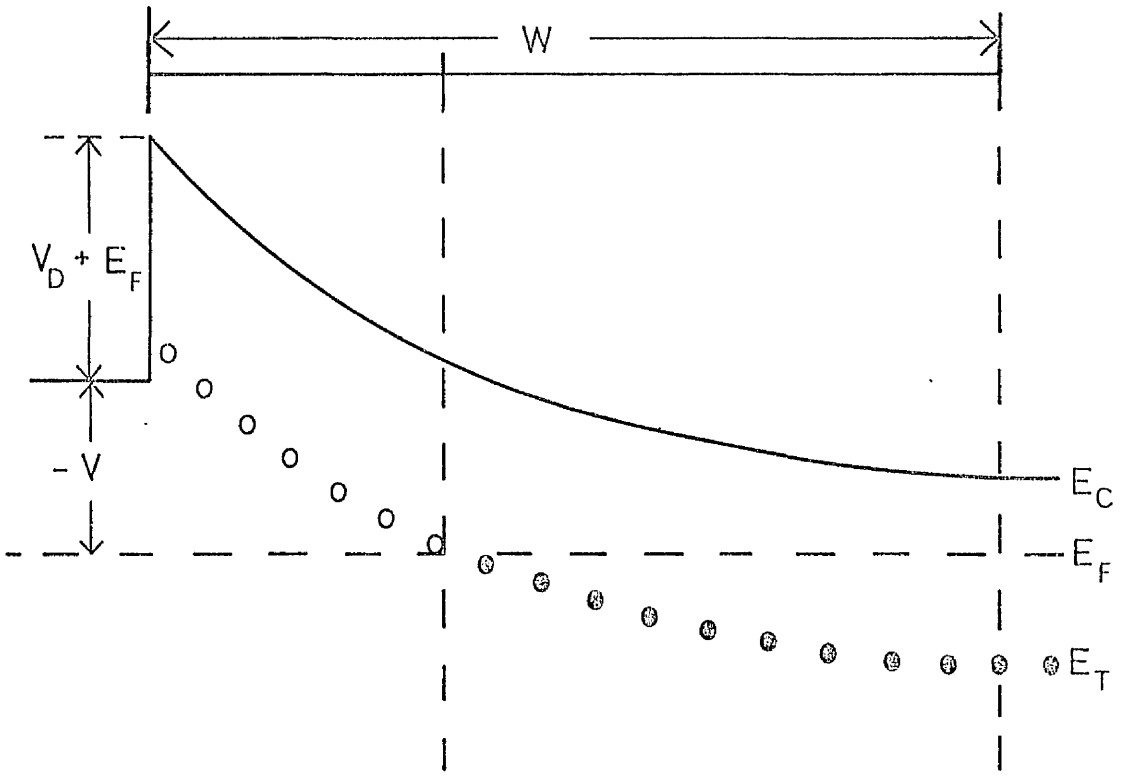

FIG. 6.1 : Energy band diagram for a reverse-biased Schottky barrier or p^+-n junction indicating the states of the traps in the depletion region W : o traps empty and • traps filled with electrons.

V = bias voltage

V_D = diffusion voltage

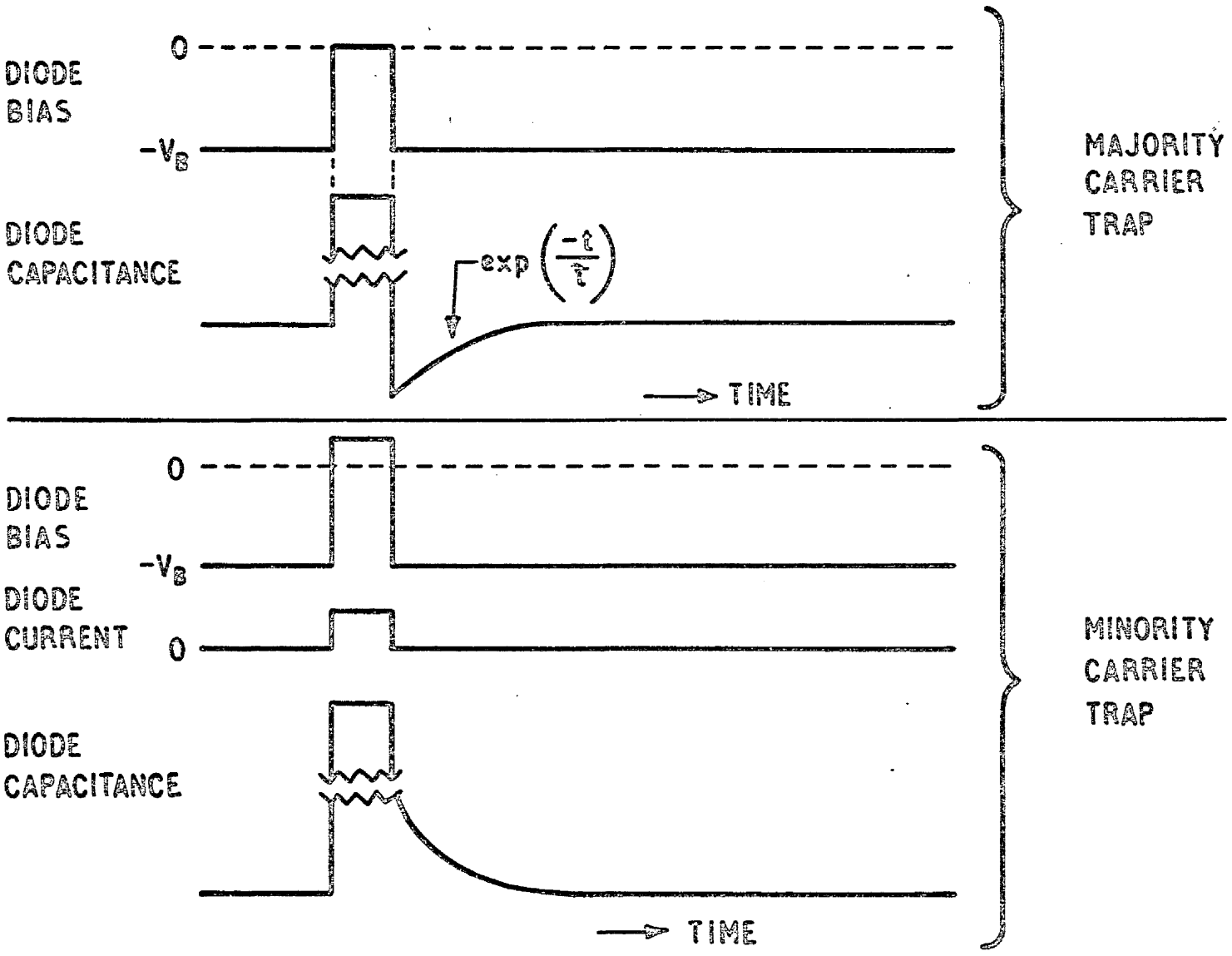

FIG. 6.2 : TYPICAL TIME DEPENDENCES INVOLVED IN PULSED BIAS CAPACITANCE TRANSIENTS FOR MAJORITY AND MINORITY CARRIER TRAPS

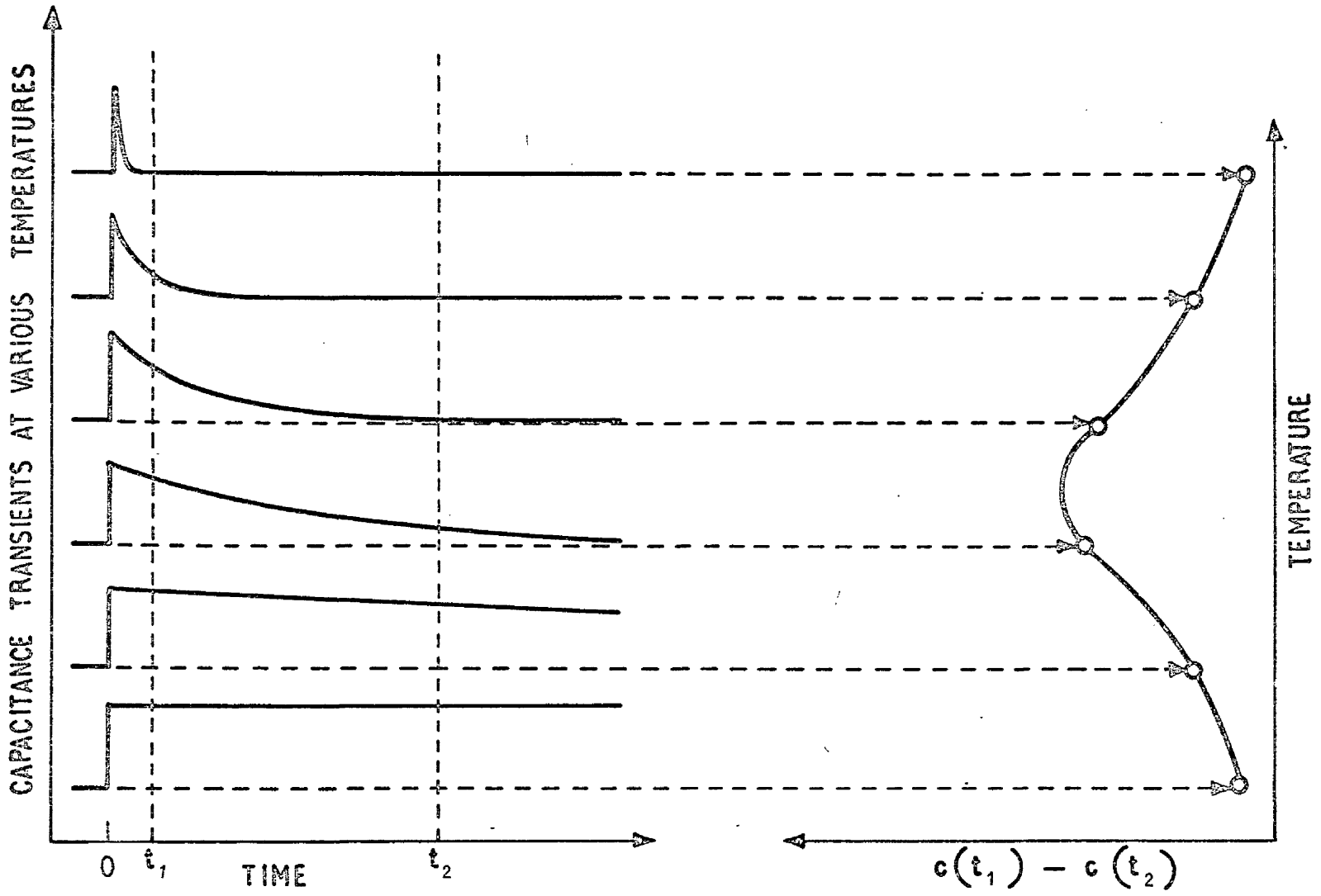

RIGHT-HAND SIDE SHOWS D.L.T.S. SIGNAL RESULTING FROM USING THE SIGNAL ANALYSER TO DISPLAY THE DIFFERENCE BETWEEN THE CAPACITANCE AT TIMES t_1 and t_2 AS A FUNCTION of TEMPERATURE

FIG. 6.3

use of two sample-and-hold circuits triggered by a double pulse generator which allows the emission-rate window to be precisely determined. The outputs of the sample-and-hold circuits are coupled to a difference amplifier (see section 6.3) which outputs a signal proportional to the difference in the capacitance readings ΔC measured at two times, t_1 and t_2 on the transient. The formation of a DLTS response peak is illustrated in Fig. 6.3.

A relationship can be derived between τ_{max}, the value of τ (the capacitance transient time constant) at the maximum value of $C(t_1) - C(t_2)$ (see Fig. 6.3) for a particular trap, and the two sampling times, t_1 and t_2. The quantity which has been loosely referred to as the 'rate window' is now defined to be τ_{max}^{-1}. Assuming the transient to be a pure exponential then $C(t_1) - C(t_2)$ is given by

$$C(t_1) - C(t_2) = \Delta C = \text{const.} \quad \exp(-t_1/\tau) - \exp(-t_2/\tau) \qquad (6.1)$$

Differentiating ΔC with respect to τ and equating $d(\Delta C)/d\tau$ to zero yields the result that ΔC is a maximum when

$$\tau_{max} = \frac{(t_2 - t_1)}{\ln(t_2/t_1)} \qquad (6.2)$$

From the principle of detailed balance the electron thermal emission from a trap can be written as (6.2)

$$\frac{1}{\tau} = \sigma \bar{v}_{th} N_c g \cdot \exp\left[-\frac{\Delta E}{kT}\right] \qquad (6.3)$$

for the case of electrons emitting to the conduction band with a thermal activation energy ΔE. The other terms in equation 3 are as follows;

$\overline{v}_{th}$ = mean thermal velocity of the electrons.

σ = capture cross-section of the trap.

N_c = density of states in the conduction band.

g = degeneracy of the trap level.

A similar expression holds for holes emitting to the valence band. N_c and $\overline{v}_{th}$ are both temperature dependent and are given by

$$N_c = 2\left[\frac{2\pi m_d kT}{h^2}\right]^{3/2} \tag{6.4}$$

$$\overline{v}_{th} = \left[\frac{3kT}{m_c}\right]^{1/2} \tag{6.5}$$

where m_d and m_c are the density of states mass and conductivity mass, respectively. Thus, the product $\overline{v}_{th} N_c$ may be written as

$$\overline{v}_{th} N_c = A.T^2 \tag{6.6}$$

where A is a constant term given by

$$A = 2\left[\frac{2\pi m_d k}{h^2}\right]^{3/2}\cdot\left[\frac{3k}{m_c}\right]^{1/2} \tag{6.7}$$

The emission time constant can therefore be corrected for the temperature dependence of the pre-factor in equation 3 and the detailed balance equation can be

written as

$$\frac{1}{\tau T^2} = (A\ \sigma\ g).\exp\left[-\frac{\Delta E}{kT}\right] \qquad (6.8)$$

assuming the trap capture cross-section σ to be independent of temperature.

Since the emission time constant τ_{max} corresponding to the maximum of a trap peak observed in a DLTS thermal scan is a precisely defined quantity given by equation 6.2 the detailed balance equation can be specifically written as

$$\frac{1}{\tau_{max}\ T_p^2} = (A\ \sigma\ g)\ .\ \exp\left[-\frac{\Delta E}{kT_p}\right] \qquad (6.9)$$

where, T_p = Temperature at which ΔC is a maximum.

An Arrhenius plot of ln (τT^2) versus $1/T$ therefore yields ΔE, the thermal activation energy of the trap, while the trap capture cross-section σ can subsequently be calculated using equation 6.9.

6.3 DLTS Measurement System

The DLTS apparatus is shown in Fig. 6.4 while the system is illustrated in block diagram form in Fig. 6.5. The functions of the various components of the DLTS measurement system are now described with reference to Fig. 6.5.

A diode is thermally scanned through a range from 77K to $\sim$ 400K by means of the variable temperature cryostat.

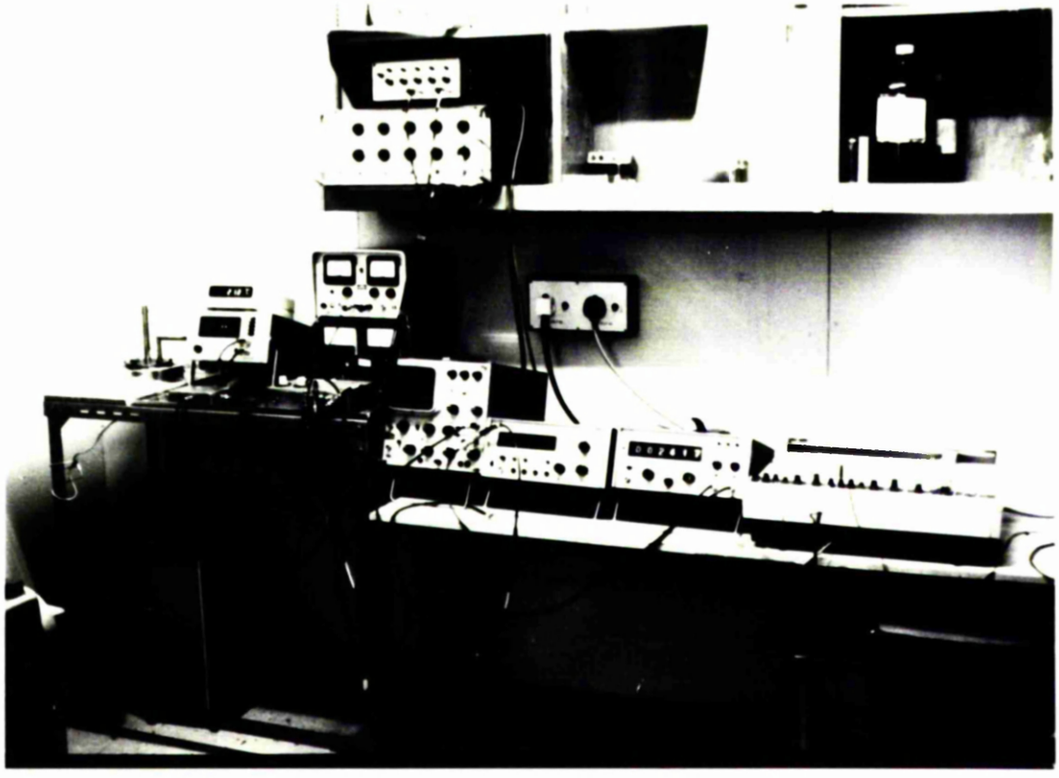

FIG.6.4 : Photograph of DLTS apparatus.

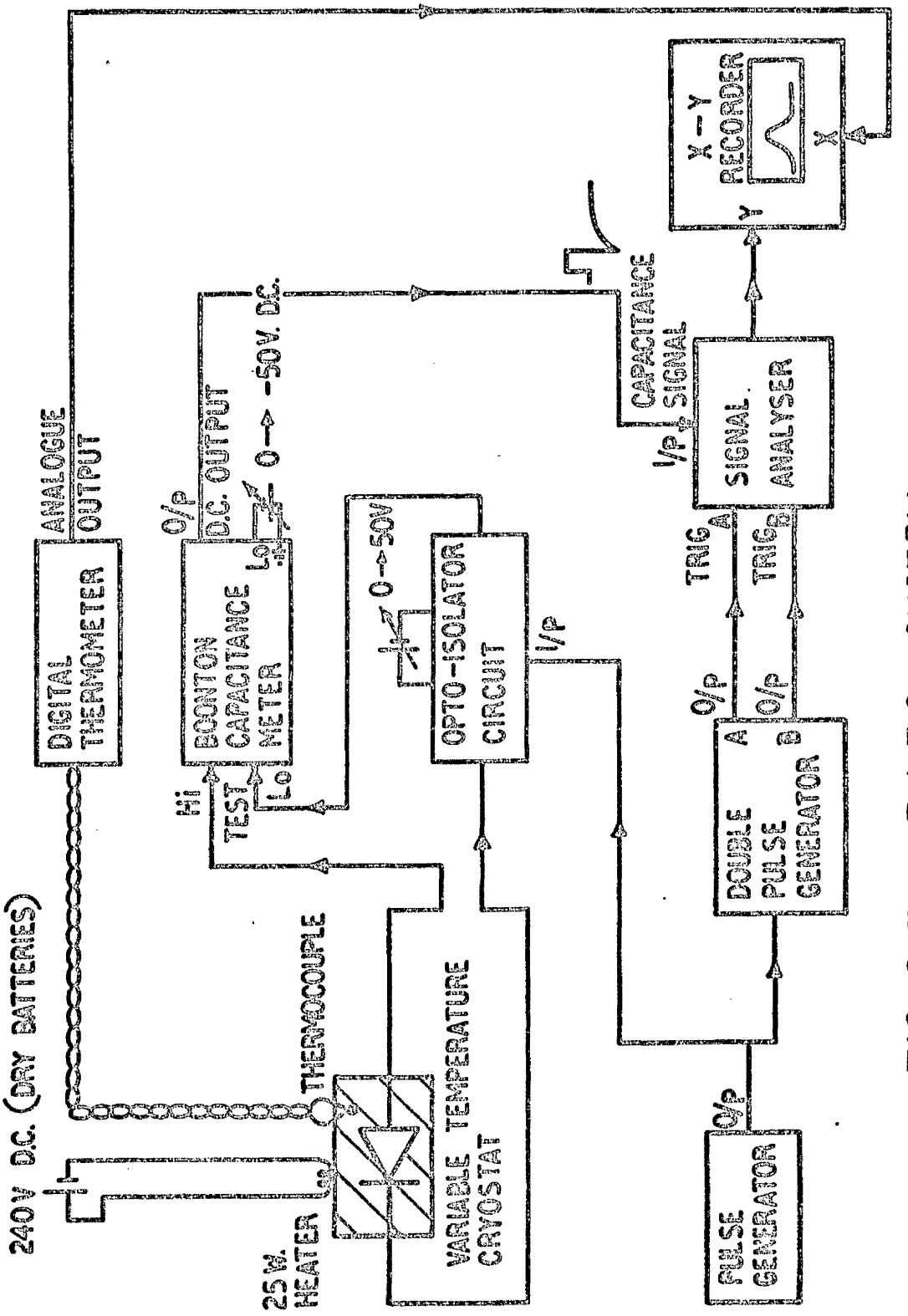

FIG. 6.5 : D.L.T.S. SYSTEM

The diode temperature is monitored by the digital thermometer, the analogue output of which is used to drive the X-movement of the X-Y recorder. The leading edge of a pulse from the single pulse generator is used to trigger both the opto-isolator circuit (shown in detail in Fig. 6.7) and the double pulse generator. With each triggering pulse the diode is switched from a steady-state reverse-bias level to zero-bias for the duration of the pulse. Hence, the capacitance meter monitors the diode capacitance which changes abruptly from a steady-state level, ie, the capacitance of the diode at a particular reverse-bias voltage, to a new level corresponding to the diode capacitance at zero-bias. If a deep trap is present the capacitance signal from the meter will be transient in nature as the diode capacitance returns to the steady-state level. The function of the double pulse generator is to provide two independent output pulses of pulse width $\sim$ 20 μs after specific time intervals from the leading edge of the triggering pulse from the single pulse generator. The two pulses are used to trigger sample-and-hold units contained in the signal analyser (see Fig. 6.6). This results in the capacitance transient being sampled at two predetermined points in time. The capacitance transient signal analyser shown in Fig. 6.6 which is a modified version of the circuit proposed by Guldberg [6.8] gives an output which is proportional to the difference in the capacitance readings at the two sampling times.

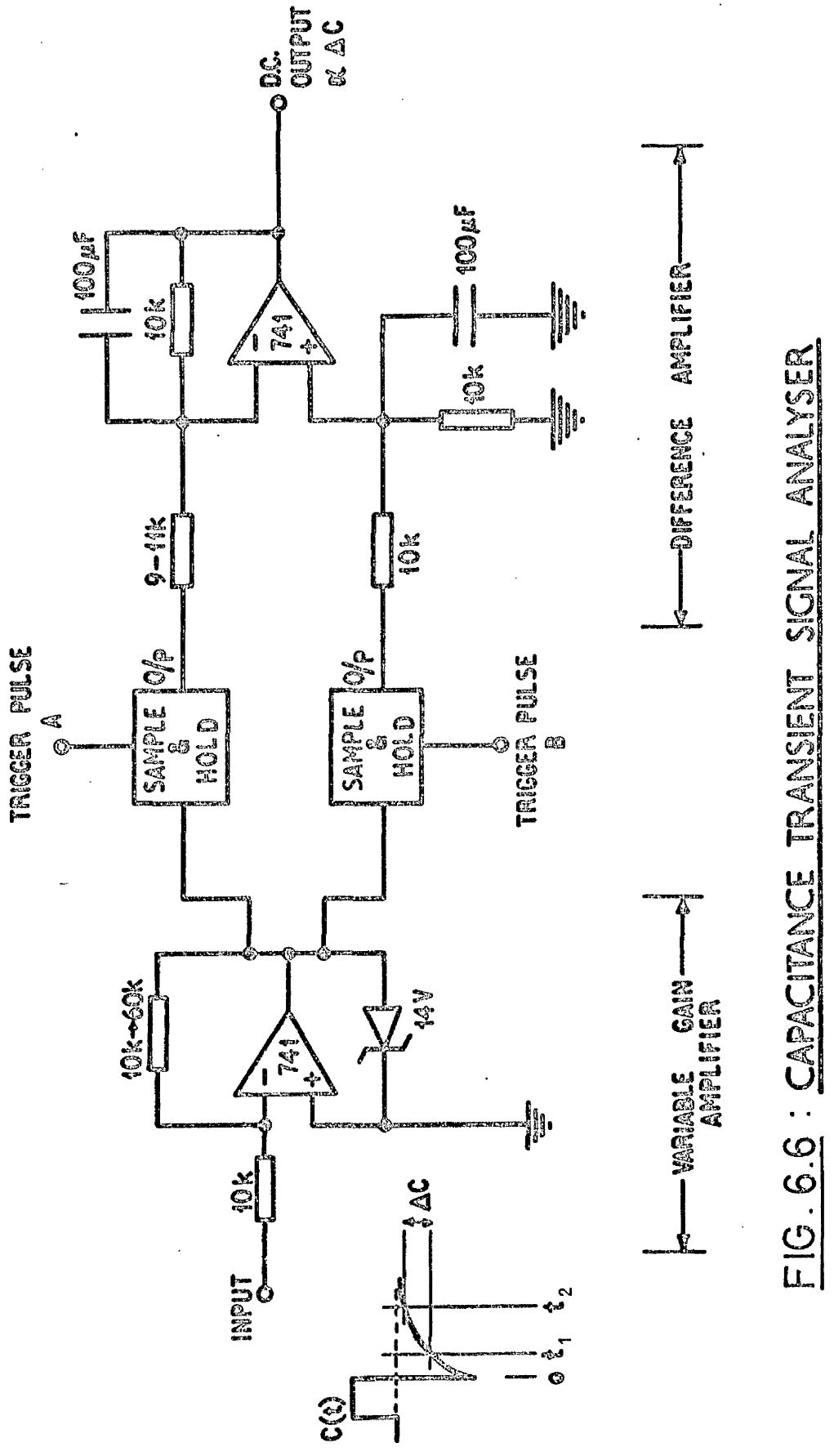

FIG. 6.6 : CAPACITANCE TRANSIENT SIGNAL ANALYSER

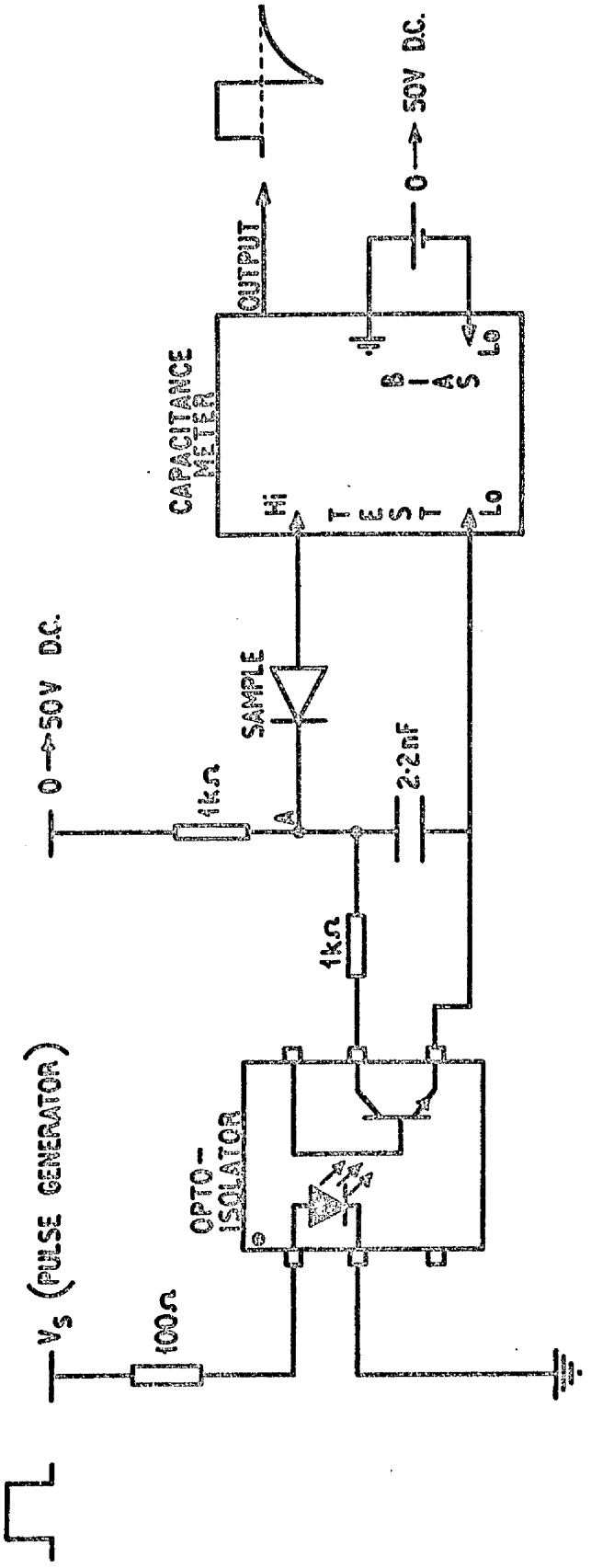

OPTO-ISOLATOR CIRCUIT
DIODE PULSING CIRCUIT / CAPACITANCE MEASUREMENT

FIG. 6.7

Since the capacitance meter requires that its test terminals be floating at all times a diode pulsing circuit was designed which employs an opto-isolator IC. The operation of the opto-isolator circuit which is shown in Fig. 6.7 is as follows: When the signal from the single pulse generator is LOW the L.E.D. is OFF and therefore the transistor is OFF. Thus, point A sits at +V volts and the diode sample is in reverse-bias. When the pulse is ON the transistor conducts and hence the 2.2nF capacitor can discharge through the 1kΩ resistor. Bias can be applied to the diode via. bias terminals at the rear of the capacitance meter and with bias applied as shown (note the polarity) point A drops to zero volts when both DC supplies are equal. Hence, for the duration of the pulse the diode is at zero bias. When the pulse goes LOW the diode is returned to the reverse-bias level. It should be noted here that with the arrangement shown in Fig. 6.7 diodes could not be forward-biased and therefore minority carrier traps were not observed in the experiments detailed in this chapter.

6.4 DLTS of GaAs Grown by VPE

Initial experiments were performed on VPE grown n-type GaAs layers supplied by D. Allen of the British Telecom Research Laboratories, Martlesham Heath. These experiments were designed essentially to calibrate the DLTS system using a material which is well characterised in terms of deep traps.

DLTS measurements were made on n-type GaAs (sulphur doped, $n \simeq 3 \times 10^{15}$ cm^{-3}) grown by VPE onto n^+-type substrates. Schottky diodes with a barrier height of $\sim$ 0.8 eV were formed by evaporating 500 μm diameter Ni dots onto the epitaxial layer surface (through a mechanical mask) while a AuGeNi eutectic was used to form an ohmic contact to the substrate. Diodes so formed were bonded onto TO5 headers (see section 6.5.1) with conducting epoxy, mounted in the variable temperature cryostat, and a copper-constantan thermocouple was spot-welded onto the header.

The GaAs Schottky diodes were pulsed from a reverse-bias level (typically 1 volt reverse-bias) to zero-bias at a 10Hz repetition rate and 5ms pulse duration, and thermally scanned from 77K to $\sim$ 400K.

6.4.1 Results

A typical DLTS spectrum obtained from VPE grown GaAs is shown in Fig. 6.8. The emission time constant τ_{max} was 6.49 ms resulting from sampling times, t_1 and t_2 of 3.26 ms and 11.36 ms, respectively.

The presence of a single deep electron trap is indicated from Fig. 6.8 with the DLTS spectrum peaking at T_p = 381K. No other deep traps were detected in the range 77K to 300K. Fig. 6.9 illustrates a set of DLTS spectra recorded for various settings of τ_{max}. In order to vary τ_{max} both t_1 and t_2 were changed; however, the ratio t_2/t_1 was kept constant. By employing the

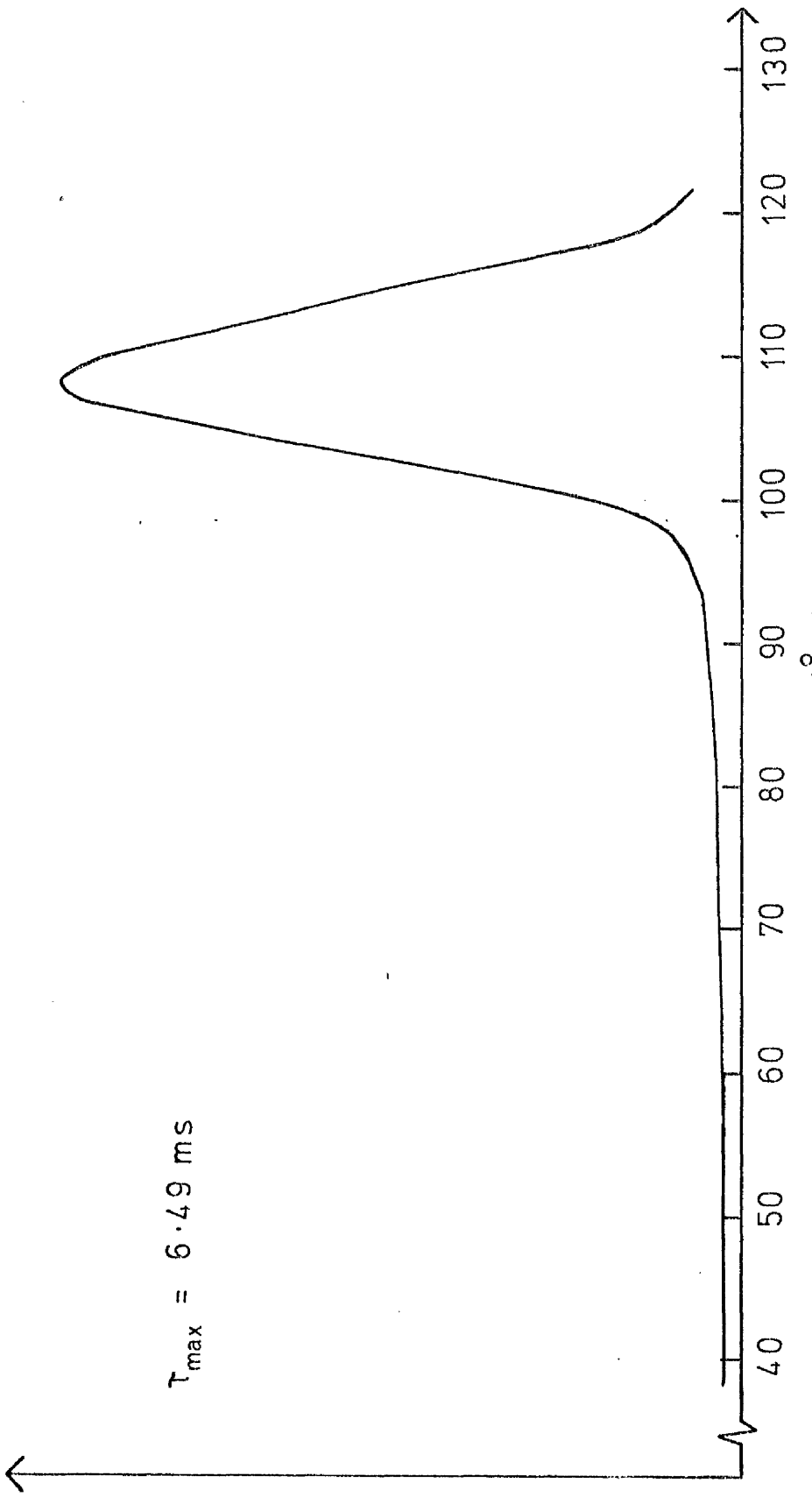

FIG.6.8 : A typical DLTS spectrum from VPE - GaAs.

Bias voltage = 1 volt

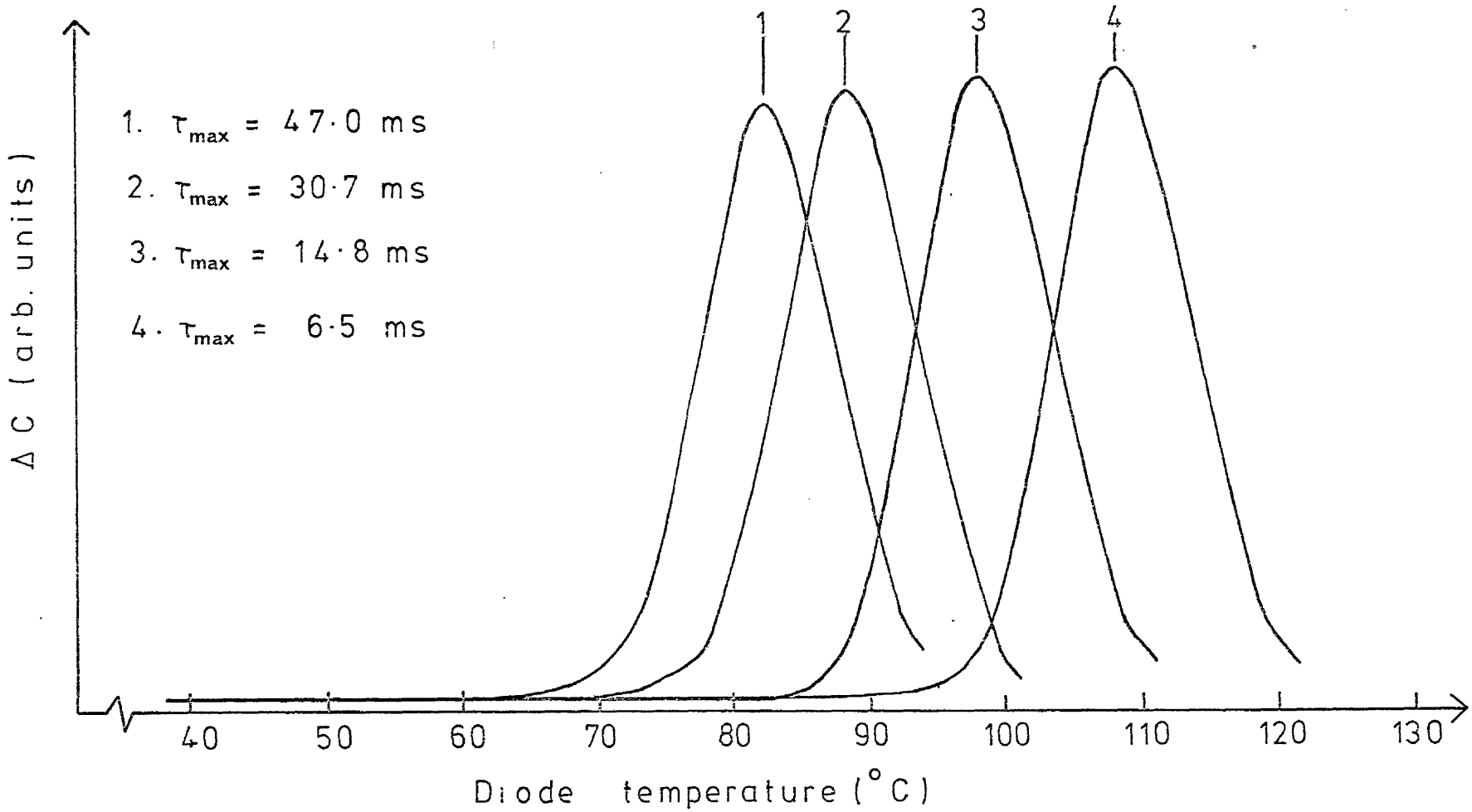

FIG.6.9 : Variation of peak position with rate-window for the dominant trap in VPE -GaAs.

constant t_2/t_1 ratio technique the peak shape remains unchanged for different rate-window settings.

The temperature dependence of the emission time constant for the trap is shown Fig. 6.10 which is an Arrhenius plot of $\ln(\tau T^2)$ versus $1/T$. The experimental points on the plot were obtained from the values of τ_{max} and T_p for each of the peaks recorded in Fig. 6.9. A least-square regression analysis of the experimental data shown in Fig. 6.10 yields a thermal activation energy for the trap of 0.82 eV $\pm$ 0.02 eV.

Referring to the detailed balance equation given in section 6.2, equation 6.9 and assuming emission of electrons from the deep level takes place to the L conduction band minima rather than the lower Γ band minimum (see the following discussion) then the constant term A is given by

$$A\ (GaAs) = 4 \times 10^{21}\ cm^{-2} s^{-1} K^{-2}$$

$$\text{since, } m_d^L = 0.55\ m_e \qquad (6.9)$$

$$\text{and} \quad m_c^L = 0.11\ m_e \qquad (6.10)$$

where, m_e is the electron rest mass.

Hence, using $\tau_{max} = 6.49$ ms and $T_p = 381$K, for example, and $g = {}^1/_2$ (6.9), the trap capture cross-section σ is calculated from equation 6.9 to be

$$\sigma = 4.5 \times 10^{-14}\ cm^2$$

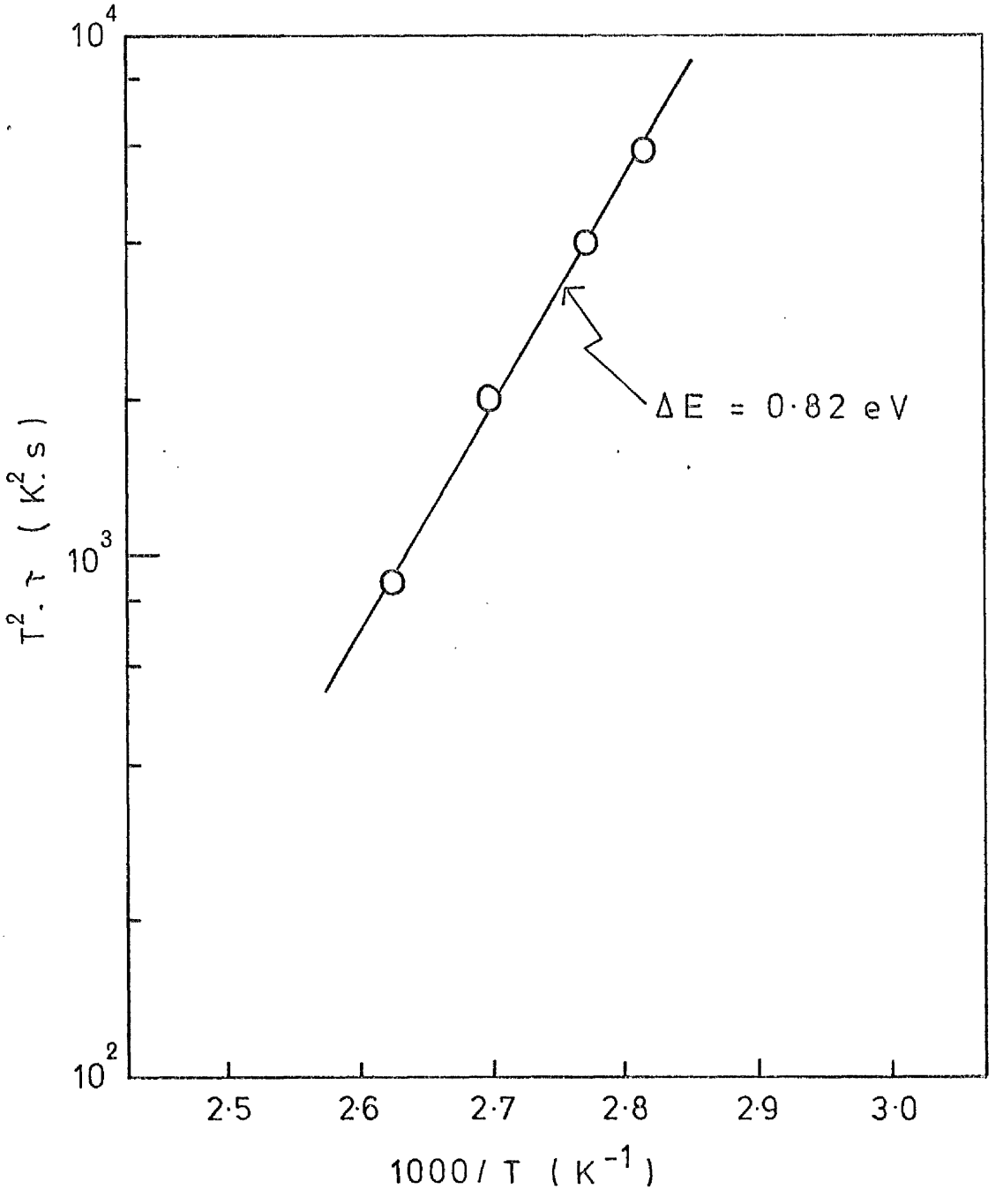

FIG. 6.10 : Activation energy plot of $T^2 . \tau$ against 1/T for the dominant trap in VPE grown GaAs.

6.4.2 Discussion

A deep electron trap has been found in GaAs grown by VPE having a thermal activation energy of 0.82 eV $\pm$ 0.02 eV and a capture cross-section of 4.5×10^{-14} cm^2. This result is in good agreement with published data for a 0.83 eV deep electron trap commonly found in both VPE and bulk-grown GaAs (6.9, 6.11). A comparison can be made with data reported on the 0.83 eV trap from other laboratories by plotting the $\ln (\tau T^2)$ versus $1/T$ curve presented here together with those curves obtained by other laboratories on a single graph; Fig. 6.11 illustrates such a graph. In addition to the author's results the lines shown in Fig. 6.11 were originally catalogued by Martin et al (6.3).

A comparison of the type shown in Fig. 6.11 is the best way to relate traps observed in different laboratories. The DLTS peak position at a fixed rate-window is more specific of a particular deep level than is the energy level alone since the DLTS peak position contains information on the capture cross-section as well as the thermal activation energy of the trap.

Majerfeld and Bhattacharya (6.9) have shown that electron emission from the 0.83 eV level in GaAs occurs to the L band minima rather than to the lower Γ conduction band minimum, hence the reason L band data was used in calculating the constant term A in the detailed balance equation (equation 6.9).

Much effort has been devoted to the identification

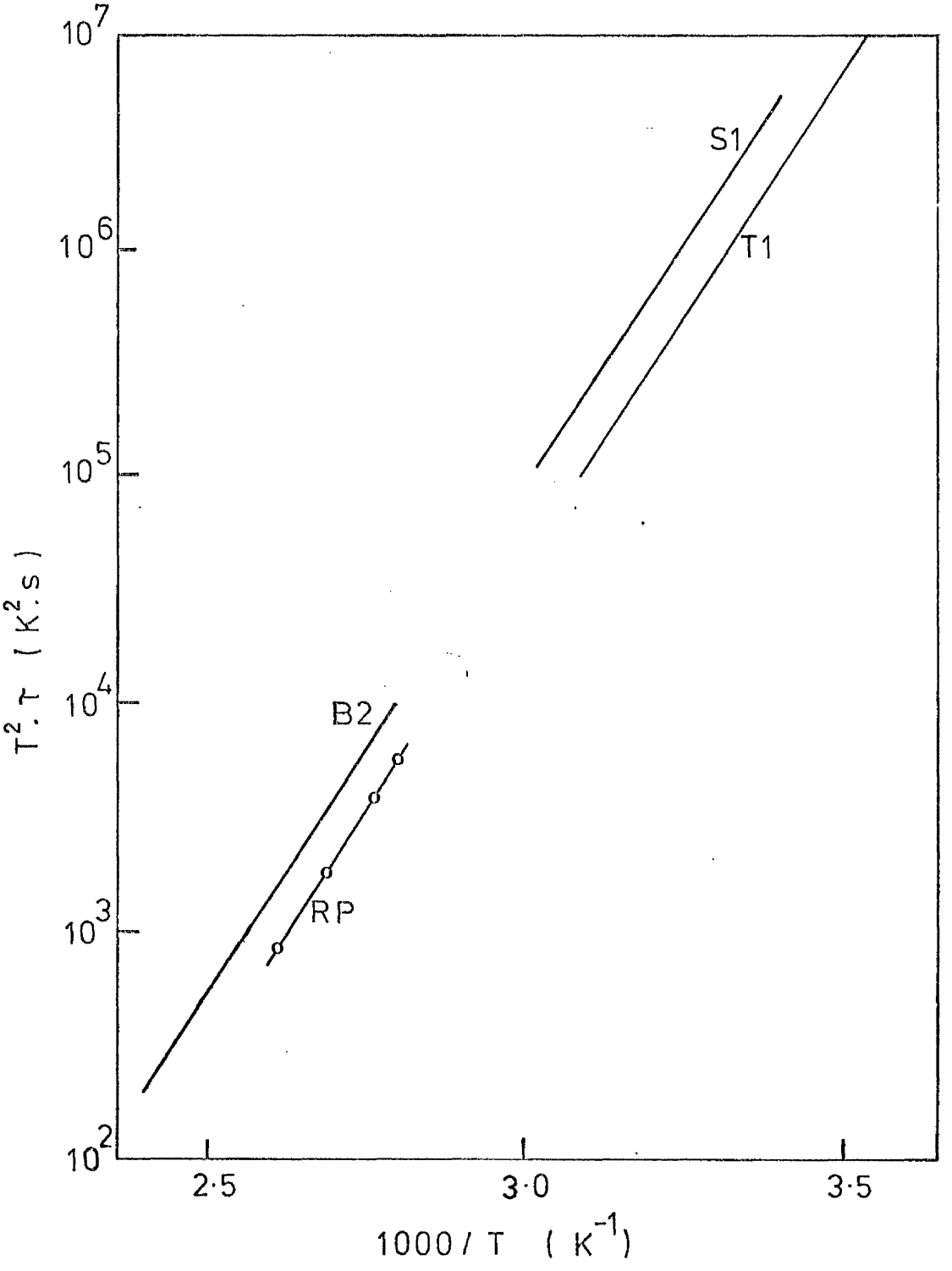

FIG. 6.11 : Activation energy plots for the 0·83 eV trap in GaAs from various laboratories.

S1 - Sheffield University ; T1 - Tokyo Univ.

B2 - Bell labs. ; RP - this work

of the 0.83 eV level in GaAs, however, the origin of the trap is still the subject of controversy having been variously assigned to impurity oxygen [6.12] and a Ga-vacancy or vacancy complex [6.13].

6.5 DLTS of InP Grown by MBE

Initially, unintentionally doped InP films were grown by MBE onto n^+-type substrates (Sn-doped, 10^{18} cm^{-3}) in order to facilitate DLTS measurements on the material. The formation of low-leakage Schottky-barriers on the as-grown epi-layers, however, proved to be a difficult problem. Several metals were deposited by vacuum evaporation onto the epi-layers, including Al, Au, Ag and Sn. These contacts, however, exhibited ohmic behaviour which is in contrast with the behaviour of metal-GaAs contacts which normally result in Schottky-barriers. Rectifying contacts were obtained by vacuum deposition of the metals mentioned above onto MBE grown InP epi-layers which were held at $\sim 250^{o}C$ for 5 mins in a 10^{-5}T vacuum prior to the metal evaporation process. These contacts, however, exhibited very 'leaky' reverse-bias characteristics.

In view of the difficulties found in fabricating good, low-leakage Schottky-barriers on as-grown InP, films were subsequently grown onto p^+-type substrates in order to form p^+-n junctions, therefore obviating the need for Schottky-barriers. The following section describes the growth of p^+-n InP junctions by MBE.

6.5.1 InP p^+-n Junction Fabrication

For the purpose of DLTS measurements, 2μm thick unintentionally doped InP layers (residual n-type, $N_D - N_A = 10^{16} - 10^{17}$ cm^{-3} were grown onto argon-ion sputter-cleaned p^+-type substrates (Zn-doped, 2×10^{18} cm^{-3}). The growth conditions were identical to those described in chapter 3, ie, a P-rich growth condition was maintained throughout. The substrate growth temperature however, was varied over a range from 250°C to 360°C. Ohmic contacts were formed on both the n- and p^+-type surfaces of the samples using Sn/Ni and Zn/Au evaporated contacts, respectively. Annealing of the ohmic contacts was done at 300°C for 1 - 2 mins in a forming gas ambient. The p^+-n junction diode area was defined by the epi-layer ohmic contact dimension (1mm dia. dot), with the p^+-type ohmic contact covering the whole of the back substrate surface area. Fig. 6.12(a) shows a schematic diagram of the InP p^+-n junction diode. Diodes so formed were bonded onto TO5 headers using conducting epoxy with contact to the epi-layer being made using the thermal-compression gold wire bond technique. Fig. 6.12 (b) shows a sample bonded onto a TO5 header ready for DLTS measurements.

The I-V characteristics of a diode grown at 360°C are shown in Fig. 6.13. As can be seen from the figure the diode has a good, low-leakage reverse-bias characteristic, the leakage-current at 2V reverse-bias,

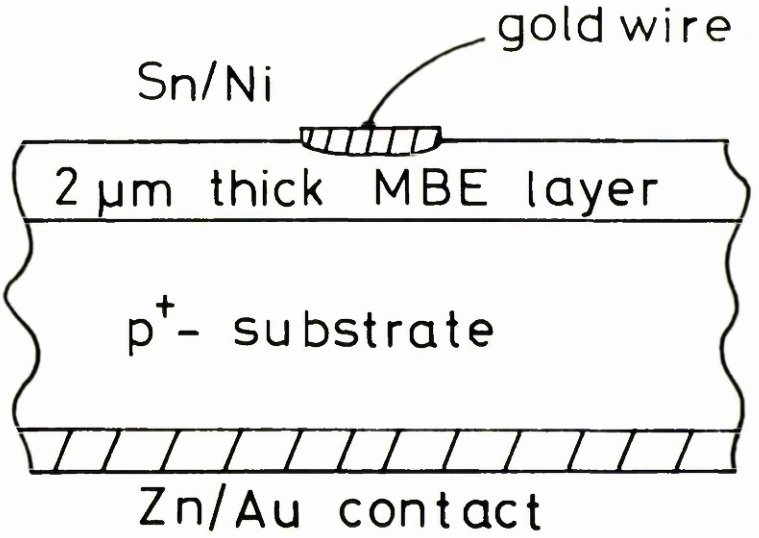

(a)

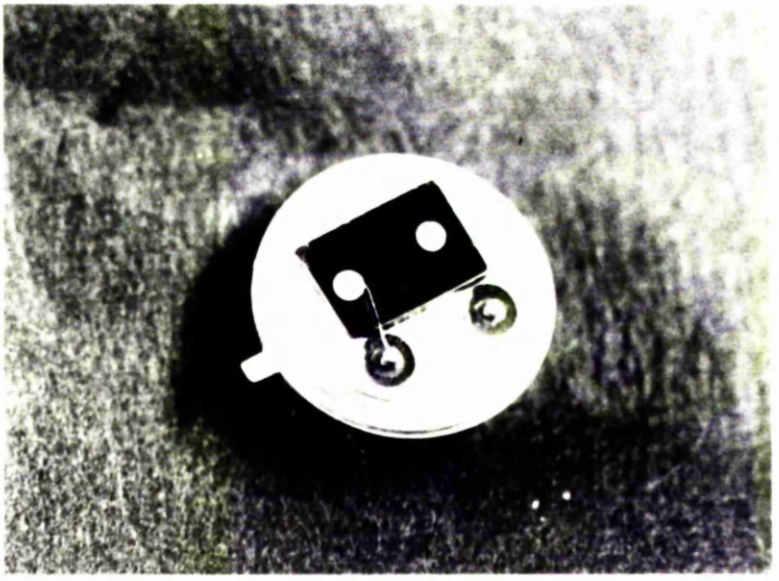

(b)

FIG.6.12 : InP p^+-n junction.

(a) Schematic diagram.

(b) Diode on TO5 header.

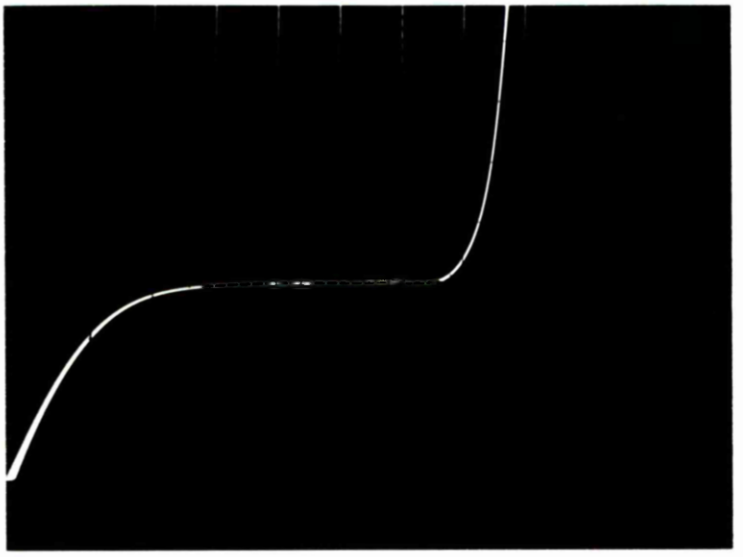

FIG. 6.13 : I-V Characteristics of an InP p^+-n junction grown by MBE. T_s = 360°C.

Horz. 1V/div ; Vert. 100μA/div.

for example, being ∿ 10μA. The reverse-bias characteristic, however, was found to deteriorate rapidly for diodes grown at temperatures <300°C and consequently DLTS measurements were only made on diodes grown in the temperature range from 300°C - 360°C.

Room temperature C-V measurements (see Appendix A.3) were made on the diodes prior to mounting them in the DLTS rig in order to determine the shallow donor concentrations in the films. Fig. 6.14 shows a C^{-2} versus V plot for a diode grown at 360°C. The slope of the straight line in the figure yields a nett donor concentration, N_D-N_A for the film of ∿ 4×10^{16} cm^{-3}. This result compares favourably with Hall effect measurements on films grown at 360°C (see chapter 3).

6.5.2 DLTS Results

InP p^+-n junctions were pulsed from 1V reverse-bias (typically) to zero-bias at a 10Hz repetition rate and 500μs pulse duration, and thermally scanned from 77K to 300K. Diodes were not heated above 300K since leakage currents were found to increase rapidly beyond room temperature due to the low contact potential (0.5 eV) of the diodes.

Fig. 6.15 shows a typical DLTS spectrum obtained from unintentionally doped InP grown by MBE. The sampling times, t_1 and t_2 were 5ms and 25ms, respectively, resulting in an emission time constant τ_{max} of 12.4 ms. The presence of a single deep electron trap is

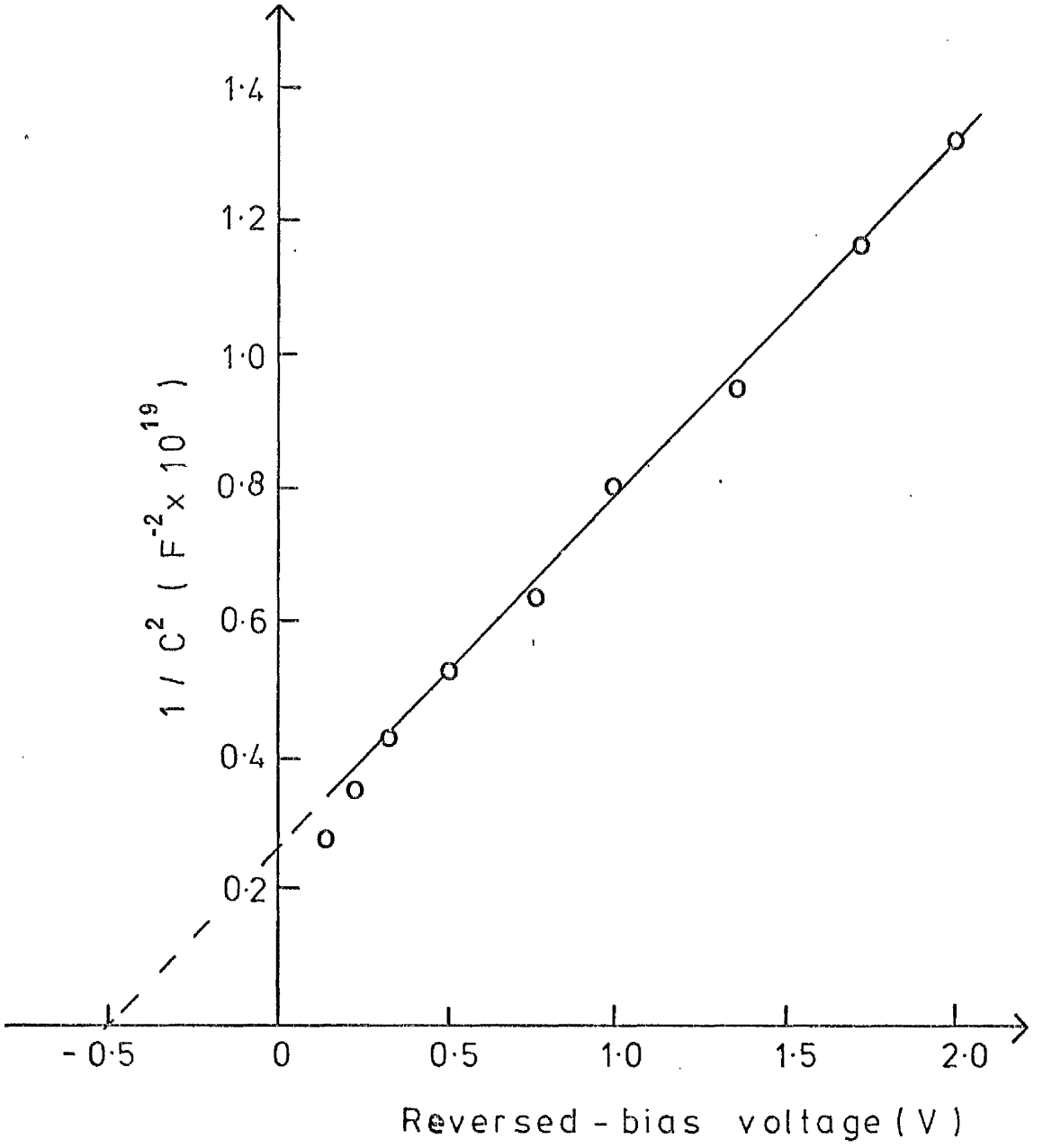

FIG. 6.14 : $1/C^2$ versus V plot for an InP p^+-n diode grown at 360 °C.

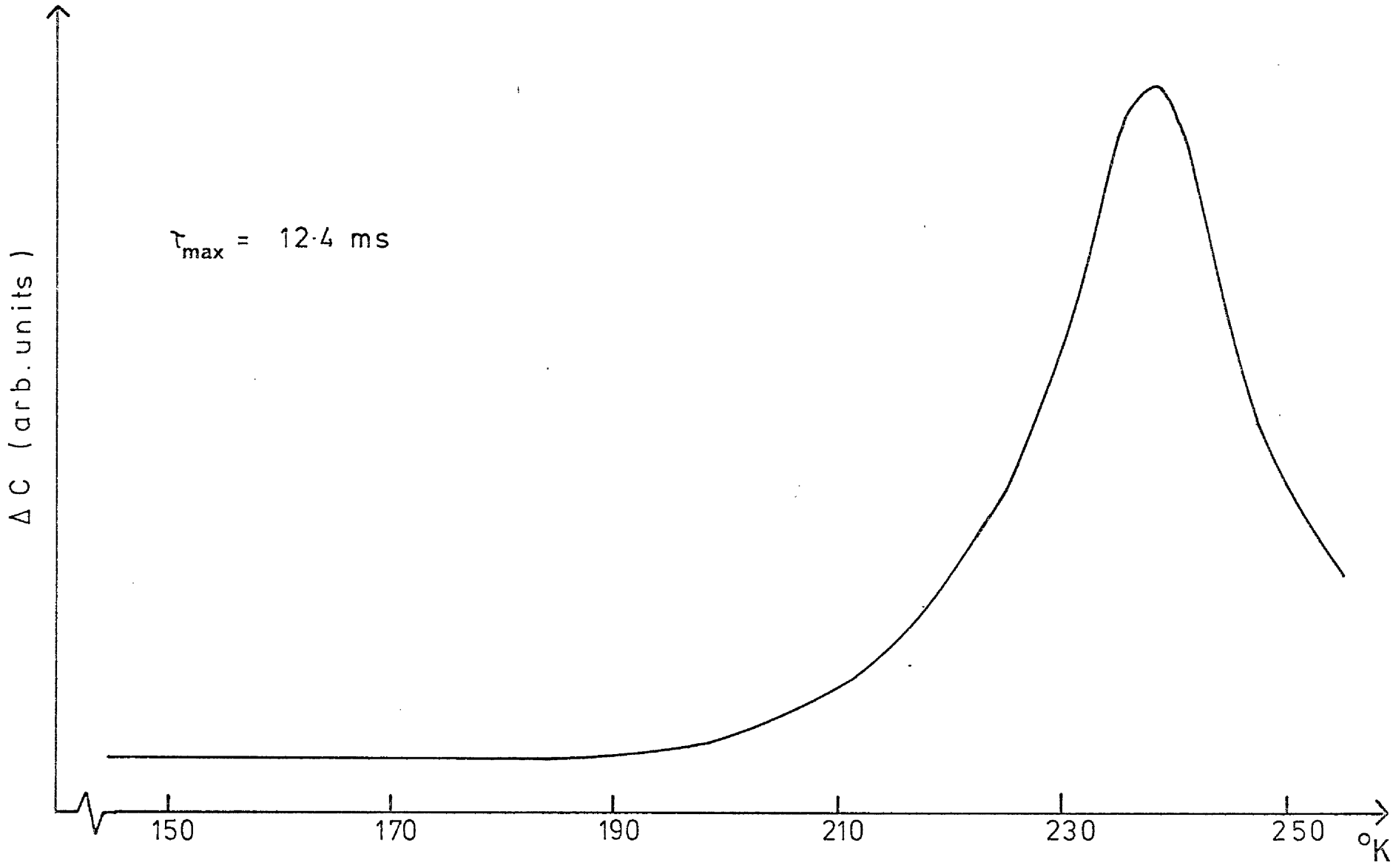

FIG. 6.15 : A typical DLTS spectrum from MBE grown InP.

indicated with the DLTS spectrum peaking at T_p = 238K. No other deep traps were detected in the temperature range from 77K to 300K.

The temperature dependence of the emission time constant for the trap is shown in Fig. 6.16. A least-square regression analysis of the experimental data shown in the figure yields an activation energy for the trap of 0.59 eV $\pm$ 0.02 eV. Again referring to the detailed balance equation given in section 6.2, equation 6.9 and assuming the trap couples with the L band minima rather than with the lower Γ band minimum (see the following discussion) the constant term A for InP is given by

$$A = 4.77 \times 10^{21}\ cm^{-2}s^{-1}K^{-2}$$
$$\text{since, } m_d^L = 0.78\ m_e \text{ and } m_c^L = 0.22 m_e \qquad (6.14)$$

Thus, using τ_{max} = 12.4 ms and T_p = 238K, for example, and g = 1/2, the trap capture cross-section σ is calculated from equation 6.9 to be

$$\sigma = 1.8 \times 10^{-12}\ cm^2$$

The trap concentration N_T in the depletion region can be estimated from an expression given by Lang [6.2] as

$$N_T = 2(N_D - N_A)\Delta C/Co \qquad (6.10)$$

where ΔC is the capacitance change at time t = 0, corresponding to the falling edge of the bias pulse, and

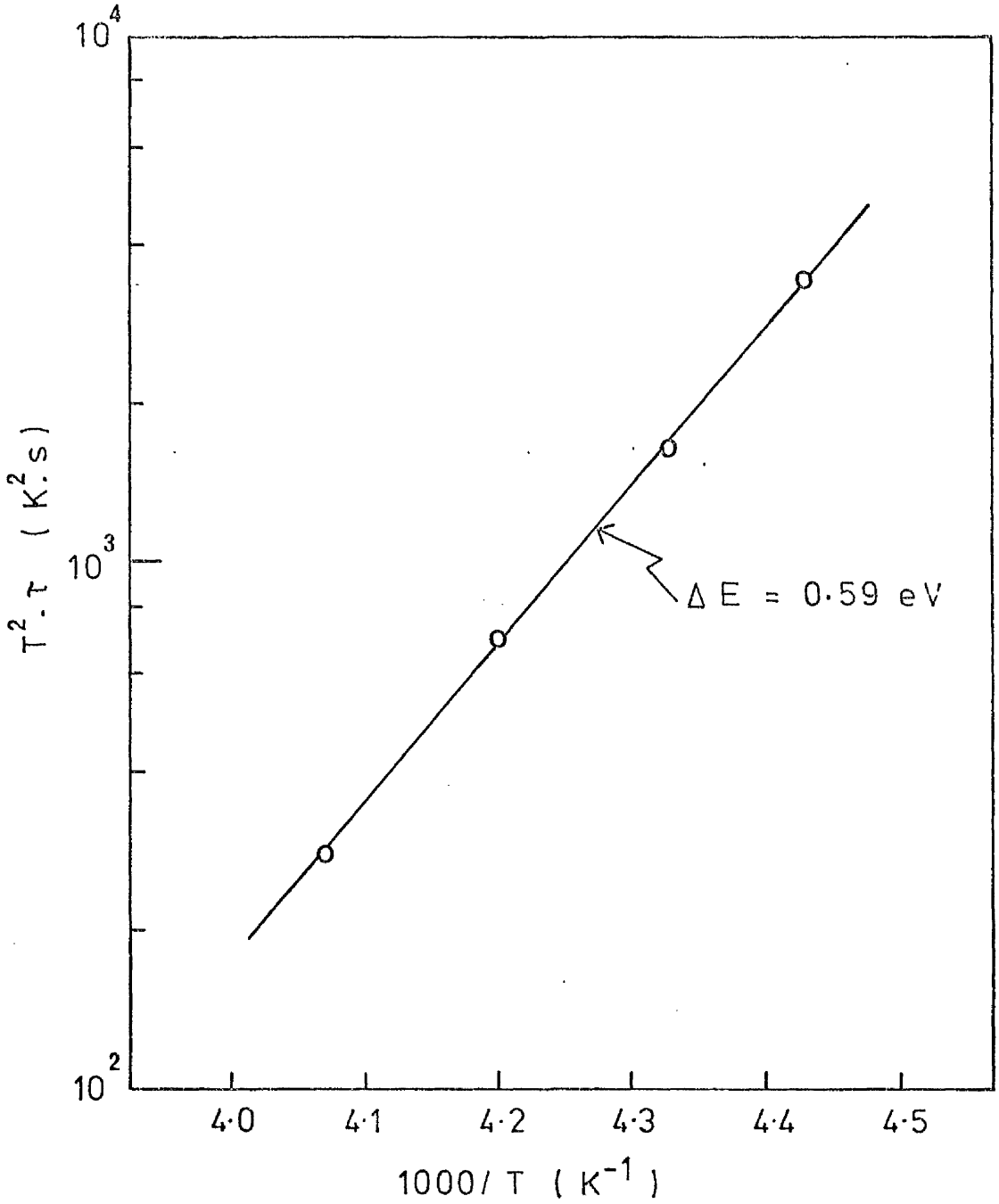

FIG. 6.16 : Activation energy plot of $T^2.\tau$ against 1/T for the dominant trap in MBE grown InP.

Co is the diode capacitance under quiescent conditions. Fig. 6.18 shows a plot of N_T versus the substrate growth temperature for three values in the temperature range from 300°C to 360°C.

6.6 Discussion of Results

A dominant deep electron trap has been detected for the first time in InP grown by MBE having a thermal activation energy of 0.59 eV and a trap capture cross-section of 1.8×10^{-12} cm^2. The trap is similar to that observed by White et al [6.5], labelled as trap S, and by Wada et al [6.6], labelled as trap D, in VPE and bulk-grown InP. Wada et al have found evidence to suggest that their trap D (ΔE = 0.59 eV, $\sigma = 1.9 \times 10^{-12}$ cm^2) couples with the L conduction band minima rather than with the lower Γ conduction band minimum. The conclusions of Wada et al with regard to the interaction of three deep levels, namely, A, D and E at 0.34 eV, 0.59 eV and 0.63 eV, respectively, with the conduction bands of InP are summarised in Fig. 6.17. As can be seen from the figure traps A and D couple with the L band minima while trap E couples with the lower Γ conduction band minimum.

The concentration of the 0.59 eV trap in MBE grown InP has been found to be dependent on the substrate growth temperature. For example, the trap concentration increases from 9×10^{14} cm^{-3} to 3×10^{15} cm^{-3} as the substrate growth temperature is lowered from 360°C to 300°C. It is postulated in direct analogy with results

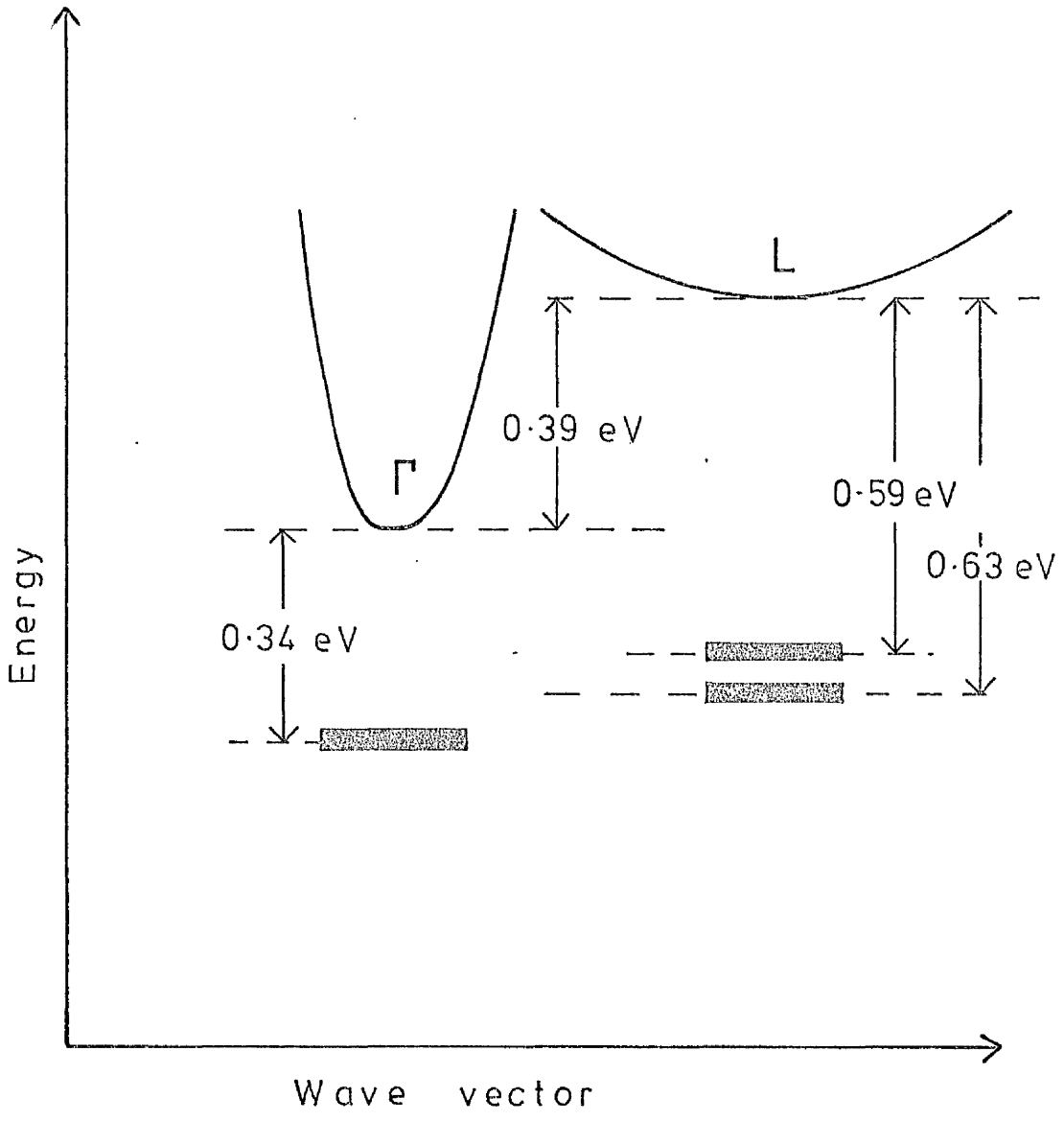

FIG. 6.17 : Schematic diagram showing energy levels of three different electron traps in InP.

(Ref. 6.6)

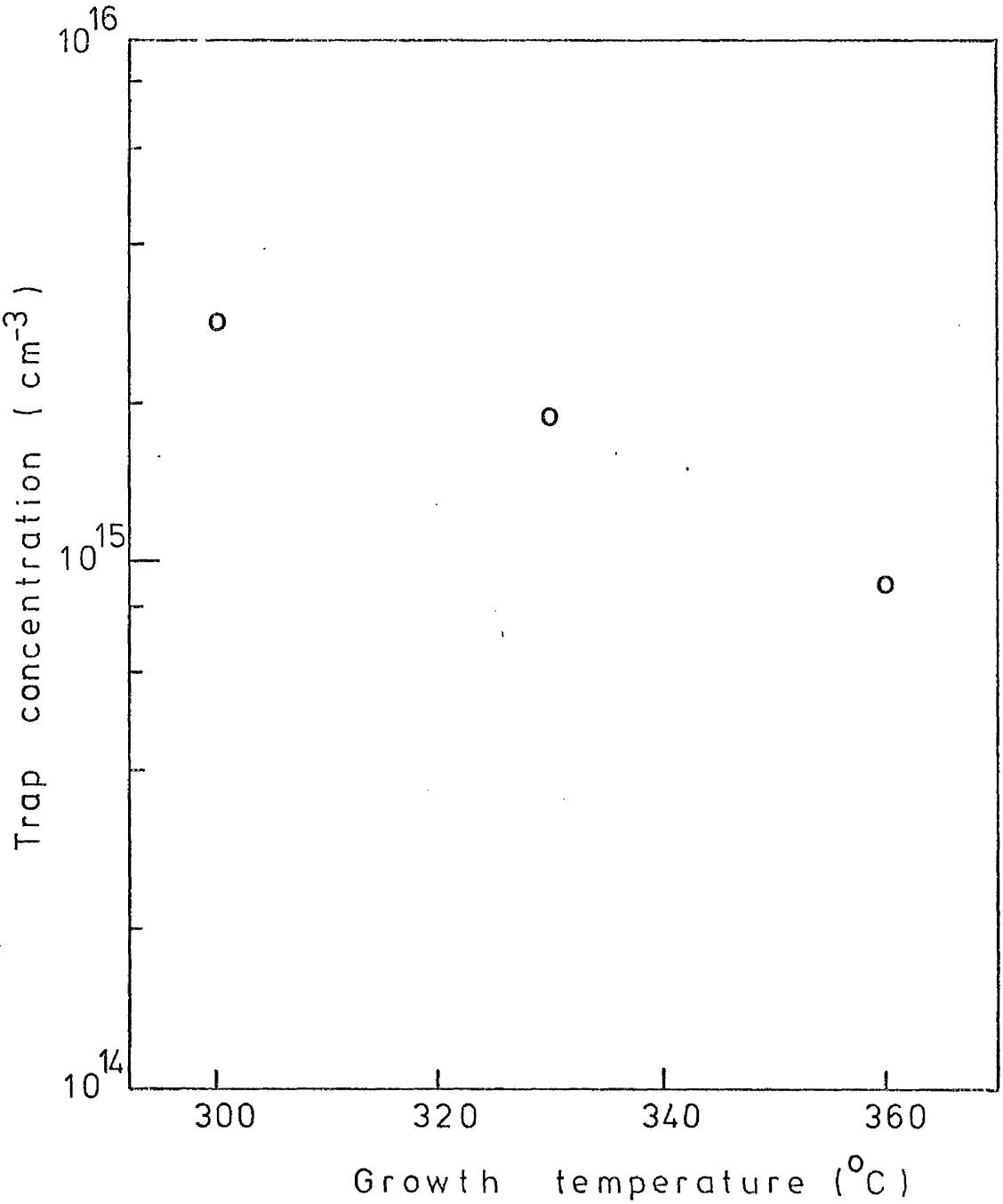

FIG. 6.18 : 0·59 eV trap concentration in MBE grown InP versus substrate growth temperature for three films.

reported on the substrate growth temperature dependence of trap concentrations in GaAs grown by MBE [6.4] that the 0.59 eV trap in MBE grown InP is due to In-vacancies or In-vacancy complexes formed during epitaxial film growth. In-vacancies or complexes involving In-vacancies and impurities are expected to be created in films grown under P-rich growth conditions, ie, with excess P present during growth. The formation of such defects will be enhanced at lower substrate growth temperatures due to an increase in the P surface population.

The influence of growth parameters on defect generation is not confined to the MBE growth technique. For instance, the concentration of tne 0.83 eV electron trap in VPE grown GaAs has been found to depend on both the substrate growth temperature and the $AsCl_3$ mole fraction in the reactor tube during growth. Ozeki et al [6.15] have observed an increase in the 0.83 eV trap concentration from 5×10^{12} cm^{-3} to 5×10^{14} cm^{-3} as the growth temperature is reduced from 1030°C to 900°C. These authors also report an increase in the trap concentration from 1×10^{13} cm^{-3} to 2×10^{14} cm^{-3} as the $AsCl_3$ mole fraction is increased from 1×10^{-3} to 9×10^{-3}.

It is interesting to note that no electron traps have been detected in either GaAs or InP grown by the LPE technique which corresponds to the extreme limit of group III-rich growth conditions.

The creation of lattice vacancies or vacancy-complexes during epitaxial layer growth is of

fundamental importance with regard to mechanisms governing the incorporation of elements as donors and/or acceptors. The interplay of vacancy generation and impurity element incorporation as a function of surface stoichiometry during growth is discussed in more detail in chapter 2.

Amendment to section 6.5

A total of ten 2μm thick unintentionally doped films were grown onto Zn doped p^+-type substrates in the temperature range from 300 - 360^{o}C and ohmic contacts were made on all ten samples. Of the ten diodes fabricated seven were found to be suitable for DLTS measurements, exhibiting I-V and $1/C^2$-V characteristics such as those illustrated in Figs. 6.13 and 6.14. Since the DLTS spectra obtained from the seven 'good' diodes peaked at the same temperature for a fixed rate window setting, the estimated accuracy in the temperature measurement being $\pm$ 0.5K, it was concluded that the trap was identical in all but density (trap density being a function of peak height rather than peak position) in each of the diodes tested. Consequently the activation energy plot illustrated in Fig. 6.16 was only plotted once. The errors given in the estimation of ΔE and σ arose from the least-square regression analysis of the experimental points in this activation energy plot.

CHAPTER 7.

CHAPTER 7

CONCLUSIONS

7.1 Growth and Characterisation of Unintentionally Doped InP

It has been shown that the commonly adopted in-vacuo substrate cleaning technique of argon ion sputtering followed by annealing produces a thin conducting layer at the surface of semi-insulating InP substrates. The conducting layer is n-type as measured by the Hall-effect with N_D-N_A in the range $10^{16}-10^{17}cm^{-3}$. Sullivan and Park [7.1] have recently found the layer to be an n-type spike with an approximate half-width of 1,000Å using a B.T.R.L. automatic C-V profiler [7.2]. The layer has also been shown to contain deep level carrier traps which act as non-radiative recombination centres as deduced from an observed reduction in the photoluminescence yield from sputter-cleaned n^+-type InP substrates. A consequence of the conducting layer is that the characterisation of both the electrical and optical properties of subsequently deposited MBE films is seriously influenced by the presence of the substrate/film interface layer. It has been demonstrated that Hall-effect measurements on <1μm thick InP films grown by MBE onto sputtered and annealed semi-insulating substrates are not representative of the epitaxial layers themselves, typical results from unintentionally doped material being $N_D-N_A \simeq 3 \times 10^{16}cm^{-3}$ and $\mu<1,000cm^2V^{-1}s^{-1}$ at R.T. The results obtained from

plasma reflectivity measurements, on the other hand, are more representative of the films since the infrared radiation only penetrates ∿ 0.5μm into the films at the resonant frequency. Since higher R.T. electron mobolities were obtained using the plasma reflectance technique, typically in the range 2,500 → 3,000 $cm^2V^{-1}s^{-1}$ with $N_D-N_A \simeq 10^{17}cm^{-3}$, it is concluded that Hall-effect measurements are degraded on account of the substrate/film interface layer. The interface layer which has been shown to contain non-radiative recombination centres is also thought to be responsible for the extremely weak photoluminescence yield (only detectable at 7K) from <1μm thick InP films grown onto sputtered and annealed substrates. This conclusion is supported by the fact that Stanley (3.16) has recently grown InP films exhibiting efficient R.T. photoluminescence which were grown by MBE onto heat-cleaned substrates as opposed to argon ion sputtered and annealed substrates. The heat-cleaning technique employed by Stanley consisted of raising the substrate temperature to ∿ 500°C for a few minutes under exposure to a large phosphorus flux. The growth of epitaxial unintentionally doped InP films, however, has been demonstrated onto sputtered and annealed substrates as indicated by texture camera and electron channelling analyses, implying that sputtered and annealed substrate surfaces are crystallographically undamaged on a macroscopic level.

7.2 Growth and Characterisation of Zn and Be Doped InP

Contrary to the expected result, Zn has been shown to have a near unity sticking coefficient on (100) InP grown by MBE at substrate temperatures around 360°C up to concentrations of $\sim 10^{19}cm^{-3}$. This result is unexpected on account of the high vapour pressure of Zn at 360°C ($2x10^{-2}$Torr) and also in view of the fact that Zn has a zero sticking coefficient on GaAs at temperatures > 100°C(4.1). With Zn flux levels at the substrate $>3x10^{11}cm^{-2}s^{-1}$ the Zn concentration in films tends to an apparent saturation level of $\sim 6x10^{20}cm^{-3}$. It is concluded that $6x10^{20}cm^{-3}$ represents the solid solubility limit of Zn in InP grown under the non-equilibrium conditions of MBE at substrate temperatures around 360°C. Zn concentrations in InP films as high as $4x10^{20}cm^{-3}$ have been achieved with no apparent degradation of either the surface morphology or crystal structure relative to unintentionally doped material. Furthermore, X-ray double crystal diffractometry analysis of heavily Zn doped MBE grown InP showed the films to be strain-free and hence it is concluded that the Zn is comfortably accomodated in the InP lattice even at Zn concentrations exceeding $10^{20}cm^{-3}$. Since plasma reflectivity measurements indicated that the electrical properties of Zn doped films are almost identical to those of unintentionally doped films it is apparent that very little or perhaps none of the Zn content is substitutional on In sites. It is postulated that most

of the Zn is tied up in some form of complex such as that proposed by Tuck and Hooper [4.12] to account for the large carrier/atom inequality in Zn-diffused InP. Tuck and Hooper [4.12] have suggested that most of the Zn in Zn-diffused InP occurs in the form of the complex $V_p Zn_{In} V_p$. Clearly, however, there is insufficient data to propose a model to account for the carrier/atom inequality found in MBE grown Zn doped InP. An extended investigation would be required involving the measurement of the carrier/atom ratio as a function of both the surface stoichiometry during growth (J_{P_2}/J_{In} ratio) and substrate temperature in order to obtain a greater appreciation of the mechanism involved. Such an investigation, however, is likely to introduce more uncertainties since the electrical properties of unintentionally doped MBE films are critically dependent on both the surface stoichiometry and substrate temperature.

Be has been shown to have a near unity sticking coefficient on (100) InP grown by MBE at substrate temperatures around 360°C with Be concentrations in films being achieved ranging from 5×10^{17} to $2 \times 10^{19} cm^{-3}$. This result is expected since Be has an extremely low vapour pressure at 360°C ($< 10^{-14}$ Torr) and consequently should have a near infinite surface lifetime on substrates held at this temperature. The Be doped films were found to be epitaxial as indicated by texture camera analysis and had excellent surface morphologies, implying that Be is

readily incorporated into the InP lattice. At this stage it is difficult to draw definite conclusions regarding the electrical properties of Be doped InP films grown by MBE since Hall-effect measurements largely proved unsuccessful and the results from plasma reflectivity measurements were not available at the time of writing. It seems apparent, however, that the Be is activated to some extent since the electrical properties of Be doped films are markedly different from those of unintentionally doped films.

To summarise, it has been conclusively shown that Zn is unsuitable as a p-type dopant whether evaporated as Zn^+ or neutral Zn on account of its electrical in-activity in as-grown films while Be appears to be activated to some extent although the non-trivial electrical contact problem remains to be solved before Be doped films can be more rigorously characterised.

7.3 DLTS Study of MBE-InP

It has been established from DLTS measurements that unintentionally doped (100) InP grown by MBE in the substrate temperature range 300-360^{o}C contains a dominant deep level electron trap having a thermal activation energy of 0.59eV and a capture cross-section of $1.8 \times 10^{-12} cm^2$. Since the concentration of the trap has been shown to increase with decreasing substrate temperatures it is concluded that the deep level corresponds to a native defect in the crystal rather than an impurity. It is

postulated that the deep level is due to In-vacancies or In-vacancy complexes formed during epitaxy, the increase in the trap concentration resulting from an increase in the P surface population at lower substrate temperatures.

7.4 Future Work

Since the argon ion sputtering and annealing substrate cleaning technique has been shown to seriously influence the characterisation of MBE films it is strongly suggested that this technique be abandoned in favour of the heat-cleaning technique recently developed by both Roberts [1.33] and Stanley[3.16], involving heating substrates to $\sim 500^{o}C$ under exposure to a phosphorous beam. In the early stages of an investigation of heat-cleaning, however, it would be necessary to monitor the substrate cleanliness using Auger electron spectroscopy and therefore an AES facility would have to be incorporated in the system. With regard to further p-type doping studies it is suggested that Mg and Mn be tested as potential dopants in MBE grown InP in addition to re-investigating the incorporation of Zn and Be in InP grown by MBE onto heat-cleaned substrates. Finally, in order to verify that the 0.59eV deep trapping level in MBE grown InP is due to In-vacancies or In-vacancy complexes it is suggested that the trap concentration in films be measured by DLTS as a function of the phosphorus flux level at the substrate during growth. Another

interesting area of study would be to compare the DLTS spectra obtained from InP films grown using P_2 and P_4 molecular beams. The P_4-P_2 cracking cell developed by Roberts [1.33] would be ideal as the source of both P_2 and P_4 molecules for these experiments.

APPENDICES

APPENDIX A ANALYTICAL TECHNIQUES

A.1 X-Ray Cylindrical Texture Camera

The atoms constituting a crystalline semiconductor effectively form a diffraction grating and consequently X-ray techniques which make use of the Bragg condition can be employed in order to determine interplanar spacings and thus identify crystallographic planes. One such X-ray diffraction technique which is commonly used to examine the crystallographic quality of thin semiconductor films is the cylindrical texture camera technique [A.1]. This technique is particularly suited to the analysis of thin crystalline films grown on flat substrates since diffraction spots (or lines) due to the underlying substrate are greatly attenuated and can be distinguished from those due to the film [A.1].

The texture camera arrangement shown schematically in Fig. A.1.1 consist of a cylindrical cassette with collimator and beam stop tubes concentric with the camera axis. The specimen is mounted on a disc which rotates the specimen in its own plane; the angle between the disc normal and camera axis being 60^{o}. A cylindrical photographic film mounted on the inside of the cassette records the diffraction pattern. Interpretation of the diffraction spots (or lines) is made by application of Bragg's law,

$$2d\sin\theta = n\lambda \qquad (A.1.1)$$

where d is the interplanar spacing and λ is the wavelength

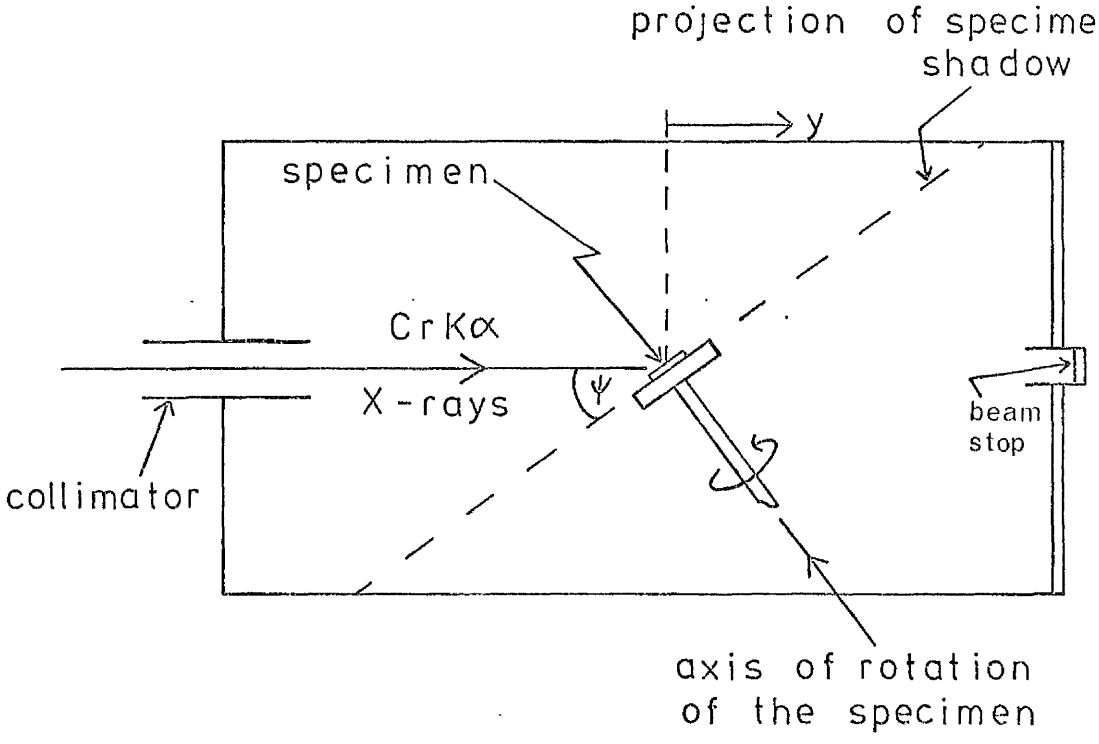

FIG. A.1.1 : Schematic of cylindrical texture camera.

(Ref. A.1)

of the incident X-ray radiation. The position of a spot y along the camera axis is related to the angle θ between the incident X-ray beam and the diffracting plane by the equation,

$$y = R\cot 2\theta \qquad (A.1.2)$$

where R is the camera radius. Hence by measuring the positions of the spots the interplanar spacings d may be determined. The angle of incidence $(90^{o}-\Psi)$ sets a lower limit to the value of 2θ, in this case 30^{o}, while the upper limit is set at the line y=o, corresponding to $2\theta=90^{o}$. Single diffraction spots are obtained corresponding to individual planes provided the specimen is mounted such that the (100) crystal plane normal is in same plane as the incident X-ray beam. If the specimen is mounted slightly off-axis multiple spots are obtained which correspond to diffraction from individual crystal planes. Diffraction patterns illustrating both these cases are presented in this thesis (see, for example, Figs. 3.20 and 4.17).

A.2 Hall-Effect Measurements

Exploitation of the Hall-effect [A.2] is the most commonly used means of determining the majority carrier polarity (n- or p-type), mobility and carrier concentration in a semiconductor. Briefly the Hall-effect relies on the fact that when a magnetic field is applied at right angles to a direction of current flow, the moving charge carriers which constitute the current (electrons or holes) experience a force (the Lorentz force) proportional to both their velocity and the magnetic field strength, and are deflected at right angles to both the magnetic field and current flow directions.

The Hall-effect measurement arrangement used in this work is shown schematically in Fig. A.2.1. A 5 pad contact pattern of Al electrodes was deposited by vacuum evaporation onto the surface of InP films grown by MBE onto semi-insulating substrates, high resistivity substrates being required to prevent electrical "short circuiting" of the films. The Al-InP contacts were shown to be "ohmic" at both 300K and 77K. Electrical contact was made to the Al electrodes via gold wire attached with silver conducting paste and bonded samples were immersed in liquid nitrogen with their planes normal to a magnetic field of flux density 0.2 Tesla.

The film conductivity σ is determined by passing a known current I through the film between contacts 3 and 4 and measuring the corresponding voltage V_C generated between contacts 1 and 2. The conductivity is calculated

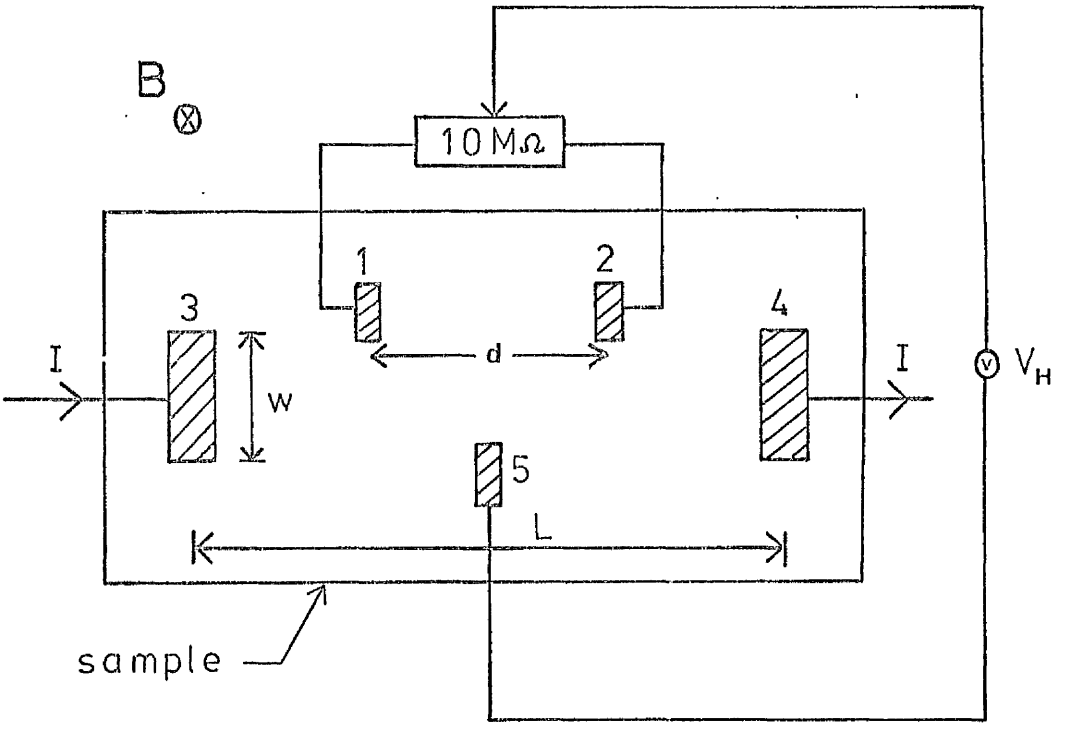

FIG. A.2.1 : Hall-effect contact pattern.

from

$$\sigma = \frac{I}{V_C} \cdot \frac{d}{wt} \qquad (A.2.1)$$

where t is the film thickness. The voltage generated between contacts 1, 2 and 5 is known as the Hall voltage V_H which is used in calculating the Hall coefficient R_H given by

$$R_H = \frac{V_H t}{I B} \qquad (A.2.2)$$

where B is the magnetic flux density. Charge carrier density is then given by

$$n = r(qR_H)^{-1} \qquad (A.2.3)$$

where r is a correction factor which is dependent on the scattering mechanism. For phonon scattering r = 1.18. Finally, the Hall mobility μ_H is obtained from

$$\mu_H = R_H \sigma \qquad (A.2.4)$$

It should be noted that the Hall mobility μ_H differs from the drift mobility μ_d by the factor r such that

$$\mu_H = r\mu_d \qquad (A.2.5)$$

Hence by measuring V_C and V_H both the carrier concentration and mobility in films can be determined. The carrier type can also be obtained by noting the polarity of V_H.

A.3 Capacitance - Voltage (C-V) Profiling

The doping profile of thin semiconductor films is commonly determined by measuring the capacitance C of a Schottky diode or p^+-n junction (for the case of n-type films) as a function of reverse bias voltage V_R - see, for example, references A.3 - A.6.

Consider an ideal Schottky barrier (ie, neglecting interface states) or p^+-n junction under reverse bias conditions; the energy band diagram for such a diode is illustrated in Fig. A.3.1. It can be shown (A.7) that the electric field strength ξ_{max} at the interface is given by

$$\xi_{max} = [(2qN_D)/\epsilon_s\ (V_D - kT/q)]^{1/2} \qquad (A.3.1)$$

where V_D is the diffusion voltage associated with the reverse bias V_R and N_D is the donor density in the n-type material. From Gauss's theorem the charge in the depletion region due to the ionised donors is given by

$$Q_D = \epsilon_s\ \xi_{max} = (2q\epsilon_s N_D)^{1/2}\ (V_D - kT/q)^{1/2} \qquad (A.3.2)$$

so that

$$C = \frac{\partial Q_D}{\partial V_R} = \frac{\partial Q_D}{\partial V_D}$$

$$= (q\epsilon_s N_D/2)^{1/2}\ (V_D - kT/q)^{-1/2} \qquad (A.3.3)$$

Since $V_D = V_{DO} + V_R$, where V_{DO} is the diffusion voltage at zero bias, equation A.3.3 may be written

$$C = (q\epsilon_s N_D/2)^{1/2}\ (V_R + V_{DO} - kT/q)^{-1/2} \qquad (A.3.4)$$

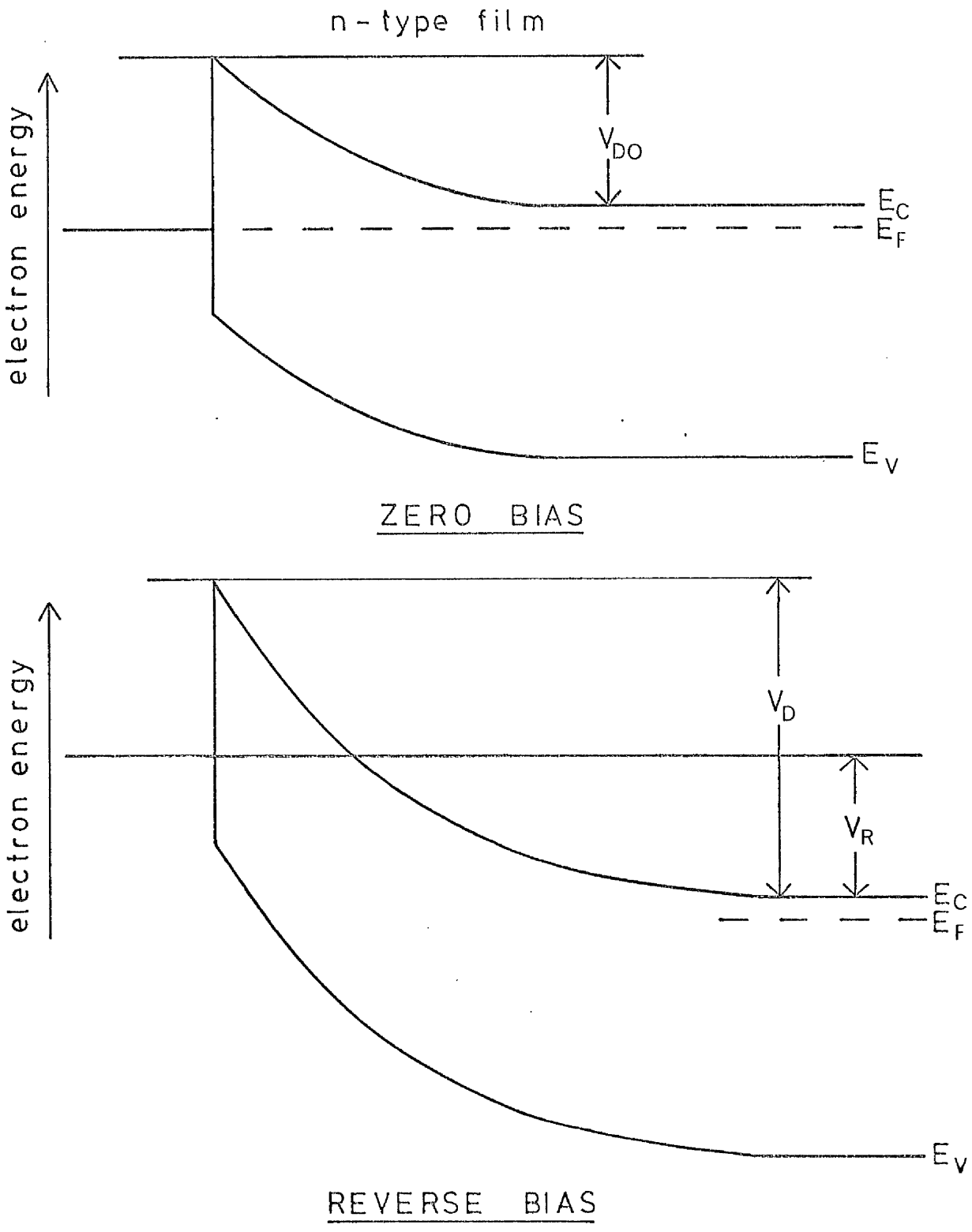
n-type film
electron energy
V_{DO}
E_C
E_F
E_V
ZERO BIAS
electron energy
V_D
V_R
E_C
E_F
E_V
REVERSE BIAS

FIG. A.3.1

Equation A.3.4 shows that a graph of $1/C^2$ as a function of V_R should be a straight line with a slope of $2/q\epsilon_s N_D$ and a negative intercept on the V_R axis equal to $-V_{DO} + (kT/q)$. Hence N_D can be determined from such a plot with V_{DO} being additionally available. If the graph of $1/C^2$ versus V_R is not a straight line then N_D is not uniform throughout the semiconductor film. In such a case the donor density can be determined at any depth into the film by obtaining $\partial(1/C^2)/\partial V_R$ at specific points on the $1/C^2$ versus V_R curve. The depletion width W and hence the depth into the film at a particular reverse bias voltage can then be calculated from

$$W = (2\epsilon_s/qN_D\ (V_R + V_{DO} - kT/q))^{1/2} \qquad (A.3.5)$$

APPENDIX B LIST OF PUBLISHED WORK

1. R.M. PARK, C.R. STANLEY and R. CLAMPITT,
   "A low-energy ion source for p-type doping in MBE",
   Inst. Phys. Conf. Ser. No 54, 235 (1980)
2. R.M. PARK and C.R. STANLEY,
   "Zinc ion doping of InP by MBE",
   2nd Annual Workshop in MBE, Cornell University,
   New York, October 1980
3. M.A. AKHTER, R.M. PARK, C.R. STANLEY and S. YOSHIDA,
   "N-type and p-type InP by MBE",
   European Workshop on MBE, Stuttgart, March 1981
4. R.M. PARK and C.R. STANLEY,
   "Incorporation of neutral zinc into InP by MBE",
   To be published in J. Appl. Phys.
5. R.M. PARK and C.R. STANLEY,
   "Characterisation of a deep electron trap in
   molecular beam epitaxial InP",
   Elec. Letts., 17, 669 (1981)
6. P.W. SULLIVAN and R.M. PARK,
   "Effect of surface treatment on the growth and
   characterisation of (100) InP by MBE",
   To be published in J. Cryst. Growth

TO: The Librarian, Electronics & Electrical Engineering Dept.

Received from the University Librarian by the Department of

...ELECTRONICS & ELECTRICAL ENGINEERING on indefinite loan, the ~~thesis~~ theses detailed below.

Signature .....

Position .....

Date .....

Thesis 7362: NUTT
Thesis 7161: DEVINE

Please sign this receipt, and return it to:

Gifts & Exchanges Department, Glasgow University Library,
Hillhead Street, Glasgow G12 8QE.

GUL 73.252

REFERENCES CHAPTER 1

1.1 A.Y. CHO, J.R. ARTHUR,
Progress in Solid-State Chemistry, 10, 157 (1975)

1.2 A. Y. CHO,
J. Vac. Sci. Technol., 16, 275 (1979)

1.3 L. L. CHANG, L. ESAKI, W.E. HOWARD, R. LUDEKE,
J. Vac. Sci. Technol., 10, 11 (1973)

1.4 K. PLOOG, A. FISCHER, H. KÜNZEL,
J. Electrochem. Soc., 128, 400 (1981)

1.5 G.H. DÖHLER, K. PLOOG,
Prog. Cryst. Growth Charact., 2, 145 (1979)

1.6 J.E. DAVEY, T. PANKEY,
J. Appl. Phys., 39, 1941 (1968)

1.7 J.T. GRANT, T.W. HASS,
J. Vac. Sci. Technol., 8, 94 (1971)

1.8 J.R. ARTHUR,
J. Appl. Phys. 39, 4032 (1968)

1.9 J.R. ARTHUR, J.J. LEPORE,
J. Vac. Sci. Technol., 6, 546 (1969)

1.10 A.Y. CHO, R.W. DIXON, H.C. CASEY, R.L. HARTMAN,
Appl. Phys. Lett., 28, 501 (1976)

1.11 W.T. TSANG, M. ILEGEMS,
Appl. Phys. Lett., 31, 301 (1977)

1.12 A.Y. CHO, F.K. REINHART,
J. Appl. Phys., 45, 1812 (1974)

1.13 A.Y. CHO, C.N. DUNN, R.L. KUVAS, W.E. SCHROEDER,
Appl. Phys. Lett., 25, 224 (1974)

1.14 S. HIYAMIZU, K. NANBU, T. FUJII, T. SAKURAI,
H. HASHIMOTO, O. RYUZAN,
J. Electrochem. Soc., 127, 1562 (1980)

1.15 T. MORIYAMA, O. FUKUDA, K. SANADA, K. INADA,
S. TANAKA, K. CHIDA, T. EDAHIRO,
6th European Conf. on Optical Comm. I.E.E.
Conf. Pub. No. 190 (1980)

1.16 J.J. HSIEH, J.A. ROSSI, J.R. DONNELLY,
Appl. Phys. Lett., 28, 709 (1976)

1.17 J.J. HSIEH, C.C. SHEN,
Appl. Phys. Lett., 30, 429 (1977)

1.18 T. YAMAMOTO, K. SAKAI, S. AKIBA, Y. SUEMATSU,
I.E.E.E. J. Quantum Electron., QE - 14, 95 (1978)

1.19 G.H. OLSEN, C.J. NUESE, M. ETTENBERG,
Appl. Phys. Lett., 34, 262 (1979)

1.20 C.T. FOXON, B.A. JOYCE, M.T. NORRIS,
J. Cryst. Growth., 49, 132 (1980)

1.21 B.I. MILLER, J.H. McFEE,
J. Electrochem. Soc., 125, 1311 (1978)

1.22 H. ASAHI, H. OKAMOTO, M. IKEDA, Y. KAWAMURA,
Jap. J. Appl. Phys., 18, 565 (1979)

1.23 M.T. NORRIS,
Appl. Phys. Lett., 36, 833 (1980)

1.24 G.J. DAVIES, R. HECKINGBOTTOM, H. OHNO, C.E.C. WOOD,
A.R. CALAWA,
Appl. Phys. Lett., 37, 290 (1980)

1.25 K.Y. CHENG, A.Y. CHO, W.R. WAGNER, W.A. BONNER,
J. Appl. Phys., 52, 1015 (1980)

1.26 B.I. MILLER, J.H. McFEE, R.J. MARTIN, P,K. TIEN,
Appl. Phys. Lett., 33, 44 (1978)

1.27 R. CORLETT, I. GRIFFITH, J.J. PURCELL,
GaAs and Related Compounds,
Inst. Phys. Conf. Ser. No 24 (1975)

1.28 R.C. CLARKE, L.L. TAYLOR,
J. Cryst. Growth, 31, 190 (1975)

1.29 R.F.C. FARROW,
J. Phys. D., 7, L121 (1974)

1.30 J.H. McFEE, B.I. MILLER, K.J. BACHMANN,
J. Electrochem. Soc., 124, 259 (1977)

1.31 M.T. NORRIS, C.R. STANLEY,
Appl. Phys. Lett., 35, 617 (1979)

1.32 Y. KAWAMURA, M. IKEDA, H. ASAHI, H. OKAMOTO,
Appl. Phys. Lett., 35, 481 (1979)

1.33 J.S. ROBERTS, P. DAWSON, G.B. SCOTT,
To be published in Appl. Phys. Lett.

1.34 Y. MATSUSHIMA, Y. HIROFUJI, S. GONDA, S. MUKAI,
M. KIMATA,
Jap. J. Appl. Phys., 15, 2321 (1976)

1.35 B.I. MILLER, J.H. McFEE, K.J. BACHMANN,
Paper 201, 149th Electrochem. Soc. Meeting,
Washington D.C. (1976)

1.36 B.I. MILLER, J.H. McFEE,
Paper F8, 18th Annual Electronic Materials Conf.,
June 23 - 25, Salt Lake City, Utah (1976)

REFERENCES CHAPTER 2

2.1 A.Y. CHO,
J. Appl. Phys., 41, 782 (1970)

2.2 B.I. MILLER, J.H. McFEE,
J. Electrochem. Soc., 125, 1310 (1978)

2.3 R.F.C. Farrow,
J. Phys. D, 7, 2436 (1974)

2.4 C.T. FOXON, J.A. HARVEY, B.A. JOYCE,
J. Phys. Chem. Solids, 34, 1693 (1973)

2.5 A.Y. CHO, M.B. PANISH,
J. Appl. Phys., 43, 5118 (1972)

2.6 R.F.C. FARROW,
J. Phys. D, 8, L87 (1975)

2.7 G.J. DAVIES, R. HECKINGBOTTOM, H. OHNO,
C.E.C. WOOD, A.R. CALAWA,
Appl. Phys. Lett., 37, 290 (1980)

2.8 K.Y. CHENG, A.Y. CHO, W.R. WAGNER, W.A. BONNER,
J. Appl. Phys., 52, 1015 (1981)

2.9 C.T. FOXON, B.A. JOYCE, R.F.C. FARROW, R.M. GRIFFITHS,
J. Phys. D, 7, 2422 (1974)

2.10 N.F. RAMSEY,
"Molecular Beams",
Oxford, 1956

2.11 A. DRAYTON,
"Vacuum Manual",
Ed. L Holland, 1974

2.12 J.H. NEAVE, P. BLOOD, B.A. JOYCE,
Appl. Phys. Lett., 36, 311 (1980)

2.13 C.T. FOXON, B.A. JOYCE,
Surface Science, 50, 434 (1975)

2.14 C.T. FOXON, B.A. JOYCE,
Surface Science, 64, 293 (1977)

2.15 Y. KAWAMURA, M. IKEDA, H. ASAHI, H. OKAMOTO,
Appl. Phys. Lett., 35, 481 (1979)

2.16 J.H. NEAVE, B.A. JOYCE,
J. Crystal Growth, 43, 204 (1978)

2.17 A.Y. CHO,
J. Appl. Phys., 42, 2074 (1971)

2.18 B.A. JOYCE, C.T. FOXON,
Inst. Phys. Conf. Ser. No. 32, 17 (1977)

2.19 A.Y. CHO,
J. Appl. Phys., 46, 1733 (1975)

2.20 A.Y. CHO, I. HAYASHI,
Met. Trans., 2, 777 (1971)

2.21 A.Y. CHO, I. HAYASHI,
J. Appl. Phys., 42, 4422 (1971)

2.22 M. ILEGEMS, R. DINGLE,
GaAs and Related Compounds,
Inst. Phys. Conf. Ser. 24 p.1, 1975

2.23 J.R. ARTHUR,
Surface Science, 43, 449 (1974)

2.24 C.E.C. WOOD,
Appl. Phys. Lett., 33, 770 (1978)

REFERENCES CHAPTER 3

3.1 M.T. NORRIS,
Ph. D Thesis, University of Glasgow, 1979.

3.2 P.W. SULLIVAN,
Ph. D Thesis, University of Glasgow, 1980.

3.3 B.D. JOYCE, E.W. WILLIAMS,
"Symposium on GaAs and Related Compounds, (Inst. of Phys., Aachen, Germany, 1970) p. 61.

3.4 E.W. WILLIAMS, W. ELDER, M. G. ASTLES, M. WEBB, J.B. MULLIN, B. STRAUGHAN, P.J. TUFTON,
J. Electrochem. Soc., 120, 1741 (1973)

3.5 R.F.C. FARROW,
J. Phys. D., 7, 2436, (1974)

3.6 R.F.C. FARROW,
Chpt. 1.7, 1976 Crystal Growth and Materials,
Ed. E. Kaldis and J.J. Scheel.
N. Holland Publishing Co. (1977)

3.7 M. DOWSETT, R.M. KING, E.H.C. PARKER,
Appl. Phys. Lett., 31, 529 (1977)

3.8 R.F.C. FARROW,
Private Communication.

3.9 S. TOLANSKY,
J. de. Phys., 11, 373 (1950)

3.10 D.G. COATES,
Proc. 2nd Annual S.E.M. Symposium
(IIT Research Inst., Illinois, 1969)

3.11 R.T. HOLM, J.W. GIBSON, E.O. PALIK,
J. Appl. Phys., 48, 212 (1977)

3.12 D.L. RODE,
Phys. Rev. B., 3, 3287 (1971)

3.13 C. PICKERING,
Private Communication.

3.14 The 7K P.L. analysis was undertaken by
G.B. SCOTT of Philips Research Laboratories,
Redhill.

3.15 K.J. BACKMANN, E. BUEHLER, B.I. MILLER,
J. H. MCFEE, F.A. THIEL,
J. Crystal Growth, 39, 137 (1977)

3.16 C.R. STANLEY,
Private Communication.

3.17 H. ASAHI, Y. KAWAMURA, M. IKEDA, H. OKAMOTO,
J. Appl. Phys., 52, 2852 (1981)

3.18 D.W. COVINGTON, E.L. MEEKS,
J. Vac. Sci. Technol., 16, 847 (1979)

3.19 D.G. COATES,
Private Communication.

REFERENCES CHAPTER 4

4.1 J.R. ARTHUR,
Surf. Sci., 38, 394 (1973)

4.2 M. ILEGEMS,
J. Appl. Phys., 48, 1278 (1977)

4.3 M. NAGANUMA, K. TAKAHASHI,
Appl. Phys. Lett., 27, 342 (1975)

4.4 N. MATSUNAGA, T. SUZOKI, K. TAKAHASHI,
J. Appl. Phys., 49, 5710 (1978)

4.5 J.C. BEAN, R. DINGLE,
Appl. Phys. Lett., 35, 925 (1979)

4.6 B.I. MILLER, J.H. McFEE, R.J. MARTIN, P.K. TIEN,
Appl. Phys. Lett., 33, 44 (1978)

4.7 W.J. PRICE,
"Spectrochemical Analysis by Atomic Absorption",
Heyden, 1979

4.8 M.G. Astles, F.G.H. SMITH, E.W. WILLIAMS,
J. Electrochem. Soc., 120, 1750 (1973)

4.9 H.C. CASEY,
"Atomic Diffusion in Semiconductors", Chapt. 6,
Plenum, New York, 1973

4.10 R.M. KUNDUKHOV, S.G. METREVELI, N.V. SINKAEV,
Sov. Phys. - Semicond., 1, 765 (1967)

4.11 A. HOOPER, B. TUCK,
Solid - St. Electron., 19, 513 (1976)

4.12 B. TUCK, A. HOOPER,
J. Phys. D., 8, 1806 (1975)

4.13 S. MAHAJIN, W.A. BONNER, A.K. CHIN, D.C. MILLER,
Appl. Phys. Lett., 35, 165 (1979)

4.14 B.A. JOYCE, C.T. FOXON,
Jap. J. Appl. Phys., 16, 17 (1977)

4.15 A.Y. CHO, M.B. PANISH,
J. Appl. Phys., 43, 5118 (1972)

4.16 J. HORNSTRA, W.J. BARTELS,
J. Cryst. Growth, 44, 513 (1978)

REFERENCES CHAPTER 6

6.1 R. WILLIAMS,
J. Appl. Phys., 37, 3411 (1966)

6.2 D.V. LANG,
J. Appl. Phys., 45, 3023 (1974)

6.3 G.M. MARTIN, A. MITONNEAU, A. MIRCEA,
Elec. Lett., 13, 191 (1977)

6.4 R.A. STALL, C.E.C. WOOD, P.D. KIRCHNER, L.F. EASTMAN,
Elec. Lett., 16, 171 (1980)

6.5 A.M. WHITE, A.J. GRANT, B. DAY,
Elec. Lett., 14, 409 (1978)

6.6 O. WADA, A. MAJERFELD, A.N.N.M. CHOUDHURY,
J. Appl. Phys., 15, 423 (1980)

6.7 G. BREMOND, A. NOVAILHAT, G. GUILLOT,
Elec. Lett., 17, 55 (1981)

6.8 J. GULDBERG,
J. Phys. E: Scientific Inst., 10, 1016 (1974)

6.9 A. MAJERFELD, P.K. BATTACHARYA,
Appl. Phys. Lett., 33, 259 (1978)

6.10 D.E. ASPNES,
Proc. 6th Int. Symposium on GaAs and Related Compounds. St Louis Conf. (Inst. of Phys., London 1977) p. 110

6.11 D.V. LANG, R.A. LOGAN,
J Electron. Mater., 4, 1053 (1975)

6.12 F. HASAGAWA, A. MAJERFELD,
Elec. Lett., 12, 52 (1976)

6.13 A. MIRCEA, A. MITONNEAU,
J. de Phys. (Lett.), 40, L-31 (1979)

6.14 W. FAWCETT, D.C. HERBERT,
J. Phys. C, 7, 1641 (1974)

6.15 M. OZEKI, J. KOMENO,
A. SHIBATOMI, S. OHKAWA,
Inst. Phys. Conf. Ser No 45, 220 (1978)

REFERENCES CHAPTER 7

7.1 P.W. SULLIVAN, R.M. PARK,

To be published in J. Cryst. Growth

7.2 T. AMBRIDGE, M.M. FAKTOR,

Inst. Phys. Conf. Ser. No. 24, 320 (1975)

REFERENCES APPENDIX A

A.1 C.A. WALLACE, R.C.C. WARD,
J. Appl. Cryst., 8, 255 (1975).

A.2 S.M. SZE,
"Physics of Semiconductor Devices"
John Wiley and Sons, New York, 1969.

A.3 J. HILDEBRAND, R.D. GOLD,
RCA Rev., June 1960.

A.4 C.O. THOMAS, D. KAHNG, R.C. MANZ,
J. Electrochem. Soc., 109, 1055 (1962).

A.5 D.R. DECKER,
J. Electrochem. Soc., 115, 1085 (1968).

A.6 A.Y. CHO, F.K. REINHART,
J. Appl. Phys., 45, 1812 (1974).

A.7 E.H. RHODERICK,
"Metal Semiconductor Contacts,"
Oxford, 1978.